THE ASTROPHYSICAL JOURNAL SUPPLEMENT SERIES, 99:27–66, 1995 July

EMISSION-LINE IMAGING OF 3CR RADIO GALAXIES. I. IMAGING DATA

PATRICK J. MCCARTHY,[1,2,3,4] HYRON SPINRAD,[1] AND WIL VAN BREUGEL[3,5]
Received 1994 June 24; accepted 1994 December 14

ABSTRACT

We present emission-line and continuum images of a sample of 53 3CR radio galaxies with $0.05 < z < 2.0$. Each object was imaged in one of the following emission lines: Hα, [O III] λ5007, [O II] λ3727, or Lyα. The visible continuum, emission-line, and radio morphologies of each object are described. The galaxies show a wide range of structures on scales ranging from subkiloparsec circumnuclear emission-line regions to 300 kpc nebulae. For $z > 0.3$ nearly all of the emission-line regions are aligned with their radio source axes. At redshifts greater than $\sim$0.6 the optical/UV continua show a strong alignment with the radio axes. All of the emission-line regions show a strong correlation with the arm-length asymmetry of their radio source. The data presented here are analyzed in Paper II.

Subject headings: galaxies: structure—ultraviolet: galaxies

1. INTRODUCTION

The spatially resolved emission-line regions of radio sources have been a subject of intensive observational study since their initial discovery in the late 1960s. The application of CCDs and narrow interference filters allowed for detailed observations of emission-line nebulae at significant redshifts (see Balick & Heckman 1982 for a review). In the past decade a number of radio galaxies at moderate redshifts have been studied in detail. While a general picture of the dominant physical properties involved in producing these 100 kpc sized nebulae has been assembled, a number of important questions concerning the origin and the energetics of the giant emission-line regions remain. The observations required for these studies are observing-time–intensive, so most efforts have been directed at a few spectacular objects.

The most spectacular emission-line nebulae associated with radio galaxies have sizes greater than 100 kpc. Even the more typical objects are impressively large, with sizes $\gtrsim$10 kpc at fairly bright surface brightness levels. The large nebulae bear a morphological relationship to their radio sources: the line emission is distributed in filaments and clumps that often lie along the boundaries of, or adjacent to, bright features in the radio maps (van Breugel 1986, 1990; Baum & Heckman 1989a). At large redshifts nebulae associated with the 3CR and 1 Jy class sources show close alignment with their radio axes (McCarthy et al. 1987b, 1990), as well as a strong correlation with the structural asymmetries of the sources (Pedelty et al. 1989a, b; McCarthy, van Breugel, & Kapahi 1991).

The extranuclear emission lines have ionization and excitation states that are qualitatively similar to those of the narrow-line regions in active galactic nuclei (AGNs) (Robinson et al. 1987). The schematic view of the emission-line nebulae that has arisen from detailed study of a modest sample of objects is built around clouds illuminated by a partially obscured central UV source (e.g., Fosbury 1986, 1990). This picture is very similar to the model for NGC 1068 and other Seyfert I galaxies proposed by Antonucci & Miller (1985). While there are some problems associated with the central photoionization model, it appears to account for the gross characteristics of the nebulae. The morphological and energetic properties of radio galaxy nebulae at high and low redshifts are reviewed by Fosbury (1990) and McCarthy (1993).

The systematic survey of the emission-line regions of radio galaxies at $z \lesssim 0.2$ by Baum (1987) and coworkers (Baum et al. 1988; Baum, Heckman, & van Breugel 1992; Baum & Heckman 1989a, b) produced one of the only fair samples of such objects. Early spectroscopic studies of the high-redshift radio galaxies from the 3CR catalog by Spinrad & Djorgovski (1984a, b) showed that extended line emission is very prevalent in these distant galaxies. Our goal was to collect a large uniform data set of emission-line images of radio galaxies at high z. When combined with the lower redshift data from the Baum et al. survey, this yields a largely unbiased data set spanning more than 70% of the Hubble time and more than four orders of magnitude in radio luminosity.

In the following sections we will discuss the sample selection (§ 2), the instruments and techniques used (§ 3), the images (§ 4), and the basic parameters for quantifying the properties of the emission-line regions (§ 5). The analysis of these data will be presented in Paper II.

2. THE SAMPLE

Our sample of 52 objects was drawn from the completely identified 3CR sample of extragalactic radio sources, defined by $S_{178} > 9$ Jy and $\delta > -05$ (Bennet 1962). A more complete subsample (from the point of view of radio flux densities), the 3CRR, has been defined by Laing, Riley, & Longair (1983). Our program objects were selected solely on the basis of being identified as galaxies in Spinrad's compilation of identifications and redshifts for the 3CR catalog (Spinrad et al. 1985a;

[1] University of California, Berkeley.
[2] The Observatories of the Carnegie Institution of Washington.
[3] Guest Observer at Kitt Peak National Observatory, which is operated by the National Optical Astronomy Observatories for AURA, Inc.
[4] Hubble Fellow.
[5] Institute of Geophysics and Planetary Physics, Lawrence Livermore National Laboratory.

Djorgovski et al. 1988; Strom et al. 1989; Spinrad et al. 1995). Instrumental constraints (e.g., the lack of appropriate filters) prevented a few objects from being observed. The sources were selected so as to give a well-balanced coverage of redshifts. We intentionally biased our selection of objects toward intermediate- and high-redshift ($z > 0.2$) objects, so that when they were combined with the sample of Baum et al. (1988), we would have an even representation of high and low redshifts. The total number of 3CR galaxies imaged in one or more emission lines in this sample, the sample of Baum et al., and individual objects from the literature is 108, or 50% of the total of 217 3CR galaxies. Emission-line images of radio galaxies from the 4C and 1 Jy surveys will also be included in our analysis. This gives us a unique data set: never before has a sample of radio galaxies been so thoroughly observed in the optical with a range of redshifts from 0.1 to greater than 2. The sample used in this investigation is not complete, but between this work and the surveys of Baum et al. (1988) and Rigler et al. (1992), we believe that essentially all of the 3CR galaxies with significantly extended line emission have been imaged in at least one emission line. The long-slit spectroscopy of 3CR galaxies carried out during the identification and redshift determination program supports this conclusion. The impact of the incompleteness and biases, where significant, will be discussed in Paper II.

3. OBSERVATIONS AND REDUCTIONS

3.1. *Telescopes, Cameras, and Filters*

The bulk of the observations reported here were obtained with the Lick 3 m telescope. The light pollution at Mount Hamilton is severe, but our emission-line imaging program, with its narrow filter bandpasses, was relatively insensitive to the bulk of the strong manmade emission lines in the sky spectrum.

At the time of this investigation the Lick 3 m telescope had two imaging/spectrograph cameras at the Cassegrain focus. Both cameras used the same UV-sensitized TI 800 × 800 CCD. The first, a transmission grating-prism spectrograph, had a high throughput throughout most of the spectrum, but did not transmit below 3700 Å or beyond 8700 Å. Imaging observations were made by opening the slit jaws and removing the grism from the beam. The pixel scale was 0.″731, and the full usable field of view (limited by vignetting) was 2.″2 × 2.″2. The filters were located above the collimator in a slow beam making bandpass shifts insignificant. The optics had large chromatic aberration; thus each filter required a separate focus setting, and special care was needed to match the foci of the on- and off-band filters.

The other Cassegrain camera was a reflection-grating system optimized for short wavelengths ($\lambda < 4000$ Å). Since this camera also transmitted at long wavelengths (8500–10000 Å), it was used to observe a few objects with redshifts such that [O/II] λ3727 was beyond the reach of the lens-grism camera. Imaging observations with this spectrograph were made by opening the slit jaws and replacing the grating with a flat mirror. This camera had a smaller field of view (1.″5 × 1.″5) and poorer image quality than the lens-grism camera. The pixel size was 0.″67. Details of the spectrographs and their operation are given by Miller & Stone (1987).

A significant fraction of the data presented here was obtained with the Kitt Peak 2.1 m telescope and its Cassegrain focus direct camera. The detector was a Tektronix 500 × 500 CCD. The pixel size for this camera/CCD combination is 0.″34, giving better sampling than the Lick cameras. A few objects were observed with the Kitt Peak 4 m telescope and its prime-focus direct camera. The detector was a Texas Instruments 800 × 800 CCD with a pixel scale of 0.″297. The filters are located in a converging beam, resulting in bandpass shifts of ~5 Å.

The emission-line images were obtained with a set of narrowband interference filters. These filters are single-stack etalons with $\Delta\lambda/\lambda_c = 0.011$ and central transmissions greater than 70% (red) and greater than 50% (blue). They are blocked to more than 0.1% from soft X-rays to 1.2 μm. The transmission curves of all filters were determined by taking spectra of the incandescent lamp used for spectroscopic flat fields with the filter in the beam.

3.2. *Observational Techniques*

Each object in the sample was imaged with one interference filter and a broadband continuum filter. The choice of the narrowband filter was dictated by the redshift and the desired emission line. For $z < 0.2$ most of the objects were observed in Hα + [N II] λ6548, 6584; for $0.2 < z < 0.6$ many were imaged in [O III] λ5007, although some were imaged in [O II] λ3727. For $0.6 < z < 1.5$ all of the objects were imaged in [O II] λ3727, while for $z > 1.7$ the imaging was done in Lyα. The broadband filter was usually the Spinrad night-sky rejection filter (λ_0 = 6900 Å; $\Delta\lambda$ = 1500 Å), r_S (Djorgovski 1985). The Kitt Peak observations used either R or V as the off-band filter. Ideally, one should use a narrow-line–free filter for the continuum imaging. This proved impractical because of the faint continuum magnitudes of the objects. For some objects the broadband images were contaminated by the emission lines. The only object for which this had significant impact was 3C 458, for which the V and R images are contaminated by [O II] λ3727 and [O III] λ5007, respectively. The r_S filter was used at Lick because it blocks many of the strong manmade emission lines in the Mount Hamilton sky.

For each object, two integrations of typically 1800 s duration each were made with the interference filter. In a few brighter objects the integrations were shorter. In the cases of 3C 356, 3C 326.1, 3C 454.1, 3C 437, 3C 458, and 3C 381, longer integrations were made with the line filter. Three broadband integrations, typically 300 s in duration, were interleaved with the interference filter images. The interleaving of the observations was useful in keeping the point-spread function the same for the on- and off-band images. Observations of the twilight sky were made with each of the interference filters to be used in constructing flat-field images.

3.3. *Reductions*

The data processing consists of three steps: (1) flattening the individual images, (2) stacking the images taken through each filter, and (3) removing the continuum from the emission-line images.

For the broadband r_S images taken at Lick, conventional dome flats leave low spatial frequency noise in the data. Dark

sky median flats were constructed from observations made throughout each night. Images of the twilight sky taken through the narrowband filters were combined using the same median technique. This removed any bright stars and cosmic-ray events that appeared in the individual flats.

After flattening, the positions of five relatively bright stars or galaxies were measured for each individual exposure, for all filters, of a given field. All of the images were then shifted into mutual registration using a bilinear interpolation algorithm. The individual frames for each object and filter were then coadded. The sky levels in the stacked continuum and line-plus-continuum images were determined by computing the mode of the distribution of pixel values. The sky was then subtracted from both the on- and off-band images.

At this point in the processing the on- and off-band stacked images had been flattened, sky-subtracted, and shifted into mutual registration. The remaining step was the differencing of the on- and off-band images. To accomplish this, the off-band image was scaled to the level of the on-band image, preserving the flux in the emission-line image. The scaling was chosen such that stars and galaxies (other than the object of interest) were subtracted completely. Often there was a large enough wavelength difference between the interference filter image and the broadband image that color differences were important. In these cases the scaling was chosen so that the galaxies (whose colors should match those of the program objects better than the stars do) were subtracted completely. In practice, the optimal scaling was found by several iterations using the image display to judge the quality of the subtraction.

The flux calibration of the images was accomplished using two different techniques. The first uses observations of spectrophotometric standard stars from Oke (1974) and Stone (1977) with the appropriate interference filter. Spectrophotometric standards rather than conventional *BVR* standards were used because they have published monochromatic flux densities determined with bandpasses similar to those used here. The ratio of signals in the continuum-subtracted line images and the standard star images was computed and normalized to a common exposure time. The flux in the line image was computed by assuming a square bandpass with a width equal to the FWHM.

Many of the objects were observed under nonphotometric conditions and hence cannot be flux-calibrated in an absolute sense. Fortunately, the vast majority of objects in the sample have been observed spectroscopically under photometric conditions. These spectrophotometric observations were used to determine the total (spatially integrated) emission-line fluxes. This was done by computing the fraction of the total emission-line light in the aperture used for the spectroscopy and scaling the spectroscopic flux accordingly. Comparison between line fluxes determined with both methods shows that in most cases the agreement was ~20%, about as good as can be expected for this type of measurement.

We have not attempted to calibrate the broadband images in this survey. The photometric studies of 3CR radio galaxies by Smith & Heckman (1989a, b) at low redshift and by Dickinson, Djorgovski, & Spinrad (1995) at larger redshifts contain broadband data of higher quality than those presented here.

After each emission-line image was flux-calibrated, contour maps were made. The lowest contour in these plots was typically at a surface brightness level of 1.0×10^{-17} ergs s^{-1} cm^{-2} arcsec^{-2}.

4. RESULTS

A total of 53 galaxies with redshifts ranging from 0.05 to 2 were imaged. Table 1 gives a complete list of all of the imaging observations and the instrumental details. Below we summarize the optical and radio morphologies of each object observed. In Figures 1–53 we present contour plots of the continuum (*left-hand panel*) and emission-line (*right-hand panel*) images of each object. The scale for each image is in arcseconds. For all of the illustrations (except 3C 321) north is at the top and east is to the left. The outer contours have been smoothed with a Gaussian with $\sigma = 1.25$ pixels; the inner contours have not been smoothed. The contour levels in the emission-line images are in surface brightness units, as listed in each caption. In each illustration we attempted to place the object in the center of the frame, but the placement is rarely exact. The registration between the line and continuum objects is exact in most cases. Halftone images of the most complex and extended objects are presented in Figures 54–59 (Plates 1–8). These plates bring out the low surface brightness features and complex structures in the emission-line images better than the contour plots.

4.1. *Notes on Individual Objects*

3C 382 ($z = 0.06$; Fig. 1).—This is one of the classic broad-lined radio galaxies (Osterbrock, Koski, & Phillips 1986). The continuum has the shape of a normal gE galaxy with some distortions in the outermost isophotes. A continuum image is also given in Hutchings, Johnson, & Pike (1988). The Hα image shows diffuse emission surrounding the nucleus and a high surface brightness patch of emission lying to the west. The inner region of the Hα image is saturated, and thus we cannot determine the structure of the innermost regions. Long-slit spectra, however, confirm that there is diffuse emission surrounding the nucleus. Ultraviolet spectra of the nucleus and ground-based blue spectra of the extended emission are given by Tadhunter, Perez, & Fosbury (1986). The radio source is a large (184″) double in position angle 50° (Tadhunter et al. 1986).

3C 321 ($z = 0.09$; Fig. 2).—This object has a large complex of extended line emission. Spinrad et al. (1985a) list 3C 321 as having a double nucleus. In our Hα and continuum images the secondary peak is not well resolved. An image with a larger field is given in Baum et al. (1988). The continuum image presented here was taken with a narrow-line–free filter. This image shows that the Hα emission in both the nucleus and the knot to the east is spatially offset from the continuum. The most unusual aspect of this object is that the narrow-line spectra of the nucleus and the knot have identical line strengths and surface brightnesses (van Breugel, McCarthy, & Spinrad 1995). Van Breugel et al. consider a number of possible explanations for the identical line spectra, but conclude that photoionization by the nucleus (as defined by the radio core) is the most likely mechanism. A low-resolution radio map is given in Leahy & Williams (1984).

3C 433 ($z = 0.10$; Fig. 3).—This object lies in a cluster and has a close companion to the northwest. The Hα image shows emission extended over 8″ with a filamentary structure. Con-

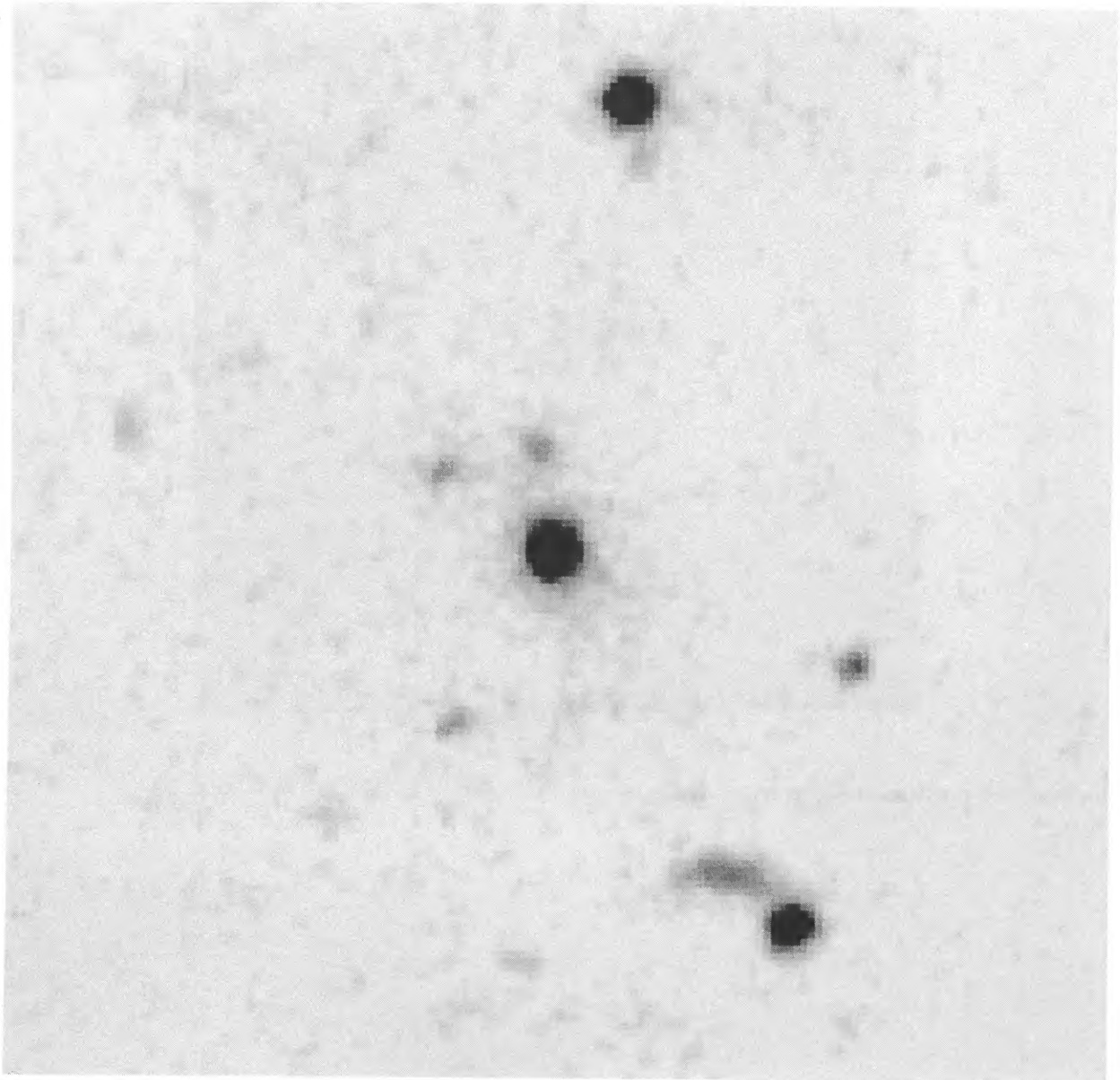

Fig. 54*a*

FIG. 54.—3C 458 ($z = 0.29$) in (*a*) *V*, (*b*) [O II] λ3727 (λ4808), and (*c*) [O III] λλ5007, 4959 (λ6477). Each image is 50″ on a side. The *V* and λ4808 images were taken with the 2.1 m telescope at Kitt Peak; the λ6477 image was taken with the Lick 3 m. The [O II] λ3727 emission can be traced over more than 30″.

PLATE 2

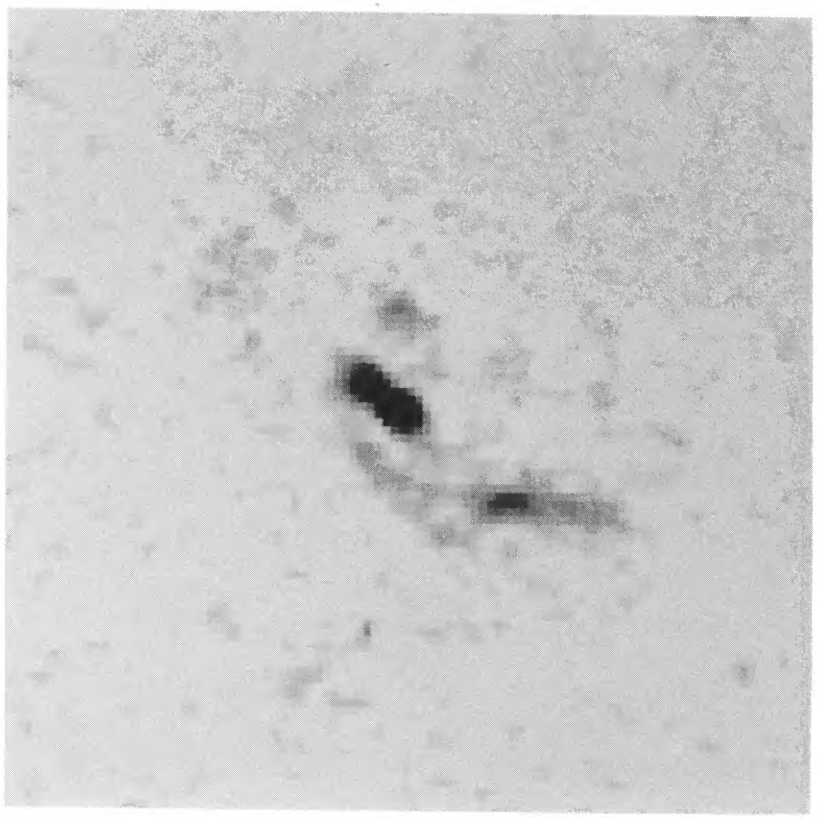

Fig. 54*b*

McCarthy, Spinrad, & van Breugel (see 99, 29)

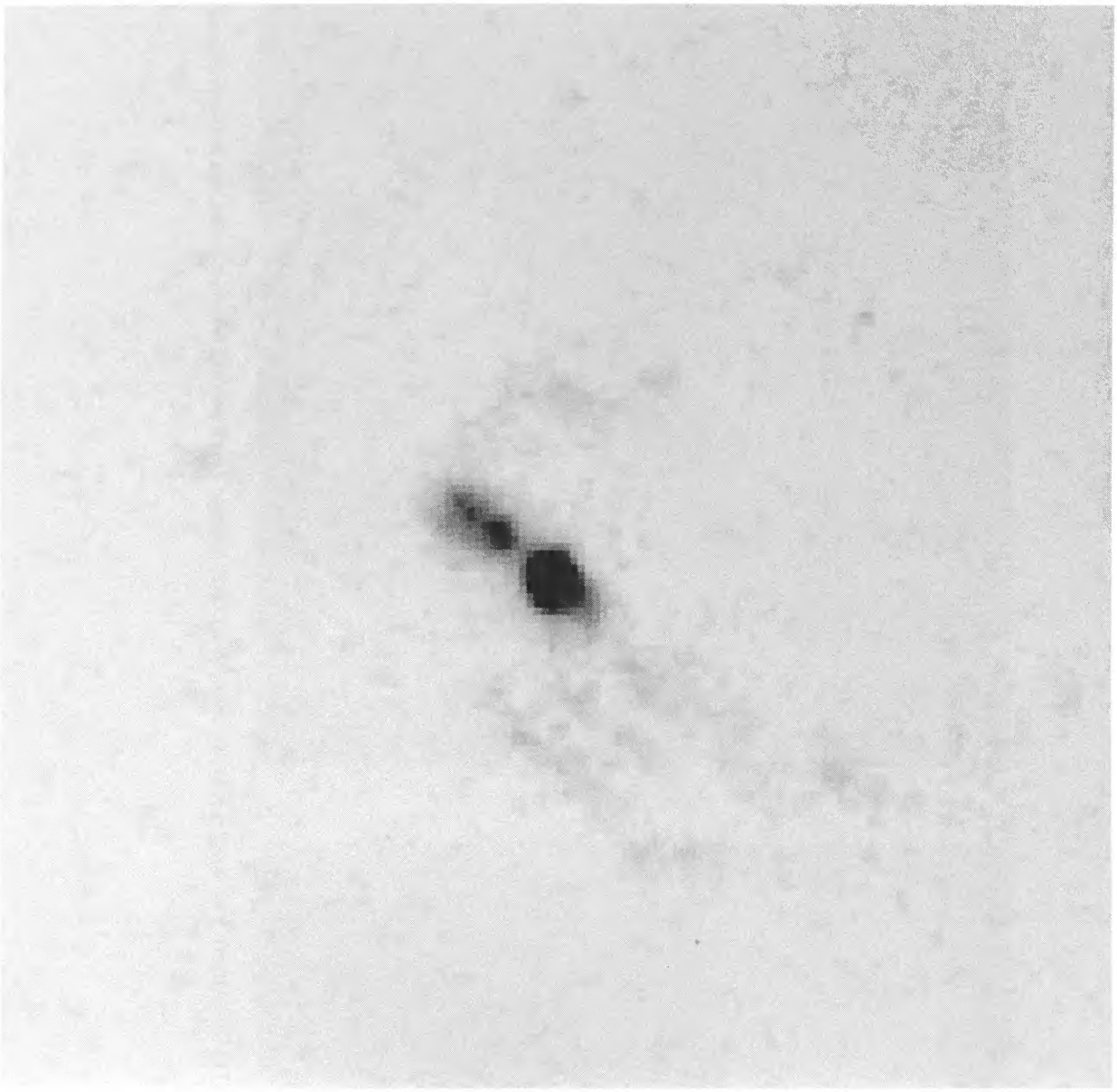

Fig. 54*c*

McCarthy, Spinrad, & van Breugel (see 99, 29)

PLATE 4

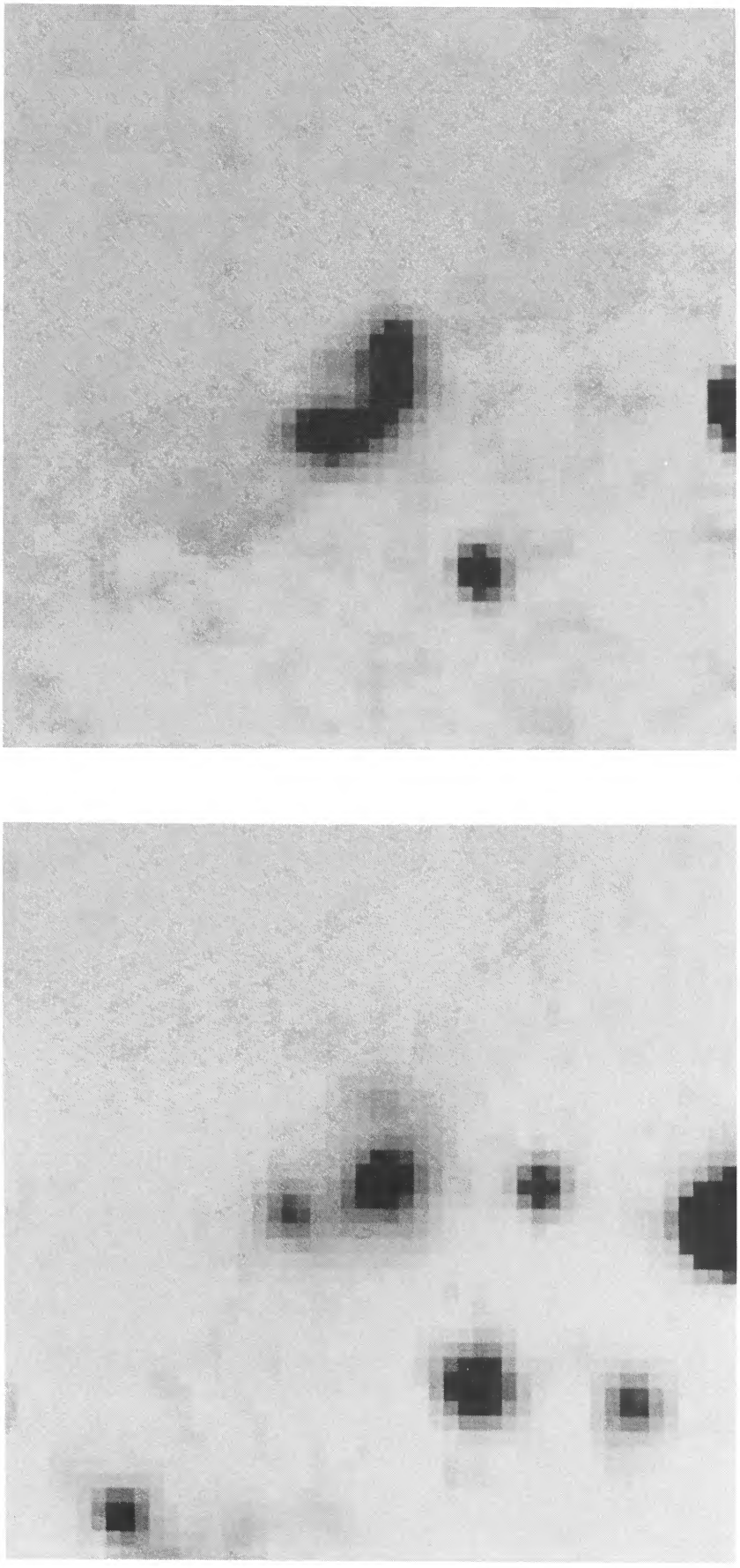

FIG. 55.—3C 435A ($z = 0.47$) in r_S (*left*) and [O III] λ3727 (λ5508) (*right*). Each image is 36″ × 36″. Faint [O II] λ3727 emission can be seen well beyond the main high surface brightness regions of the nebula.

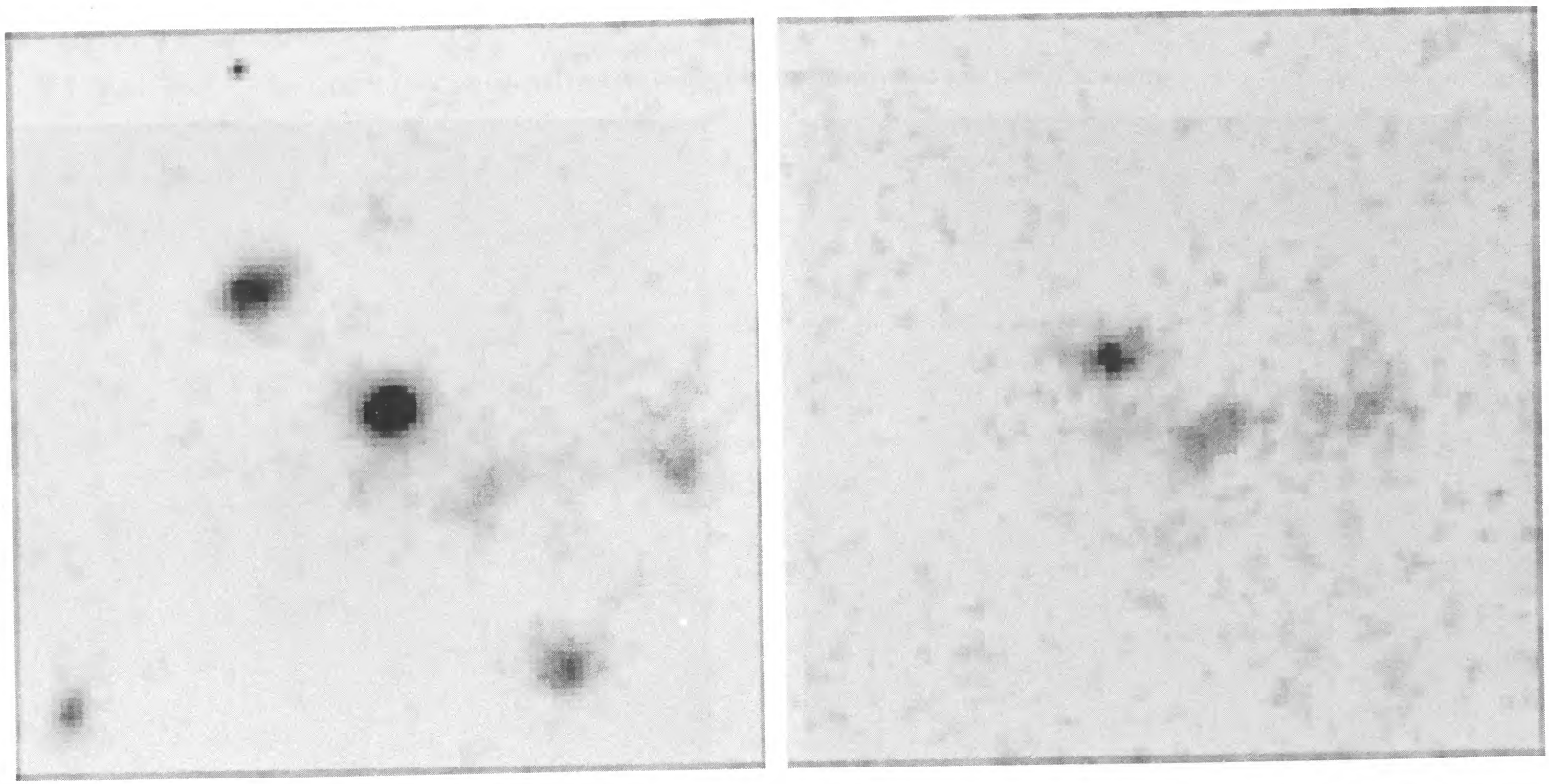

FIG. 56.—3C 277.2 ($z = 0.77$) in R (*left*) and [O II] λ3727 (λ6581) (*right*). Each image is 29″ on a side. The images were taken with the Kitt Peak 4 m telescope. The [O II] λ3727 emission can be traced over 15″.

McCARTHY, SPINRAD, & VAN BREUGEL (see 99, 29)

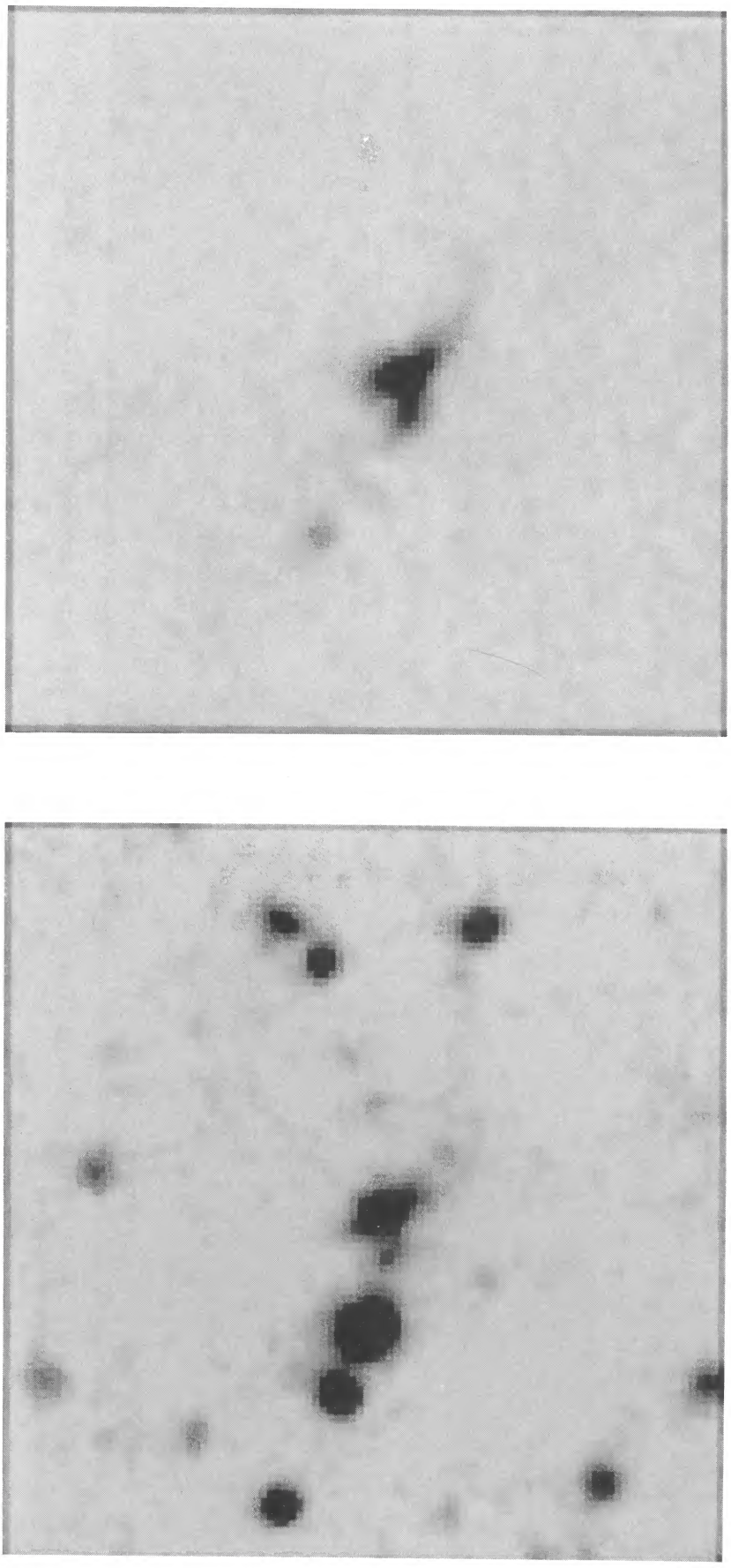

FIG. 57.—3C 265 ($z = 0.81$) in r_S (*left*) and [O II] λ3727 (λ6606) (*right*). Each image is 72″ on a side.

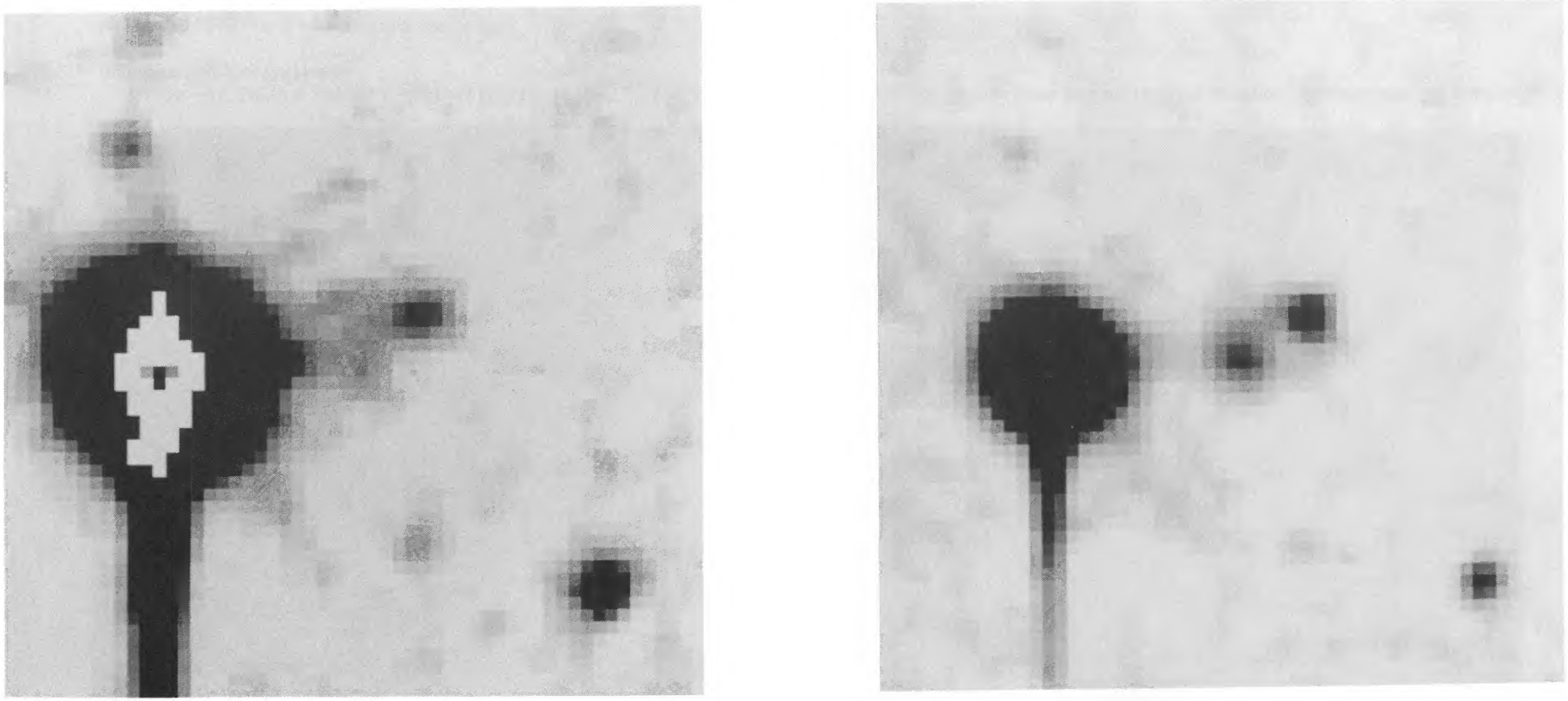

FIG. 58.—3C 356 ($z = 1.08$) in r_S (*left*) and [O II] λ3727 (λ7781) (*right*). Each image is 40″ on a side and was taken with the Lick 3 m telescope. The continuum has not been subtracted from the [O II] image.

McCARTHY, SPINRAD, & VAN BREUGEL (see 99, 29)

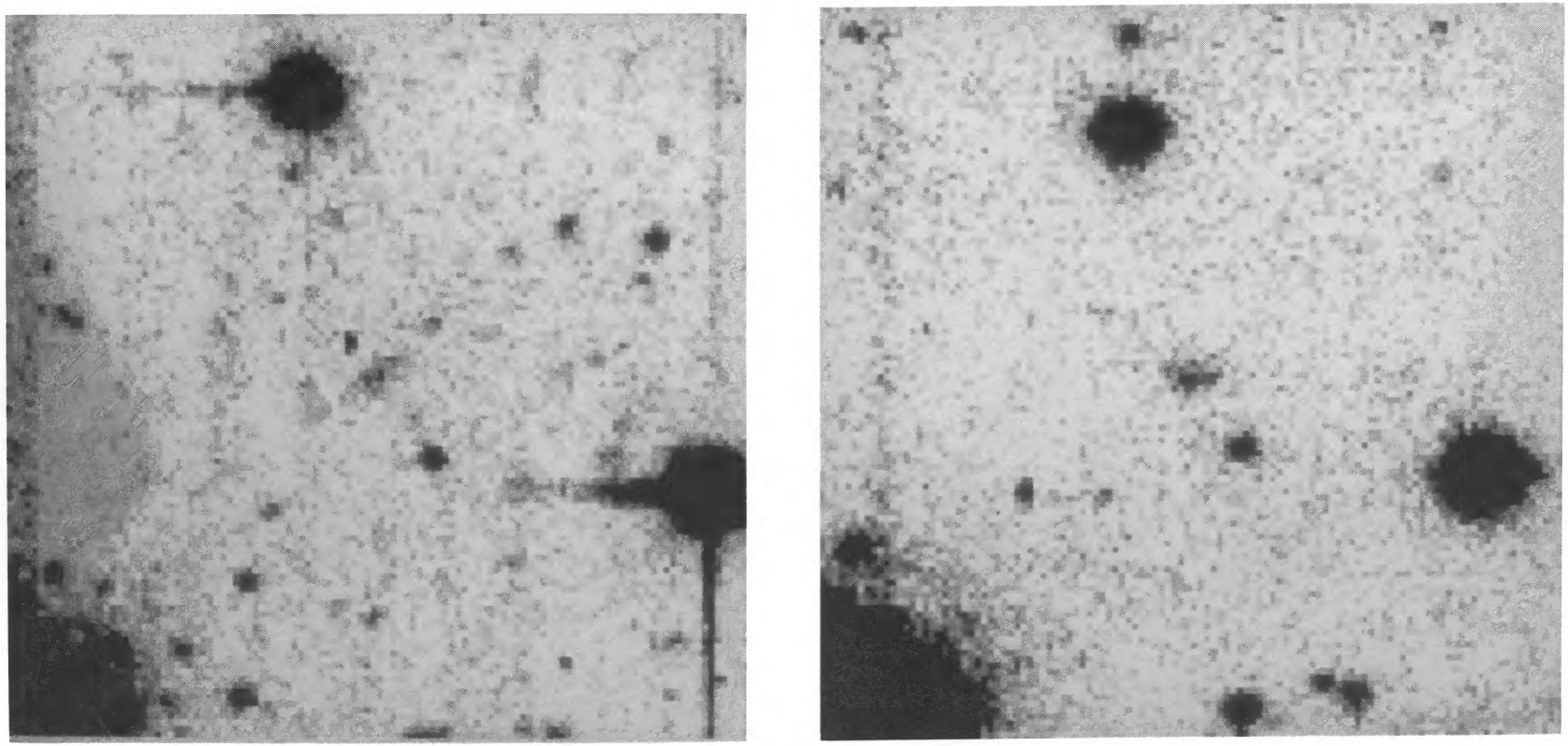

FIG. 58.—3C 356 (z = 1.08) in r_S (*left*) and [O II] λ3727 (λ7781) (*right*). Each image is 40″ on a side and was taken with the Lick 3 m telescope. The continuum has not been subtracted from the [O II] image.

TABLE 1

JOURNAL OF OBSERVATIONS

3CR	z	Date	Telescope & Camera	Line Filter	Exposure Time	Continuum Filter	Exposure Time
454.1	1.8470	27 Jul 87	3m UVS	3440/100	4500	...	...
326.1	1.8250	7 Jul 87	3m UVS	3440/100	10800	...	...
		8 Jul 87	3m UVS	3440/100	5400	...	...
256.0	1.8190	2 Apr 87	3m UVS	3440/100	3600	...	...
437.0	1.4800	3 Jul 87	3m UVS	9230/100	5100	...	...
		27 Jul 87	3m UVS	9230/100	2400	...	...
297.0	1.4061	15 Feb 88	3m UVS	8945/70	1800	r_S	600
238.0	1.4050	15 Feb 88	3m UVS	8945/70	1800	r_S	300
36.0	1.3010	15 Feb 88	3m UVS	8570/80	2200	r_S	300
266.0	1.2750	13 Feb 88	3m UVS	8470/85	4200	r_S	900
324.0	1.2063	7 Jun 86	3m UVS	8225/85	1800	...	...
267.0	1.1400	12 Jan 87	4m PF	7935/85	1800	R	600
305.1	1.1320	27 Jul 87	3m UVS	7935/80	1800	r_S	150
252.0	1.1035	31 Jan 87	3m LG	7850/80	2500	r_S	600
124.0	1.0830	25 Sep 87	3m LG	7781/80	2700	r_S	600
356.0	1.0790	11 Aug 86	3m LG	7781/80	4500	r_S	840
173.0	1.0350	15 Feb 88	3m UVS	7580/70	1800	r_S	400
280.0	0.9975	30 Jan 87	3m LG	7433/75	3600	r_S	600
184.0	0.9940	2 Dec 86	3m LG	7433/75	3300	r_S	750
22.0	0.9370	2 Dec 86	3m LG	7193/75	2400	r_S	600
217.0	0.8975	24 Nov 87	2m Cass	7146/70	3600	R	2100
325.0	0.8600	12 May 88	2m Cass	6916/70	1200	R	1200
6.1	0.8400	4 Oct 86	3m LG	6871/70	1200	r_S	200
54.0	0.8274	16 Feb 88	3m LG	6826/70	3600	r_S	600
263.1	0.8240	25 Apr 87	3m LG	6781/70	3000	r_S	600
226.0	0.8177	31 Jan 87	3m LG	6781/70	2500	r_S	600
265.0	0.8110	30 Jan 87	3m LG	6606/70	3000	r_S	900
352.0	0.8057	16 Feb 88	3m LG	7832/75	4200	r_S	1000
41.0	0.7940	23 Aug 87	3m LG	6693/70	3000	r_S	900
340.0	0.7754	1 Aug 87	3m LG	6606/70	1800	r_S	600
277.2	0.7660	12 Jan 87	4m PF	6581/70	1800	R	600
318.0	0.7520	17 May 88	2m Cass	6520/70	3600	R	1520
343.1	0.7500	25 Apr 87	3m LG	6520/70	1800	r_S	600
247.0	0.7489	26 Apr 87	3m LG	6520/70	2400	r_S	200
292.0	0.7130	21 May 88	2m Cass	6351/70	3000	R	900
441.0	0.7070	25 Sep 87	3m LG	6351/70	1800	r_S	140
		8 Sep 86	3m LG	6351/70	3300	r_S	1050
172.0	0.5191	31 Jan 87	3m LG	5684/60	2400	r_S	300
44.0	0.6600	7 Sep 86	3m LG	6187/70	3600	r_S	300
337.0	0.6350	10 May 86	3m LG	6107/70	3000	r_S	600
169.1	0.6330	3 Dec 86	3m LG	6067/70	2750	r_S	600
49.0	0.6210	8 Oct 86	3m LG	7781/70	2400	r_S	600
		19 May 88	2m Cass	7781/70	4200	R	900
330.0	0.5500	18 Feb 88	3m LG	7781/70	1800	r_S	720
		27 Apr 87	3M LG	7781/70	3000	r_S	500
172.0	0.5191	31 Jan 87	3m LG	5684/60	2400	r_S	300
435A	0.4710	30 Jul 87	3m LG	5508/60	3600	r_S	750
411.0	0.4670	2 Jul 87	3m LG	7336/70	900	r_S	400
313.0	0.4610	21 May 87	2m Cass	7336/75	2400	R	900
411.0	0.4670	2 Jul 87	3m LG	7336/70	900	r_S	400
327.1	0.4628	19 May 88	2m Cass	5434/60	2700	R	1100
341.0	0.4480	31 Jul 87	3m LG	5434/60	1800	r_S	600
306.1	0.4410	18 Feb 88	3M LG	5366/60	3000	r_S	800
244.1	0.4280	12 May 88	3m LG	7146/75	1200	r_S	400
99.0	0.4260	24 Nov 87	2m Cass	7146/70	2400	R	600
274.1	0.4220	19 May 88	2m Cass	5298/60	1800	R	1800
268.3	0.3710	21 May 88	2m Cass	6871/70	3000	V	1200
299.0	0.3670	12 May 88	3m LG	6871/70	3000	r_S	900
458.0	0.2900	24 Dec 87	3m LG	4808/50	3500	r_S	900
		3 Dec 86	3m LG	6477/70	1800	r_S	600
		26 Oct 87	3m LG	8478/80	2400	r_S	600
		25 Nov 87	2m Cass	4808/50	3600	V	1020

TABLE 1—*Continued*

3CR	z	Date	Telescope & Camera	Line Filter	Exposure Time	Continuum Filter	Exposure Time
		12 Jan 87	4m PF	6477/70	1800	R	900
153.0	0.2769	24 Nov 87	2m Cass	4776/50	2100	R	450
300.0	0.2700	19 May 88	2m Cass	6351/65	3000	V	1200
460.0	0.2680	4 Oct 86	3m LG	6391/65	2700	r_S	600
303.1	0.2670	19 May 88	2m Cass	6351/65	2100	R	900
379.1	0.2560	3 Jul 87	3m LG	6269/65	2700	r_S	800
		17 May 88	2m Cass	6269/65	3000	r_S	1200
79.0	0.2559	23 Dec 87	3m LG	6269/70	3000	r_S	600
		26 Nov 87	2m Cass	6520/70	5400	R	300
93.1	0.2440	8 Oct 86	3m LG	8149/70	1800	r_S	300
284.0	0.2394	17 May 88	2m Cass	6187/65	4200	R	1500
456.0	0.2330	1 Aug 87	3M LG	8091/86	1200	r_S	600
436.0	0.2145	8 Oct 86	3m LG	7986/70	3200	r_S	450
28.0	0.1952	25 Nov 87	2m Cass	7832/78	3600	R	300
33.1	0.1810	2 Dec 86	3m LG	7730/78	3000	r_S	600
357.0	0.1664	11 Aug 86	3m LG	7630/78	3300	r_S	700
381.0	0.1605	23 Aug 87	3m LG	5826/60	1800	r_S	300
		1 Aug 87	3m LG	7630/78	4500	r_S	750
		3 Jul 87	3m LG	7630/78	800	...	...
		21 May 88	2m Cass	7630/78	2400	R	500
135.0	0.1083	25 Nov 87	2m Cass	7384/75	3300	R	900
433.0	0.1016	2 Dec 86	3m LG	7193/74	1800	r_S	135
382.0	0.0578	9 May 86	3m LG	6961/70	1700	7193/72	1000

tinuum and Hα images are also given by Baum et al. (1988). The radio source has an edge-darkened appearance as shown by Baum et al. (1988). The residuals associated with the objects to the north and east of 3C 433 are the result of poor continuum subtraction.

3C 135 ($z = 0.13$; Fig. 4).—This giant elliptical galaxy lies in a rich cluster of galaxies. The Hα image shows a small high surface brightness structure oriented along the minor axis of the galaxy, typical of the small circumnuclear disk class of objects discussed by Baum & Heckman (1989a). The Hα image also shows emission from two of the spiral members of the cluster, one of which may be seen in Figure 4. The radio source is a Fanaroff-Riley class II (FR II) double.

3C 381 ($z = 0.16$; Fig. 5).—This object is quite remarkable

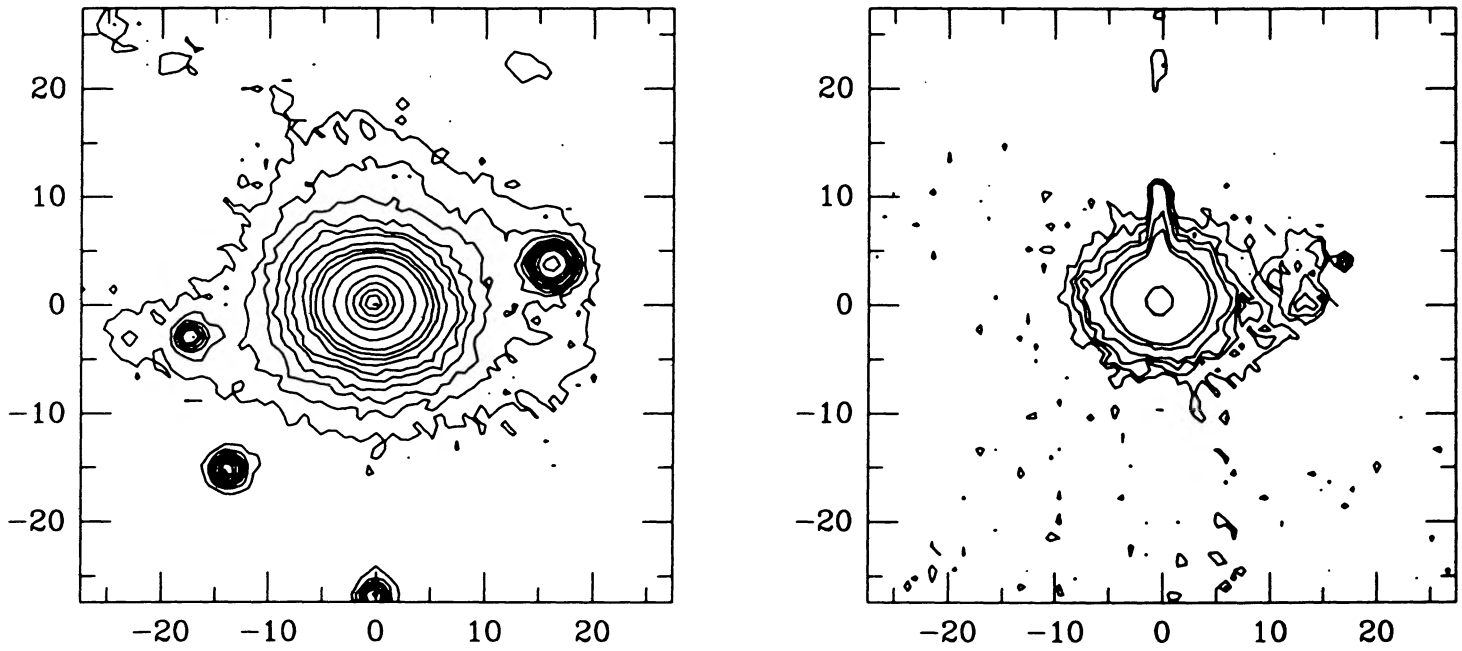

FIG. 1.—3C 382 in Hα and r_S. The strongly saturated region in the center of the Hα image made flux calibration difficult. As a result we are unable to give the surface brightness levels of the contours.

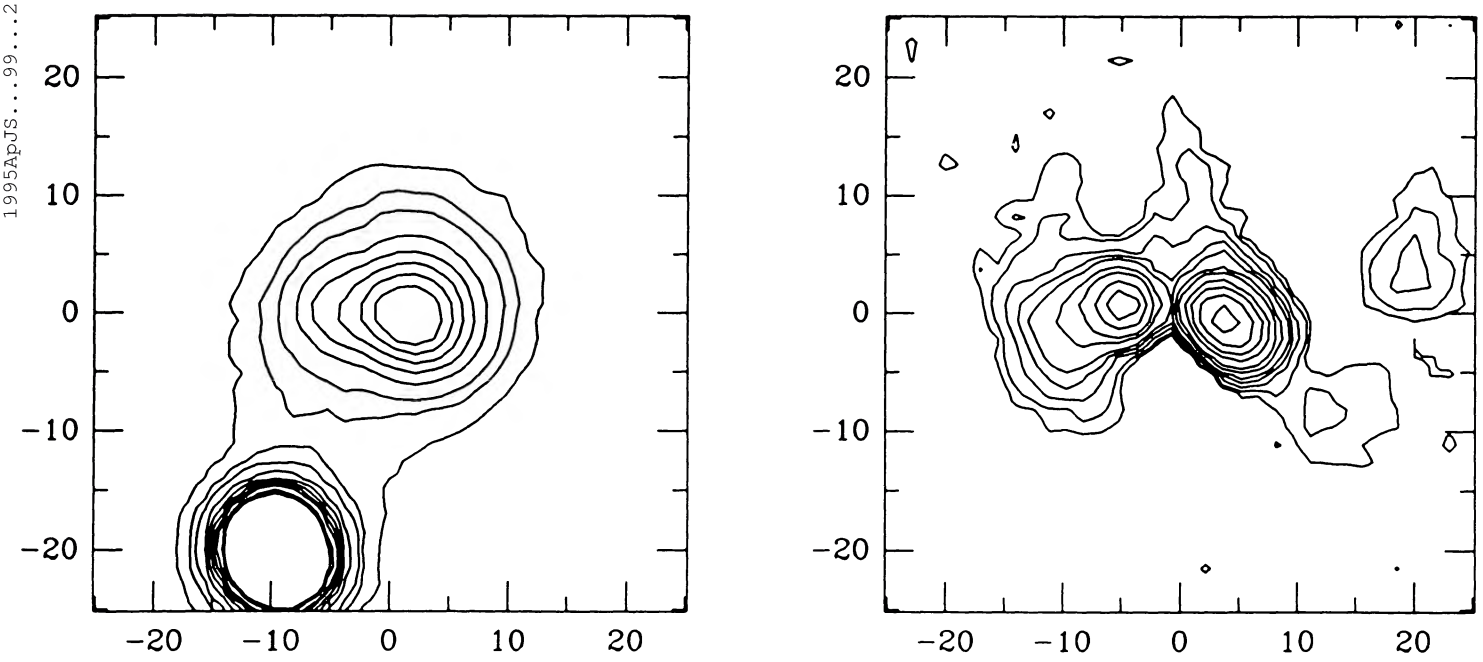

FIG. 2.—3C 321 in Hα and 6737 Å continuum. The image has been rotated by 40°. A calibrated image covering a larger field is given in Baum et al. (1988).

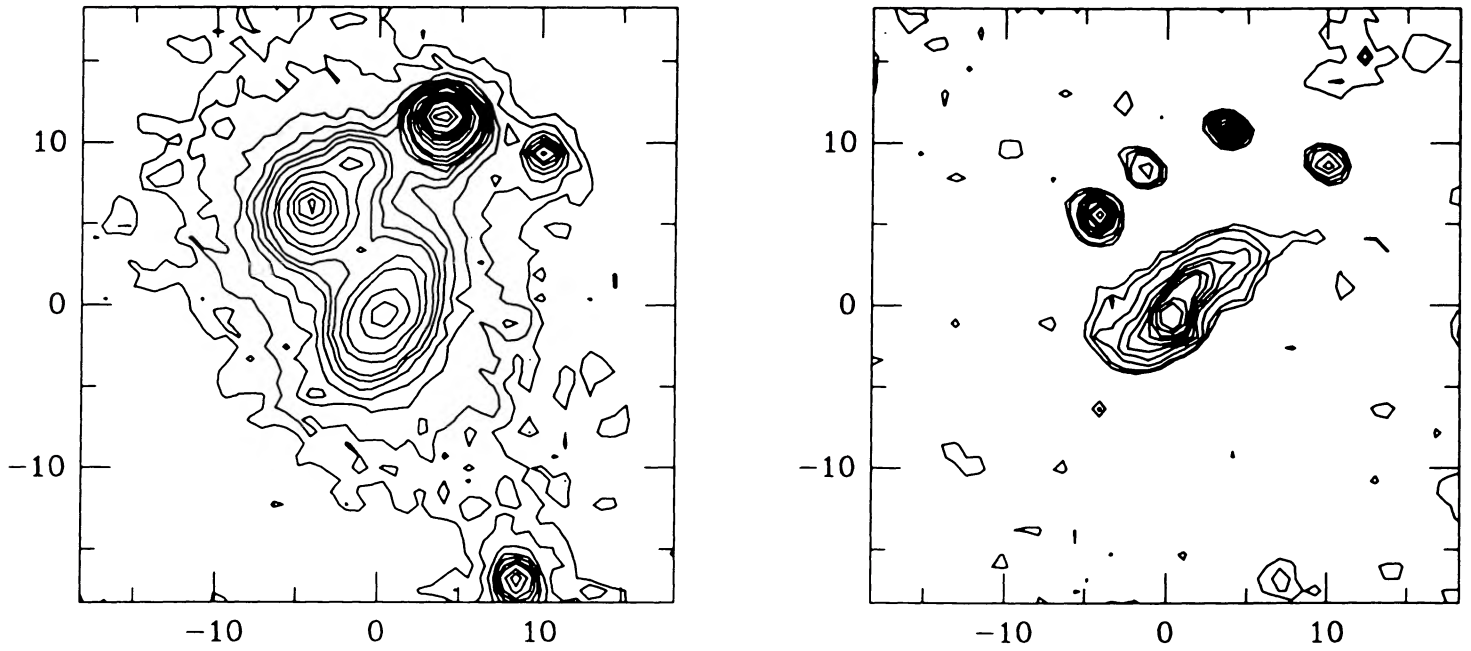

FIG. 3.—3C 433 in Hα + [N II] and r_S. We have no flux calibration for this image. A calibrated image is given in Baum et al. (1988).

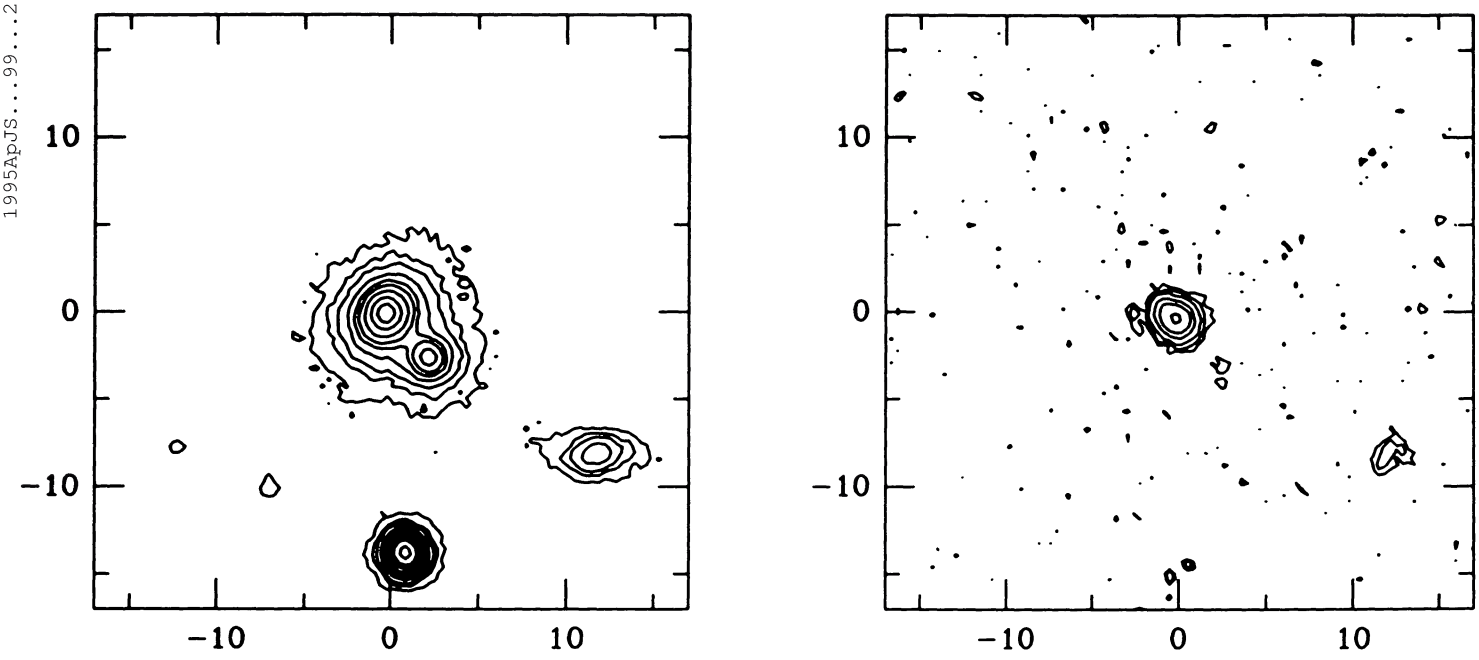

FIG. 4.—3C 135 in Hα and R. The contour levels in the [O II] image in 10^{-17} ergs s^{-1} cm^{-2} arcsec^{-2} are 10, 15, 20, 40, 100, 200, and 500.

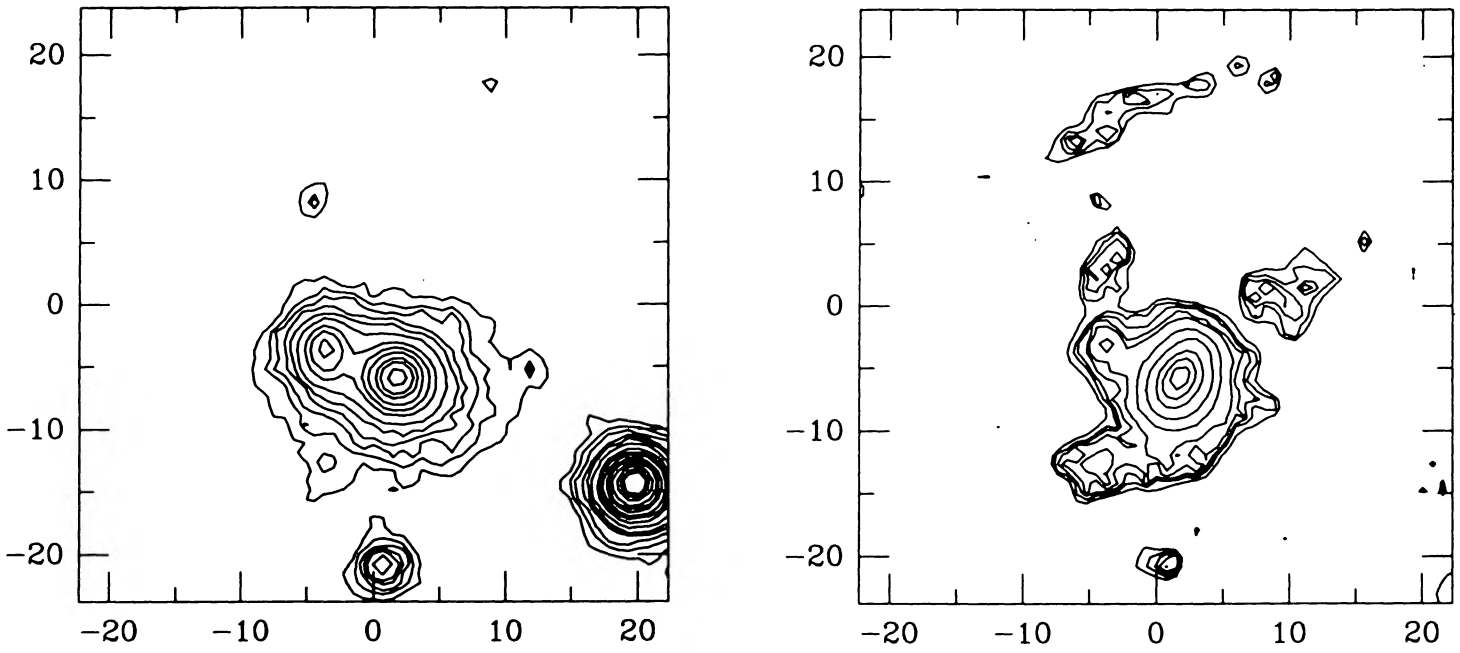

FIG. 5.—3C 381 in [O III] and r_S. The contour levels in the [O III] image in units of 10^{-17} ergs s^{-1} cm^{-2} arcsec^{-2} are 3, 4, 5, 6, 7, 8, 10, 12, 14, 16, 18, 20, 25, 30, 35, 40, 50, 60, 70, 80, 100, 150, 200, 250, 300, 350, and 400.

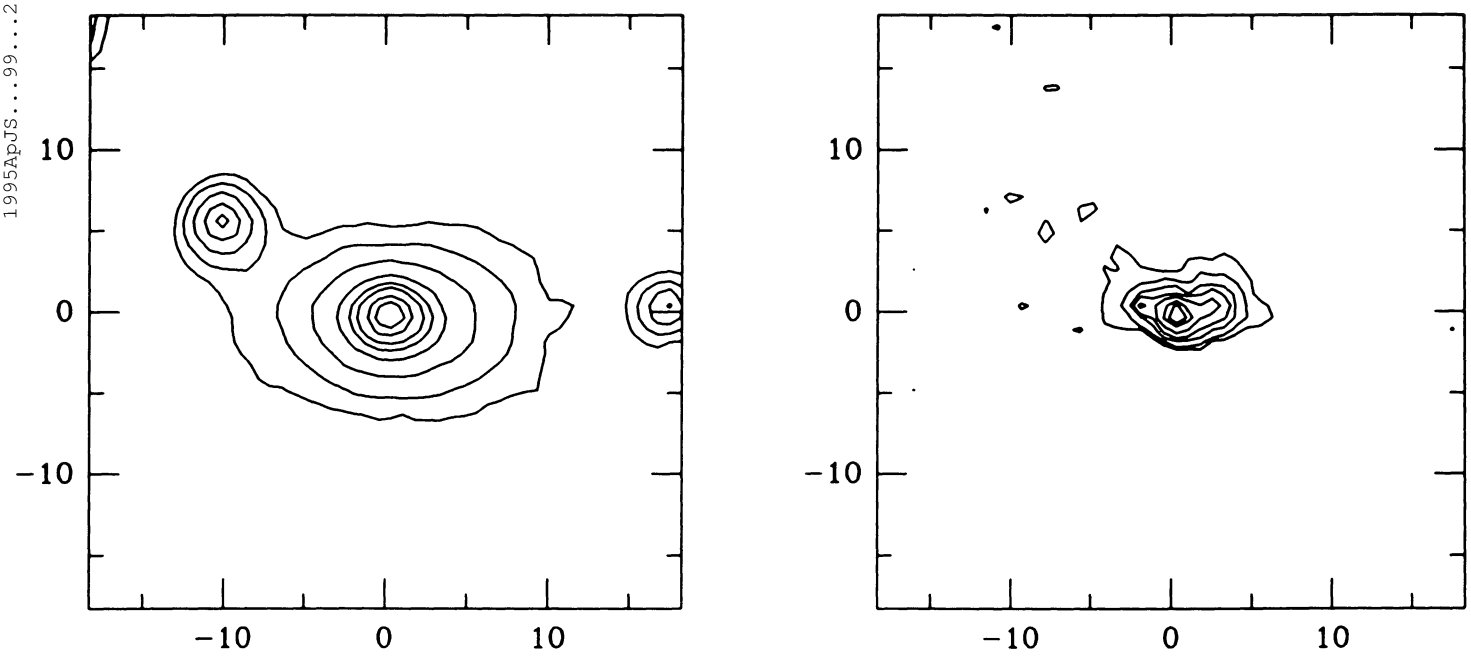

FIG. 6.—3C 357 in [O II] and r_S. We have no flux calibration for this object.

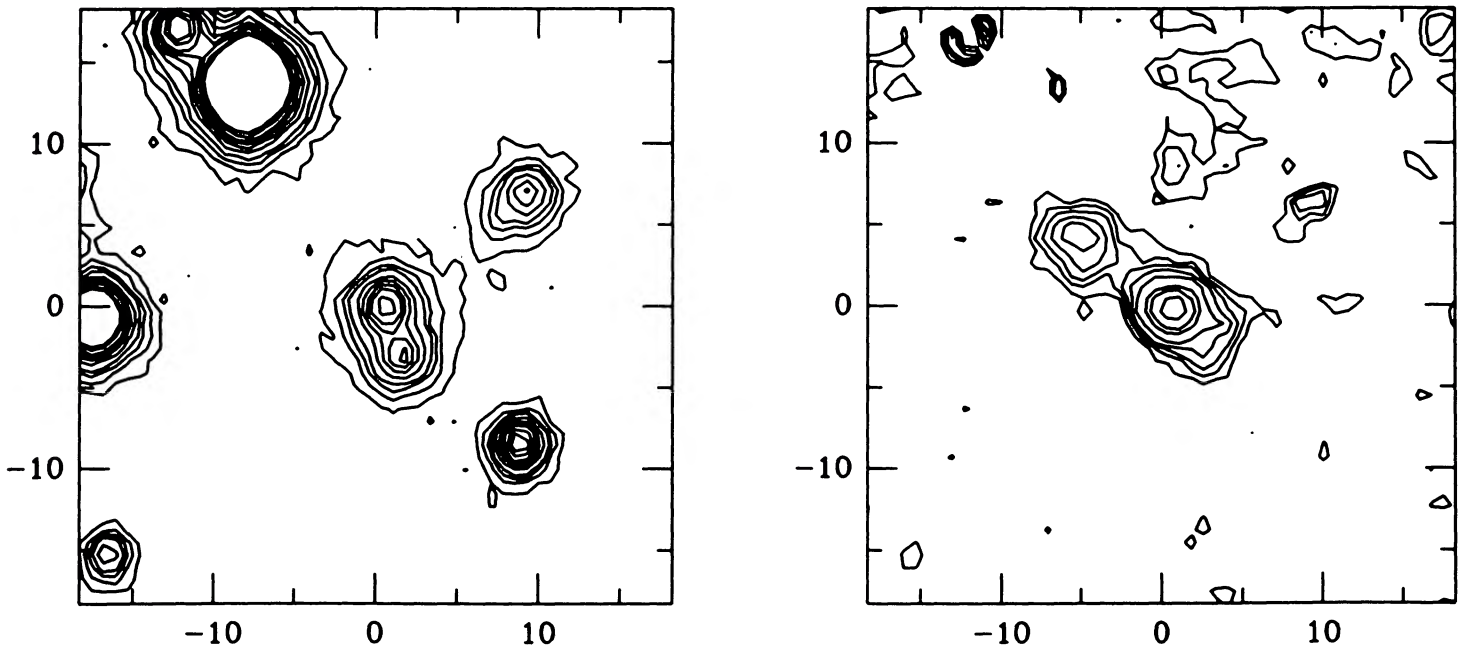

FIG. 7.—3C 33.1 in Hα and R. The contour levels in the Hα image in units of 10^{-17} ergs s^{-1} cm^{-2} arcsec^{-2} are 3, 5, 7, 10, 15, 35, 55, and 100.

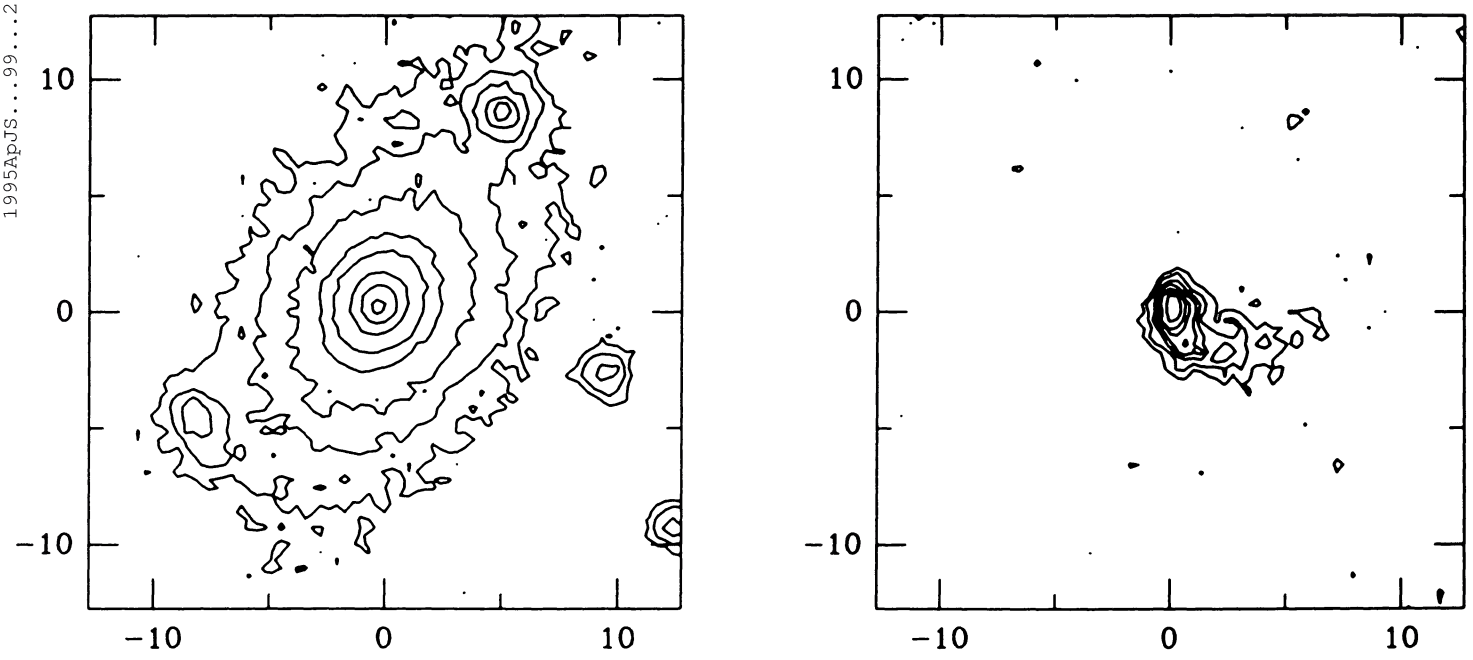

FIG. 8.—3C 28 in Hα and R. We have no flux calibration for this object.

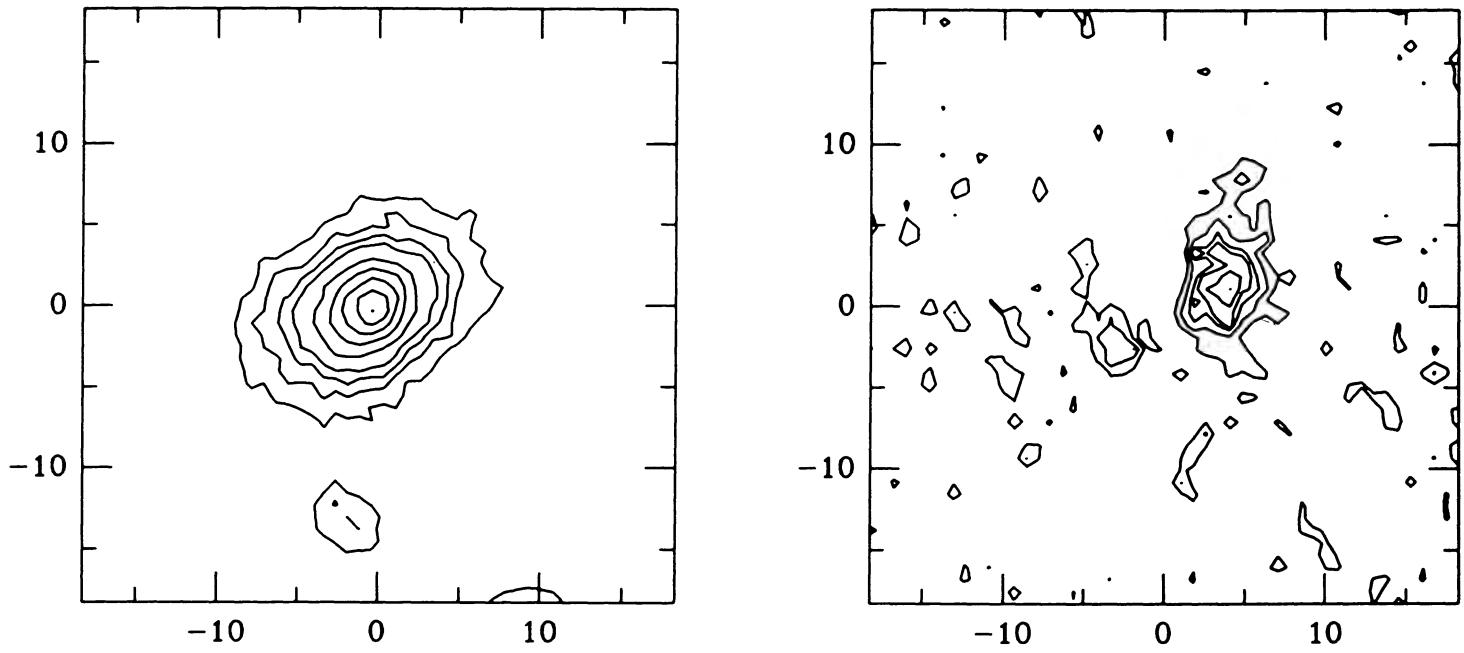

FIG. 9.—3C 180 in [O II] and R. The contour levels in the [O II] image in units of 10^{-17} ergs s^{-1} cm^{-2} arcsec^{-2} are 1, 2, 3, 4, 6, 10, 14, 20, 30, and 38.

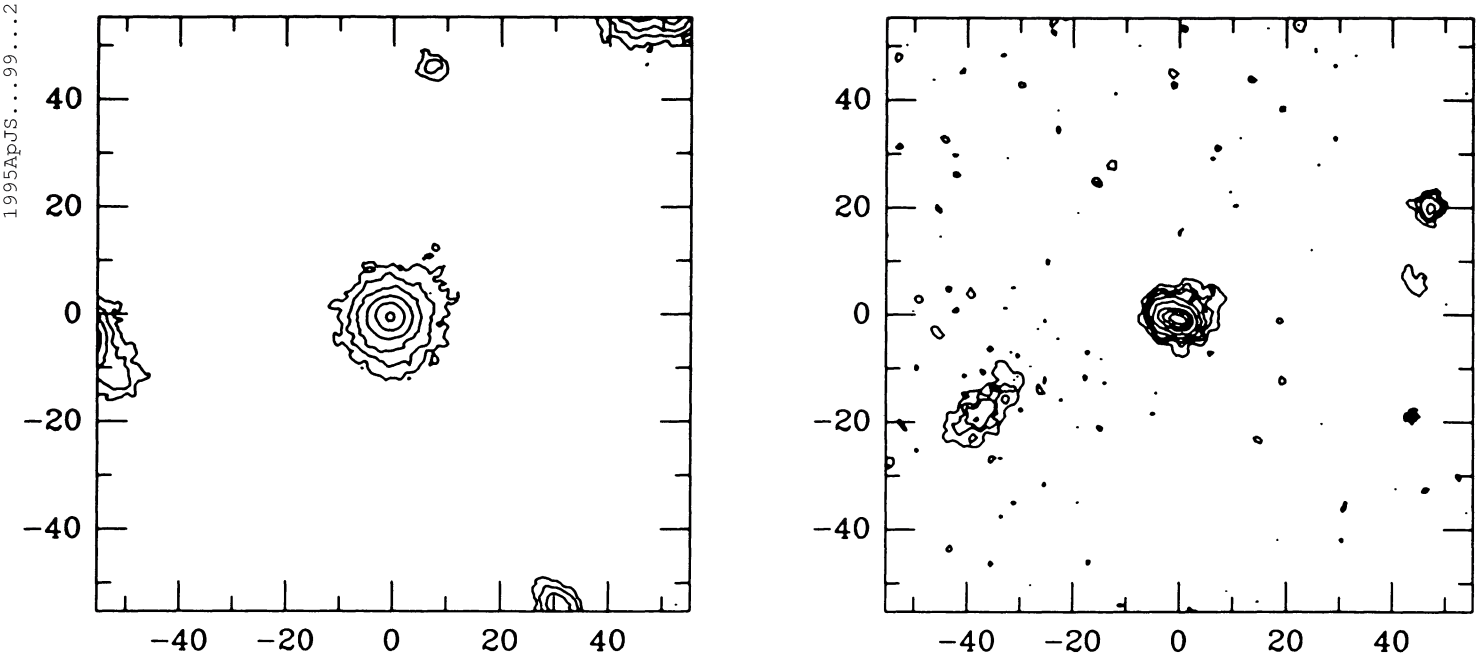

FIG. 10.—3C 284 in [O II] and R. The contour levels in the [O II] image in units of 10^{-17} ergs s^{-1} cm^{-2} equivalent Hα emission arcsec^{-2} are approximately 0.3, 0.6, 0.8, 1.4, 2.8, 5.5, 11, 17, and 25.

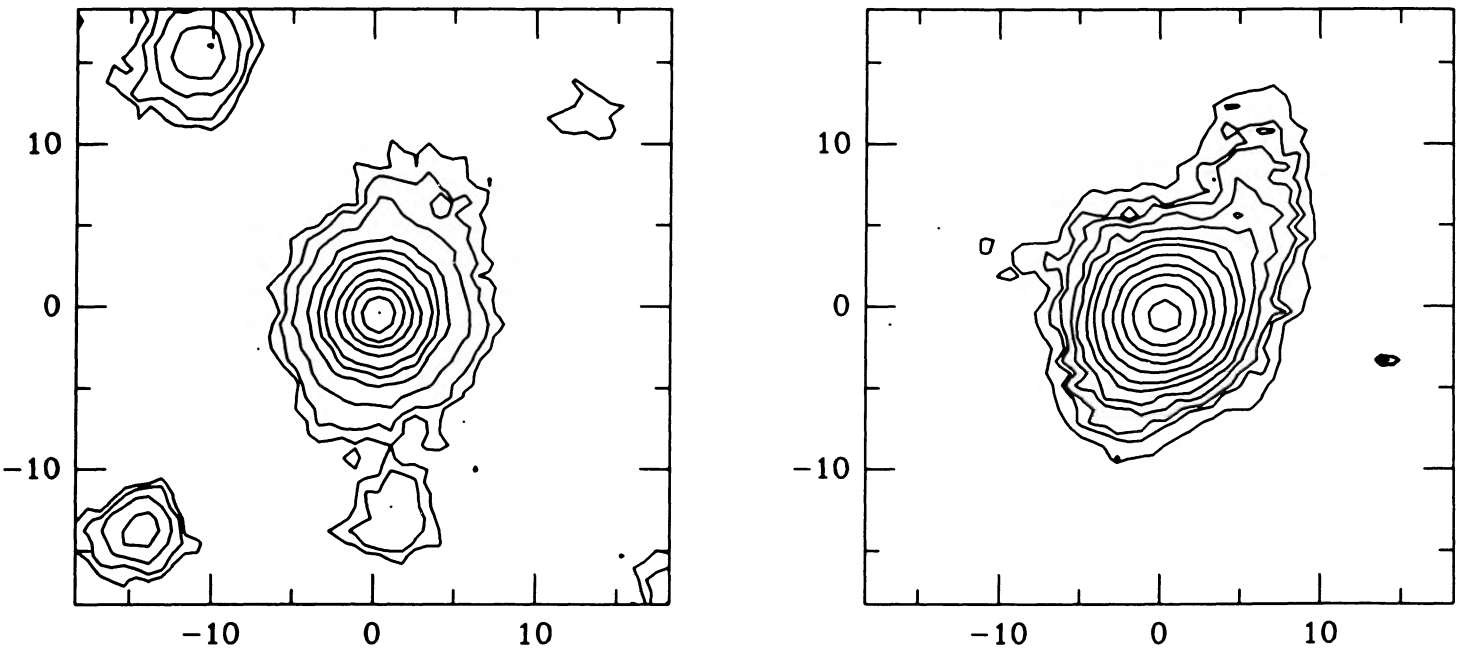

FIG. 11.—3C 79 in [O III] and r_S. The contour levels in the [O III] image in units of 10^{-17} ergs s^{-1} cm^{-2} arcsec^{-2} are 1, 1.5, 2, 3, 4, 6, 8, 12, 1, 25, 35, and 50.

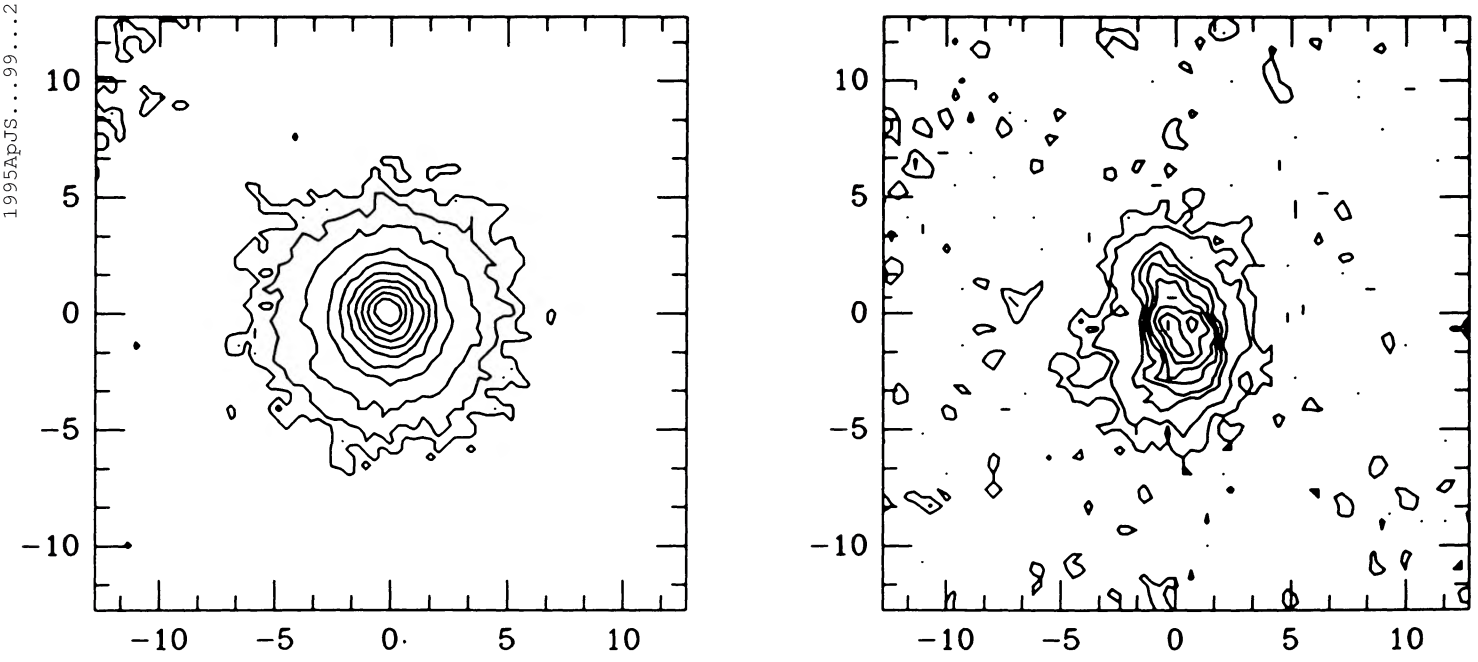

FIG. 12.—3C 379.1 in [O III] and r_S. No flux calibration is available for this object.

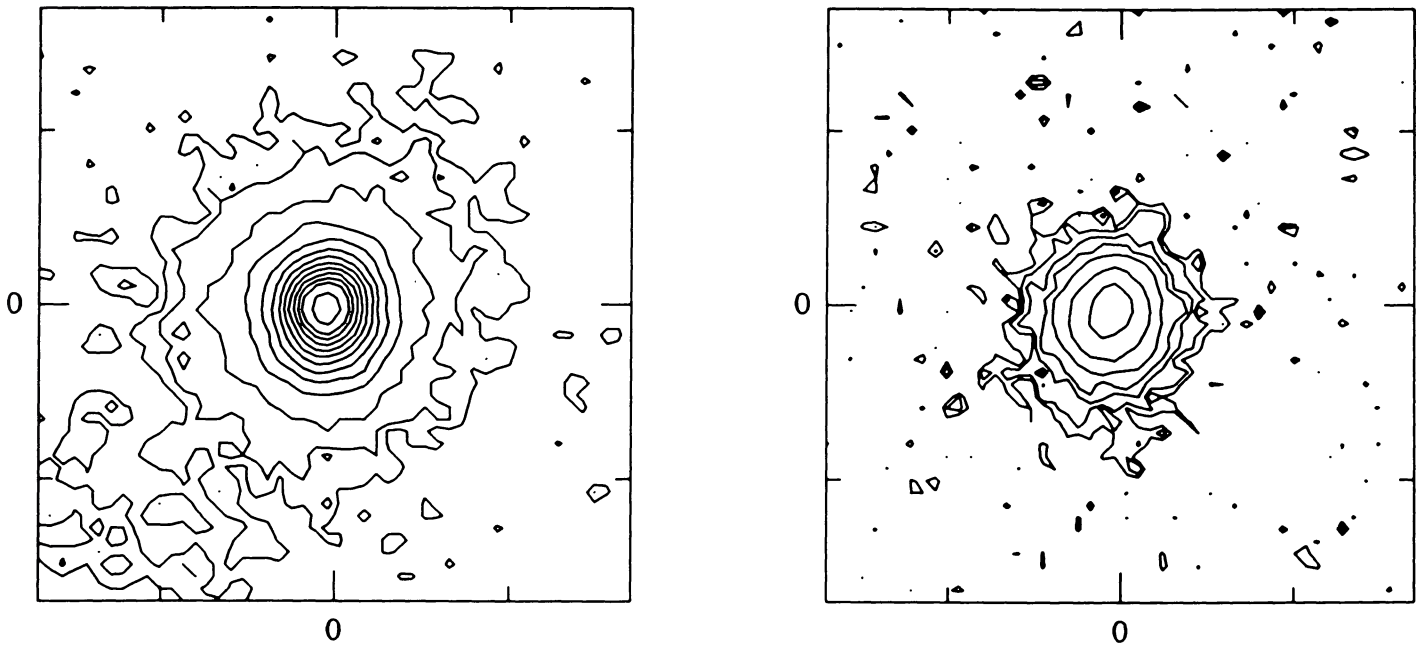

FIG. 13.—3C 303.1 in [O III] and R. The contour levels in the [O III] image in units of 10^{-17} ergs s^{-1} cm^{-2} arcsec^{-2} are 16, 24, 40, 60, 100, 200, 400, 600, and 800. The size of each image is $17'' \times 17''$.

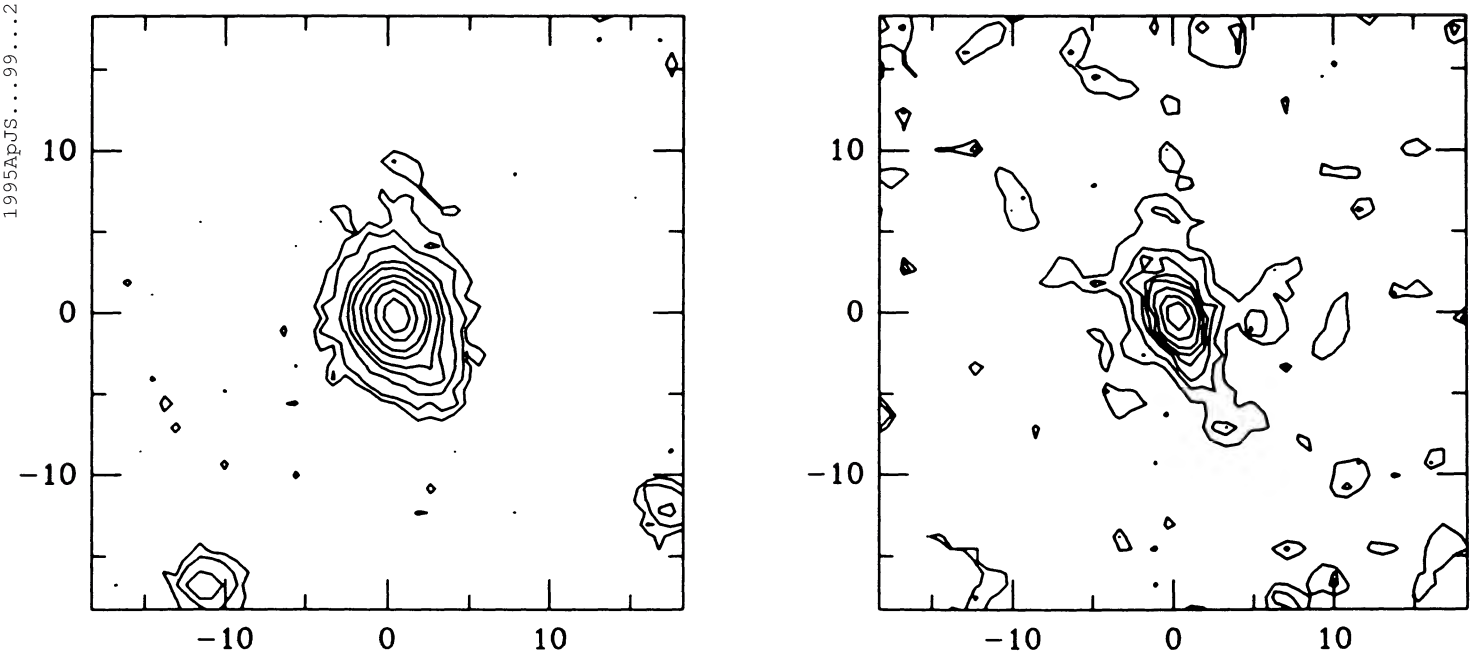

FIG. 14.—3C 460 in [O III] and r_S. The contour levels in the [O III] image in units of 10^{-17} ergs s^{-1} cm^{-2} $arcsec^{-2}$ are 1, 2, 4, 6, 8, 12, 18, and 25.

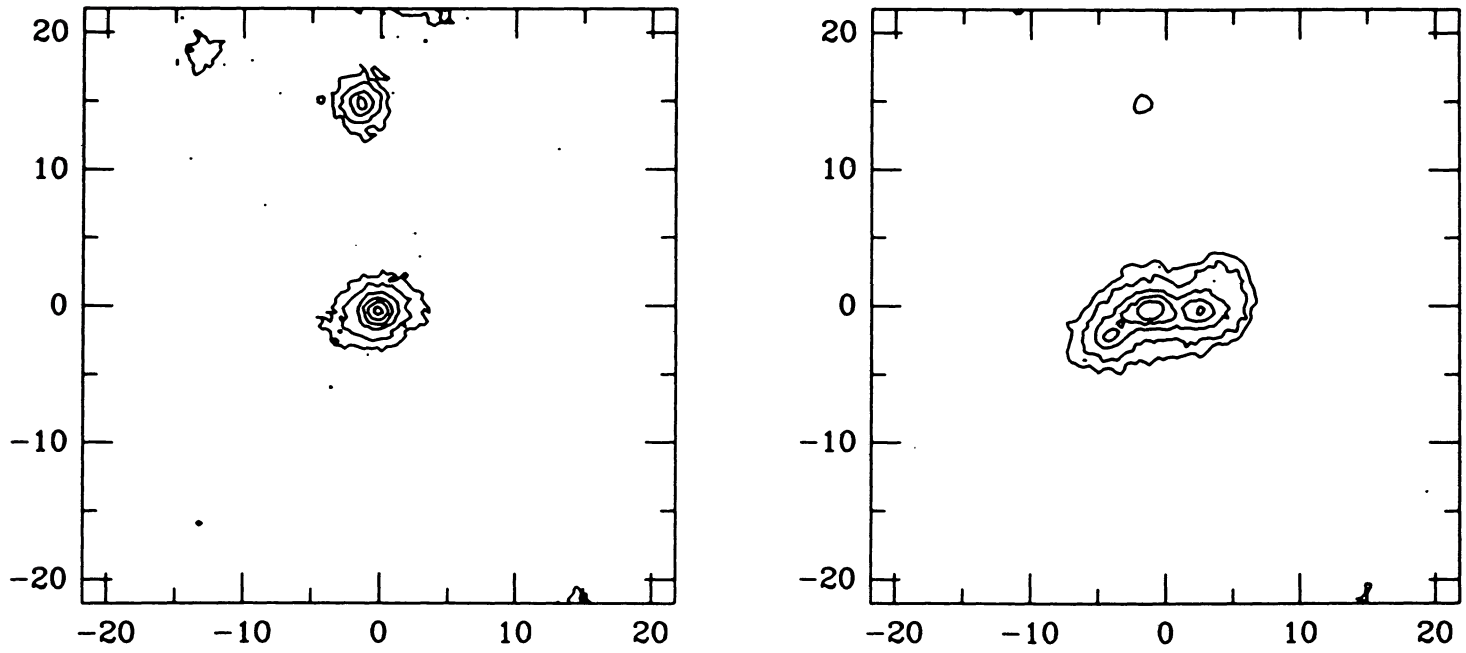

FIG. 15.—3C 300 in [O III] and R. The contour levels in the [O III] image in units of 10^{-17} ergs s^{-1} cm^{-2} $arcsec^{-2}$ are 7.5, 27, 60, 100, 139, 200, 250, and 300.

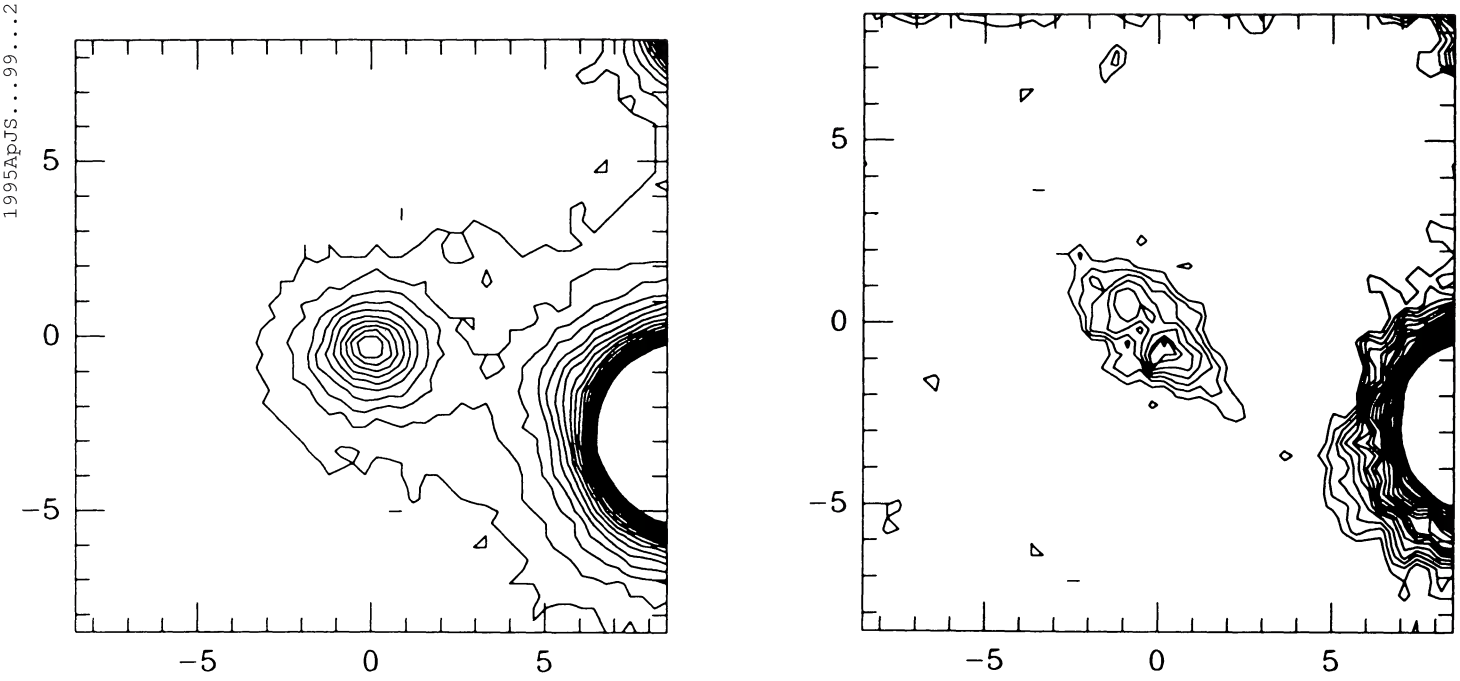

FIG. 16.—3C 153 in Hα and R. The contour levels in the Hα image in units of 10^{-17} ergs s^{-1} cm^{-2} arcsec^{-2} are 5, 7.5, 10, 12.5, 15, 17.5, 20, and 22.5.

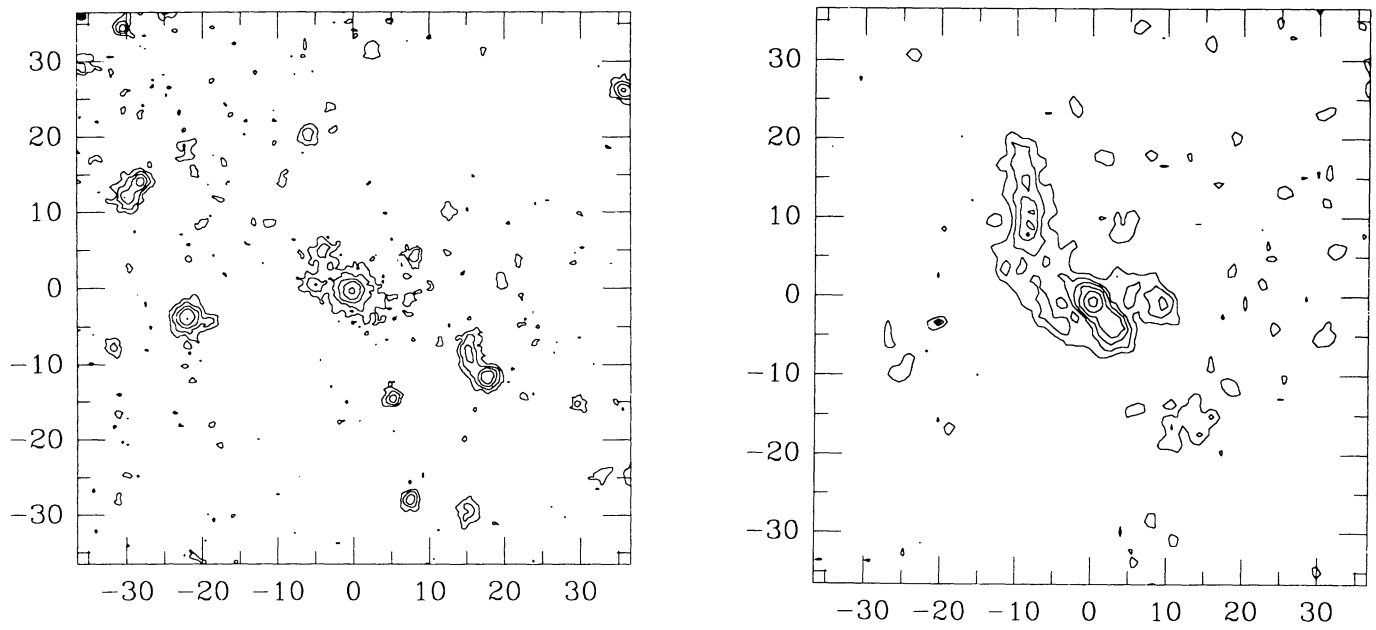

FIG. 17.—3C 458 in [O II] and V. The contour levels in the [O II] image in units of 10^{-17} ergs s^{-1} cm^{-2} arcsec^{-2} are 0.75, 1.5, 2.5, 4, 8, and 16.

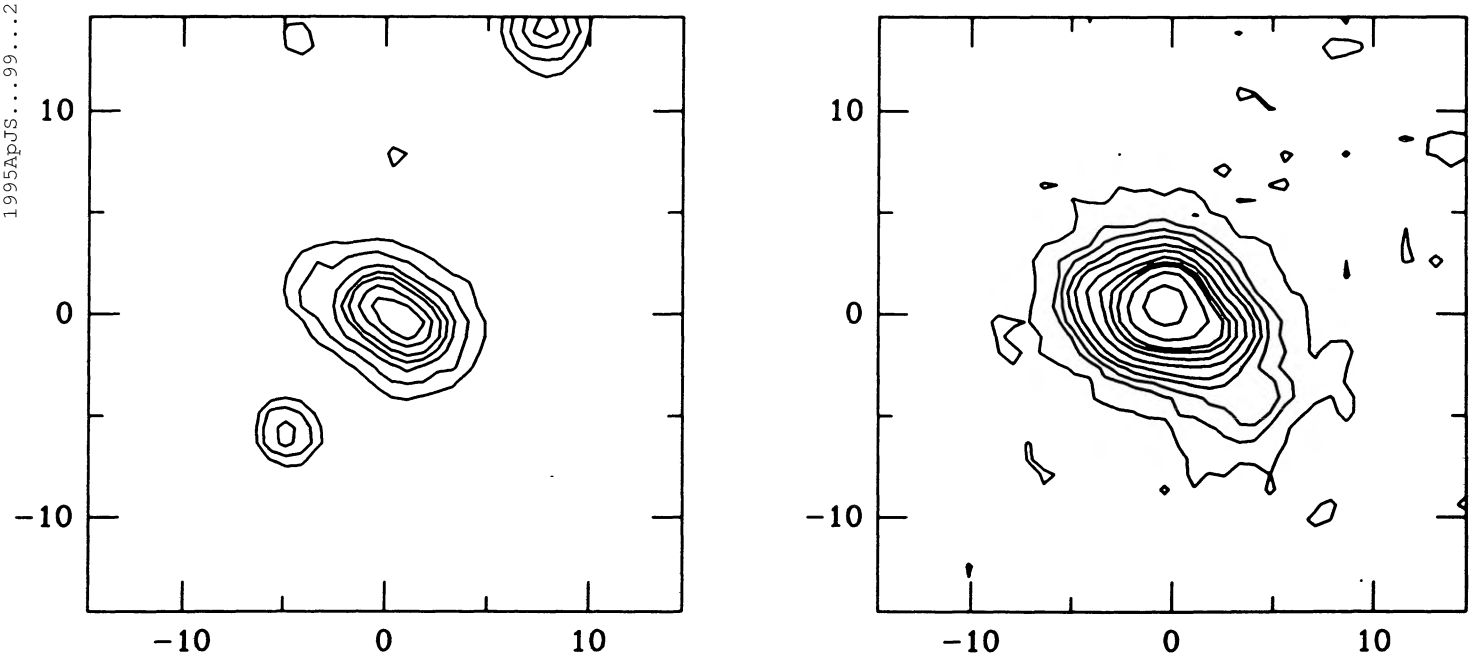

FIG. 18.—3C 299 in [O III] and R. The contour levels in the [O III] image in units of 10^{-17} ergs s^{-1} cm^{-2} arcsec^{-2} are 2.3, 3.5, 5, 8, 12, 16, 20, 30, 50, and 80.

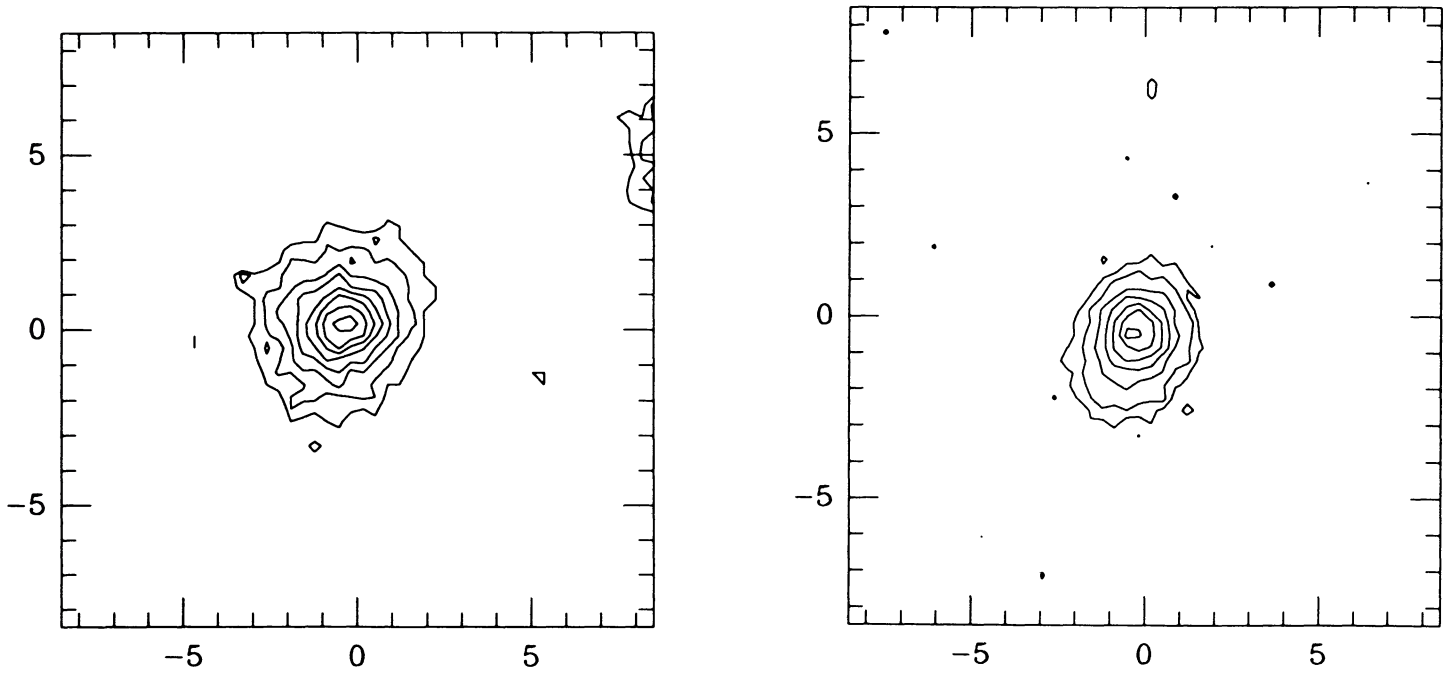

FIG. 19.—3C 268.3 in [O/III] and R. The contour levels in the [O III] image in units of 10^{-17} ergs s^{-1} cm^{-2} arcsec^{-2} are 2.3, 4.6, 9.2, 13.8, 18.4, and 27.

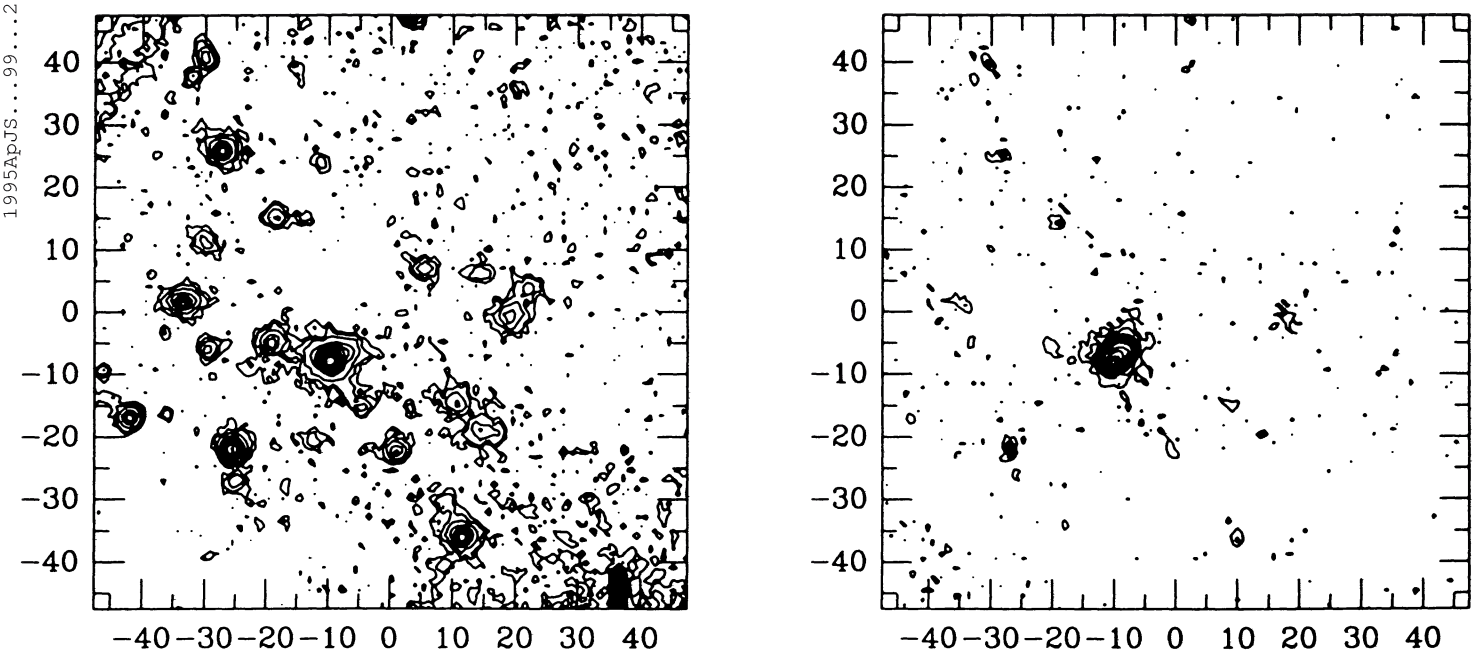

FIG. 20.—3C 244.1 in [O III] and r_S. The contour levels in the [O III] image in units of 10^{-17} ergs s^{-1} cm^{-2} arcsec^{-2} are 14, 28, 43, 57, 71, 85, 100, 114, 143, 214, 286, 357, 428, and 500.

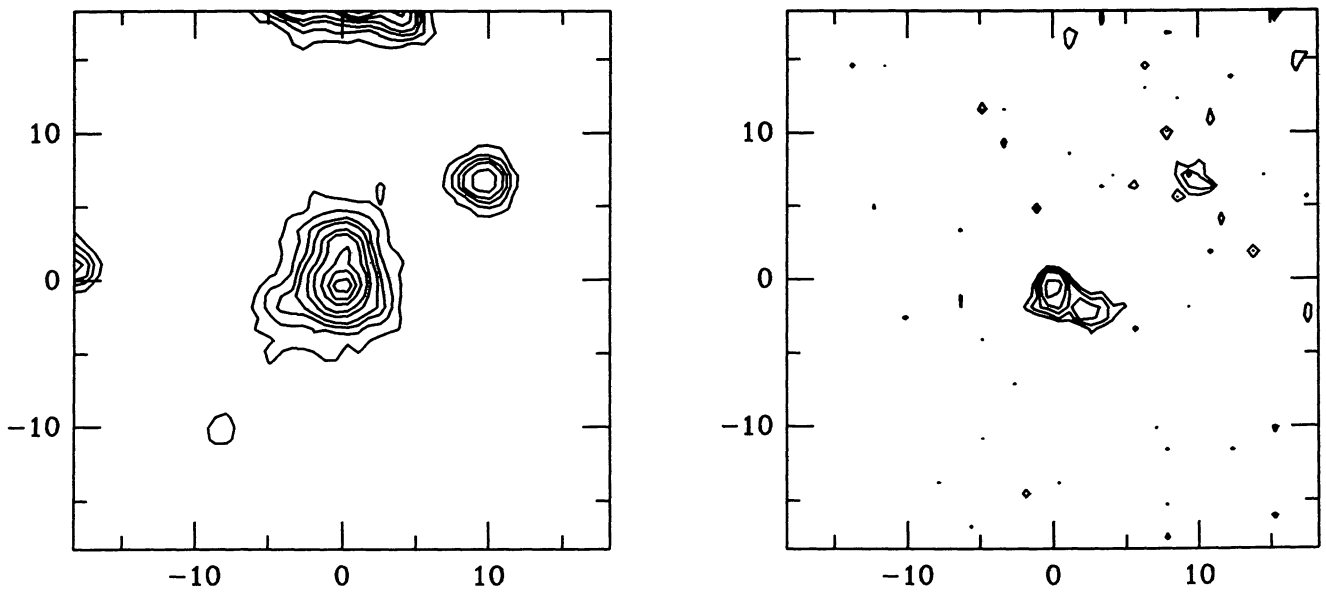

FIG. 21.—3C 306.1 in [O II] and r_S. The contour levels in the [O II] image in units of 10^{-17} ergs s^{-1} cm^{-2} arcsec^{-2} are 10, 15, 20, 25, 35, 45, and 55.

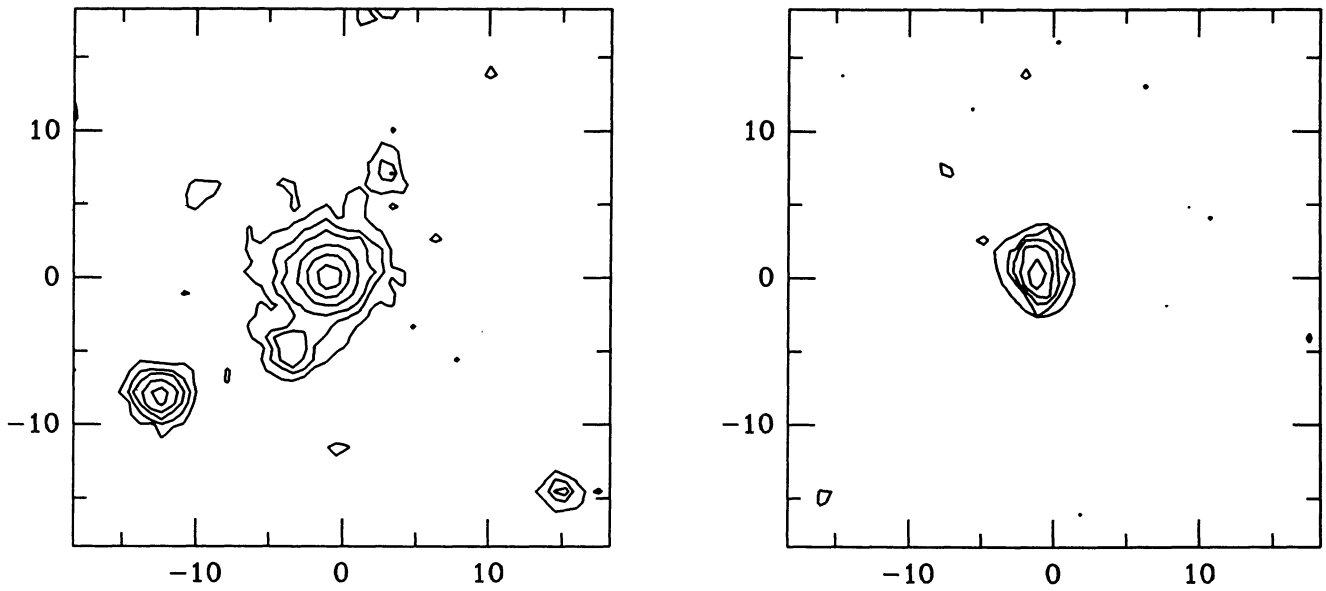

FIG. 22.—3C 341 in [O III] and r_S. The contour levels in the [O III] image in units of 10^{-17} ergs s^{-1} cm^{-2} $arcsec^{-2}$ are 0.75, 1.25, 2, 3, 4, 5, and 7.

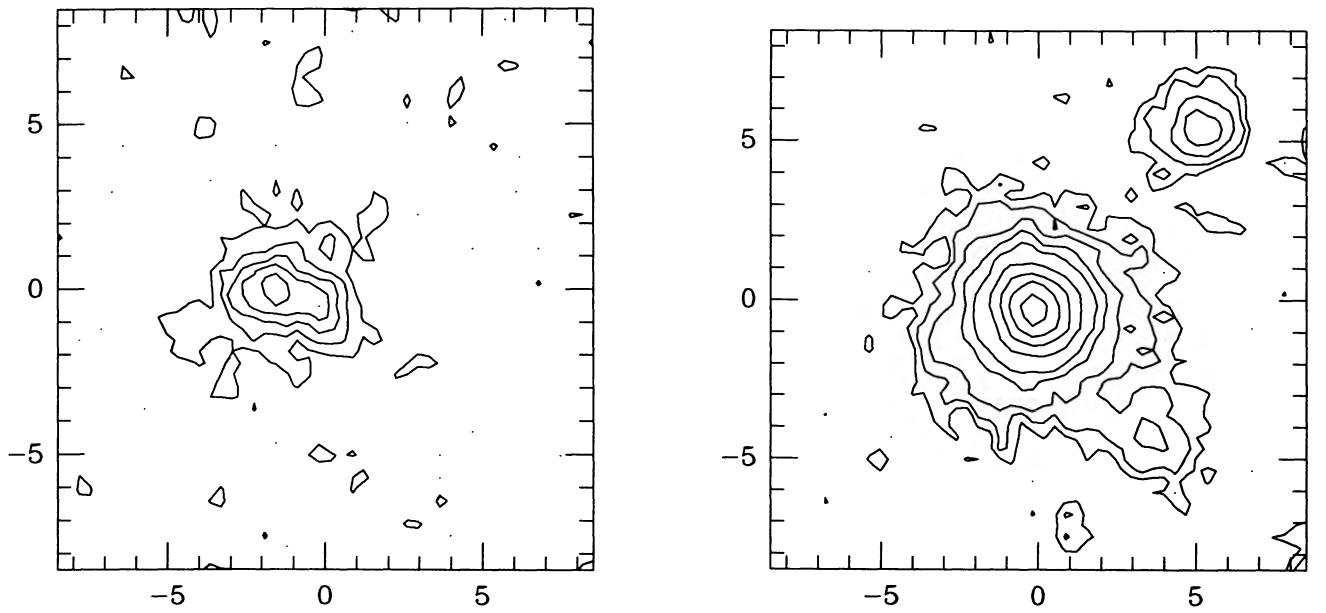

FIG. 23.—3C 313 in [O III] and R. The contour levels in the [O III] image in units of 10^{-17} ergs s^{-1} cm^{-2} $arcsec^{-2}$ are 1, 2, 3, 4, 5, 6, 7, 8, 9, 10, 11, and 12.

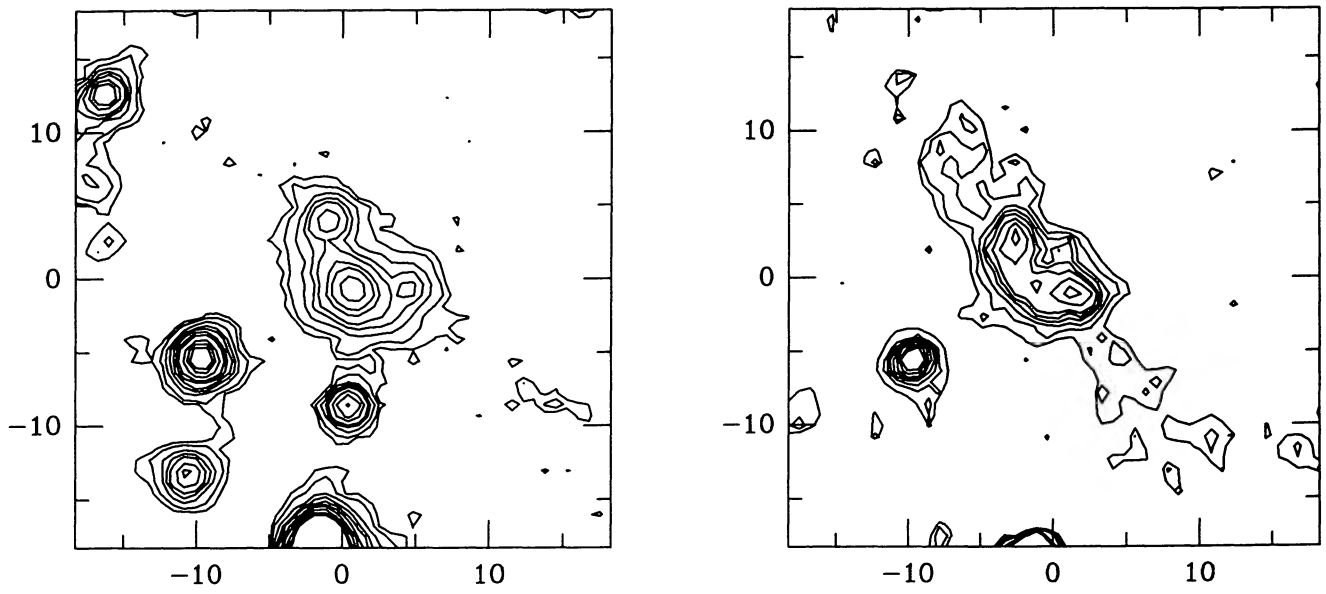

FIG. 24.—3C 435A in [O II] and r_S. The contour levels in the [O II] image in units of 10^{-17} ergs s^{-1} cm^{-2} $arcsec^{-2}$ are 1.5, 3, 5, 7, 9, 12, 18, and 24.

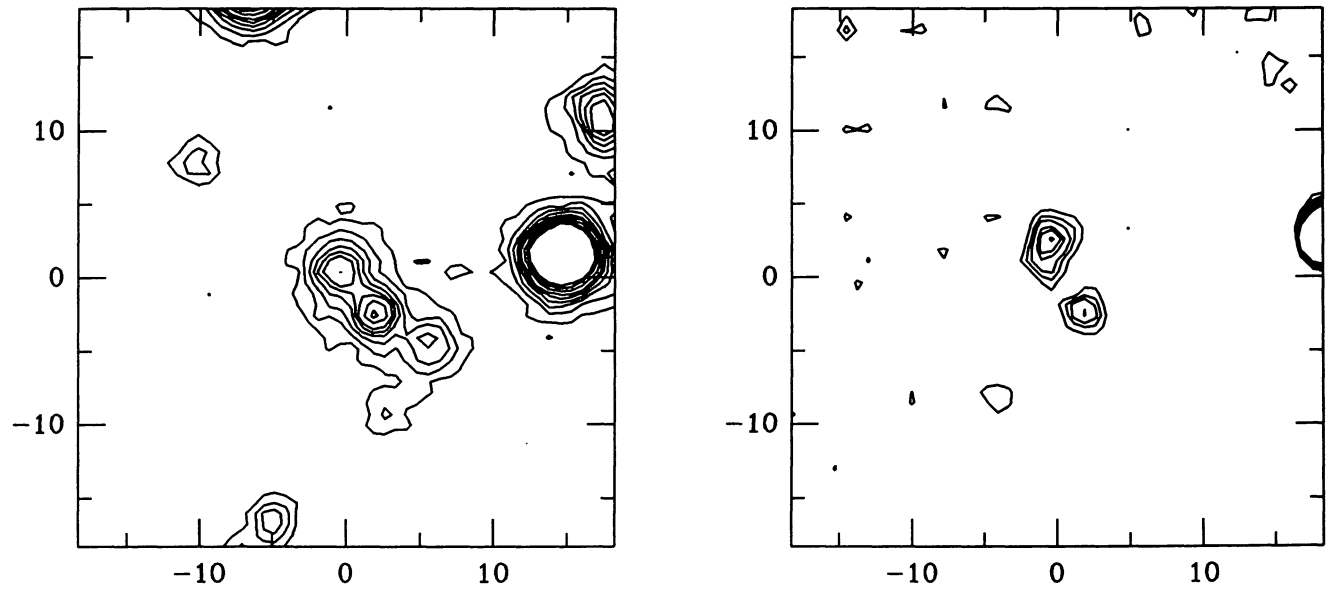

FIG. 25.—3C 172 in [O II] and r_S. The contour levels in the [O II] image in units of 10^{-17} ergs s^{-1} cm^{-2} $arcsec^{-2}$ are 4.5, 7.5, 10, 14, 16, and 20.

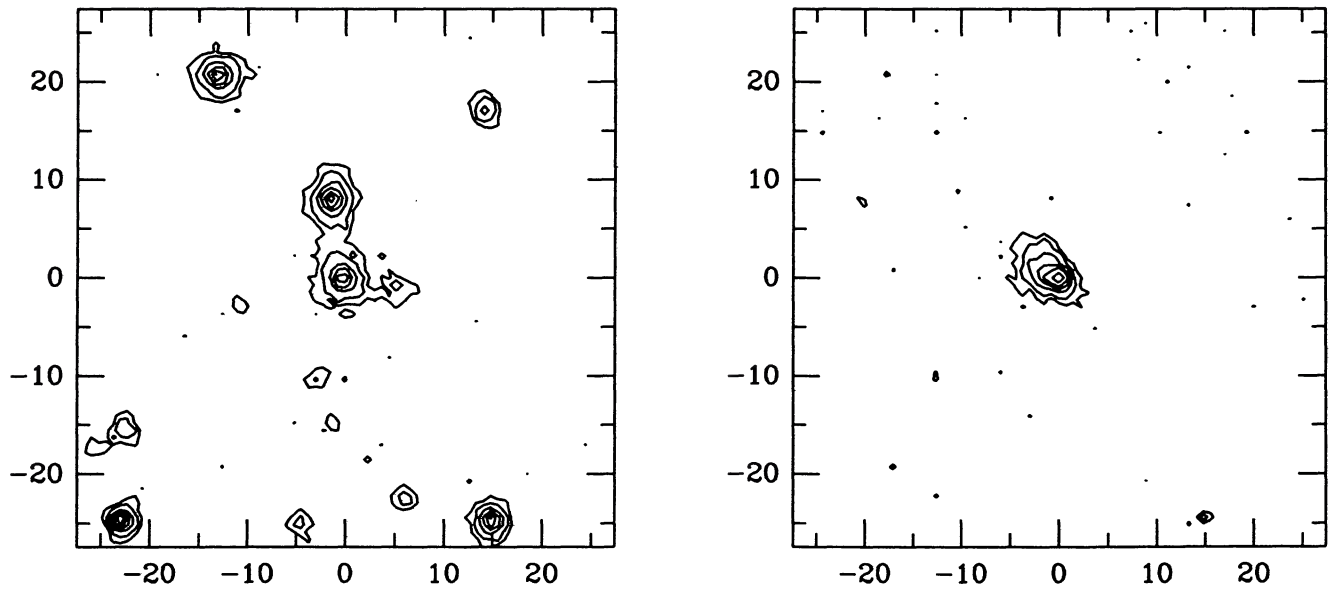

FIG. 26.—3C 330 in [O III] and r_S. The contour levels in the [O III] image in units of 10^{-17} ergs s^{-1} cm^{-2} arcsec^{-2} are 15, 30, 60, 90, 120, and 200.

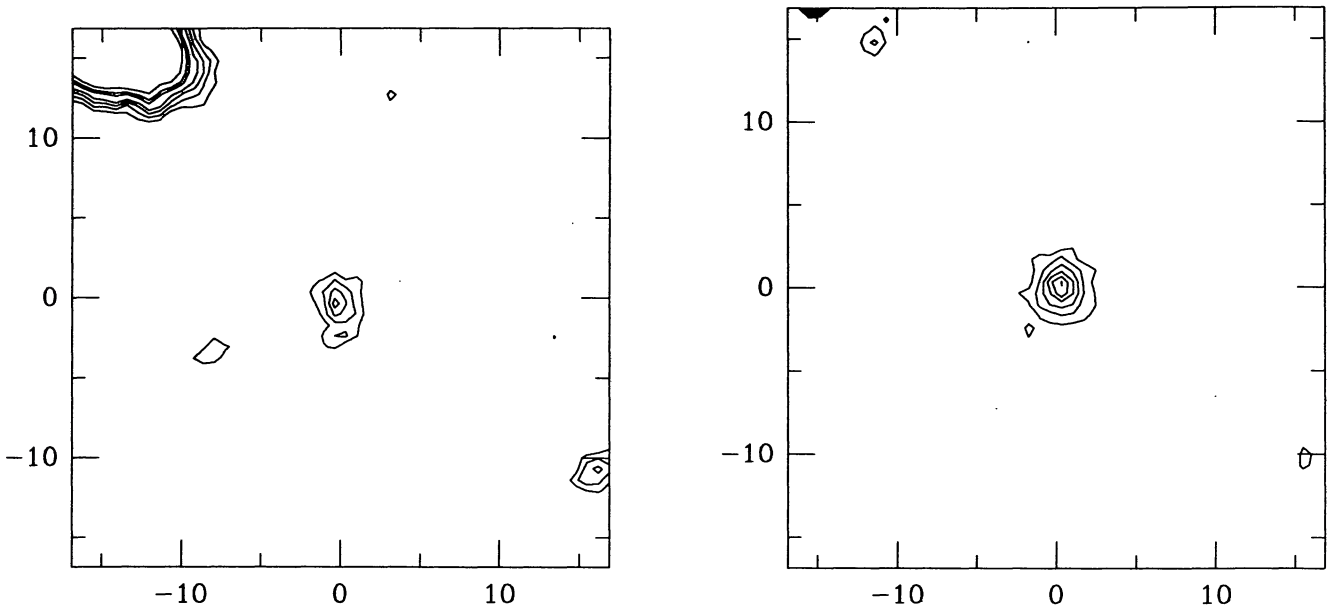

FIG. 27.—3C 228 in [O II] and r_S. We have no flux calibration for this object.

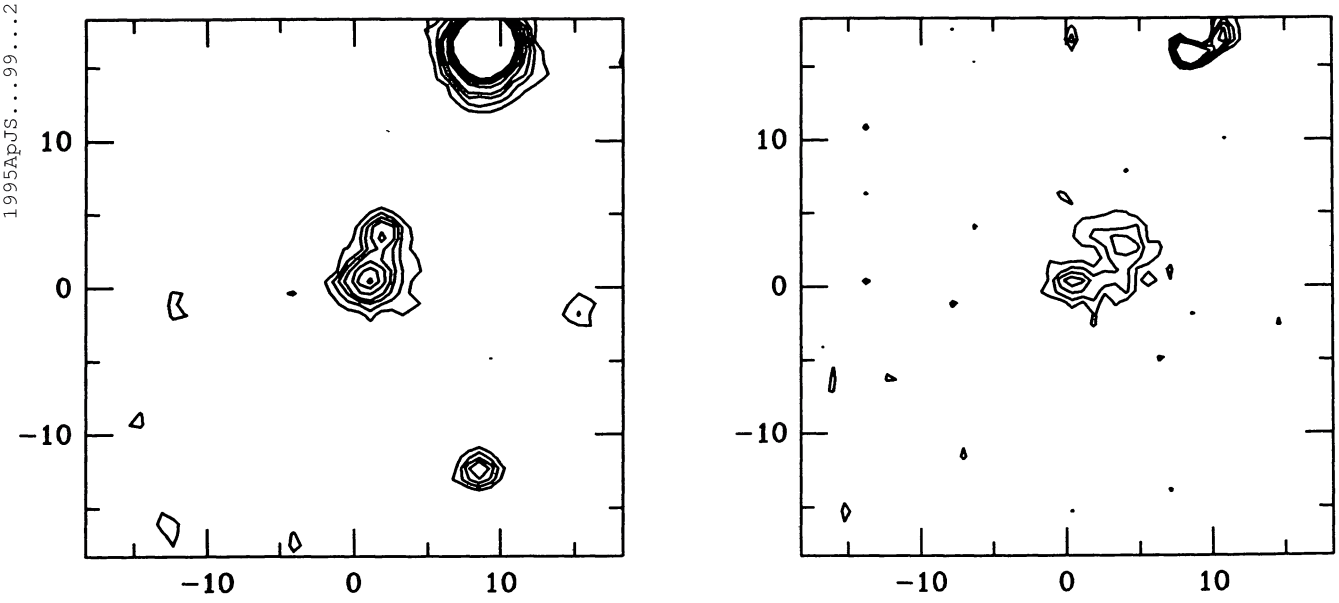

FIG. 28.—3C 169.1 in [O II] and r_S. The contour levels in the [O II] image in units of 10^{-17} ergs s^{-1} cm^{-2} arcsec^{-2} are 6, 23, 32, 42, and 56.

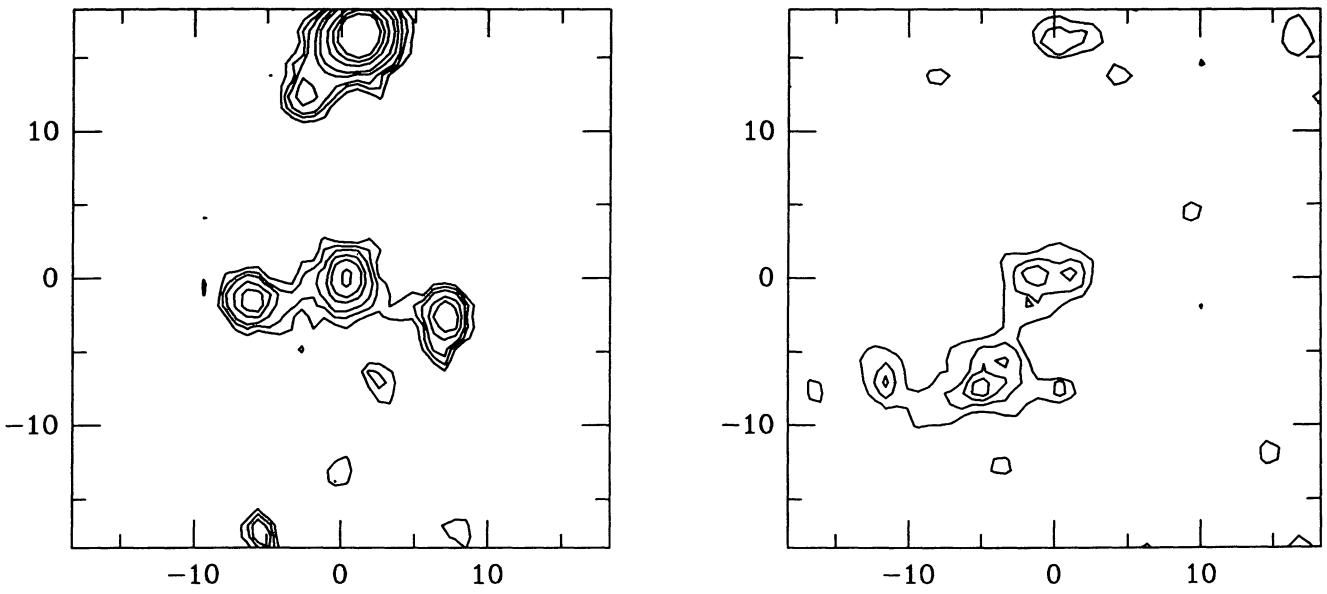

FIG. 29.—3C 337 in [O II] and r_S. We have no flux calibration for this object.

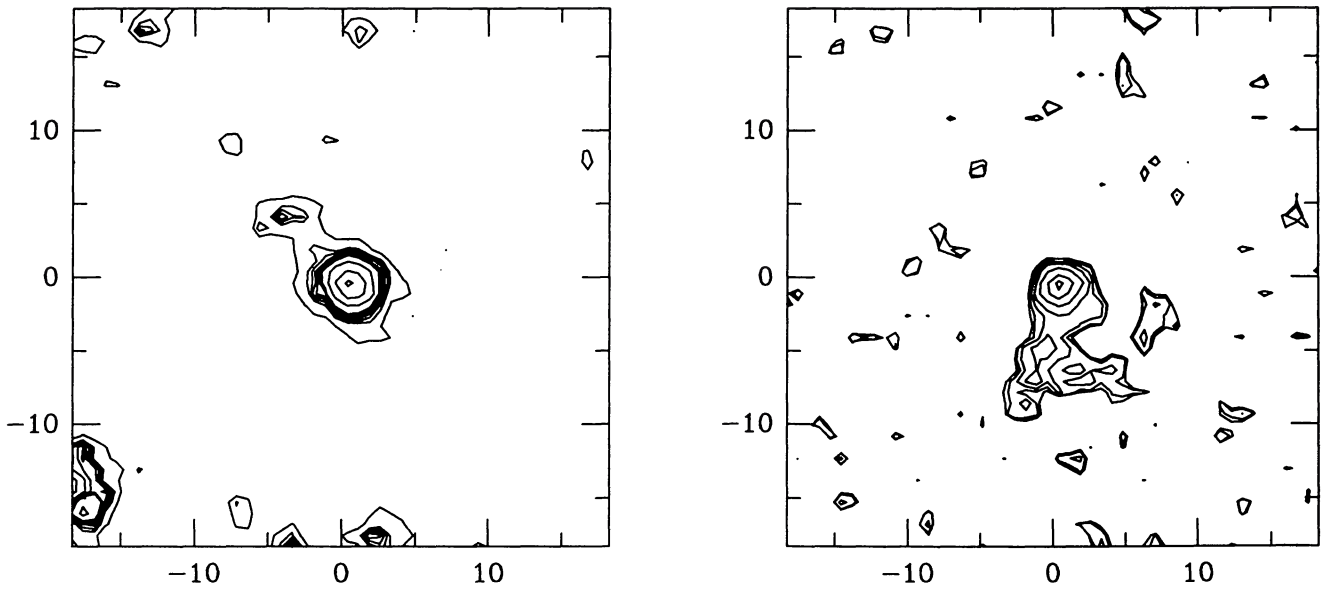

FIG. 30.—3C 44 in [O II] and r_S. The contour levels in the [O II] image in units of 10^{-17} ergs s^{-1} cm^{-2} $arcsec^{-2}$ are 1, 1.3, 2, 3.1, 6.2, 12.3, and 18.5.

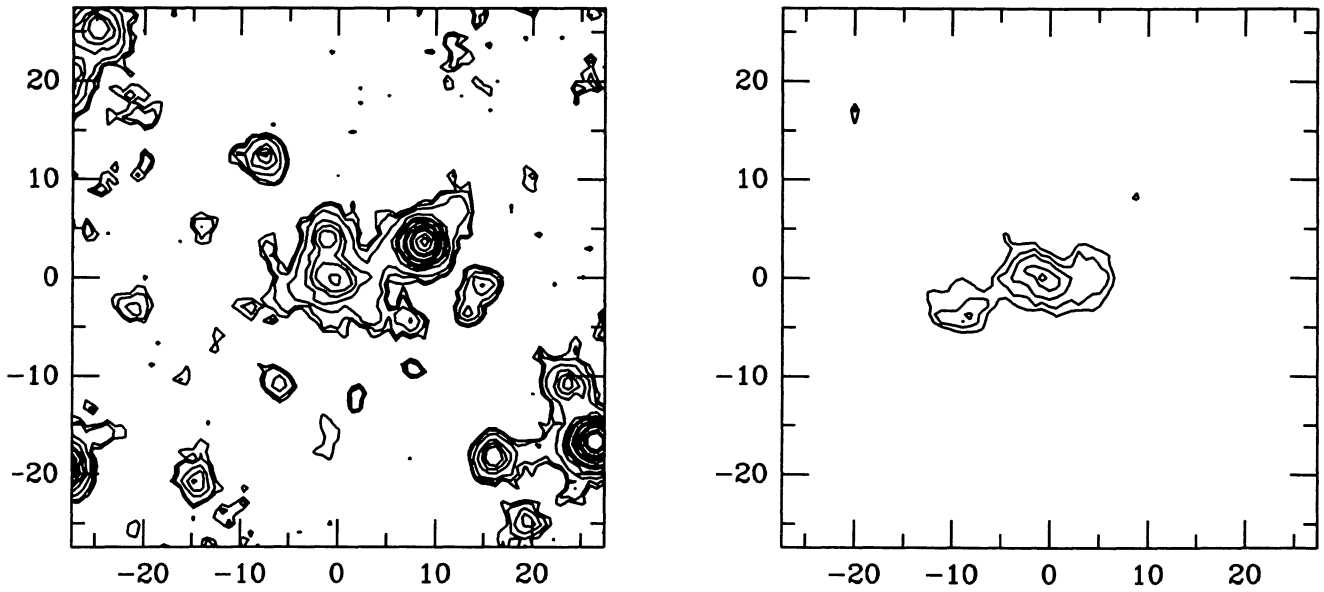

FIG. 31.—3C 34 in [O II] and r_S. The contour levels in the [O II] image in units of 10^{-17} ergs s^{-1} cm^{-2} $arcsec^{-2}$ are 8, 13, 24, 40, and 50.

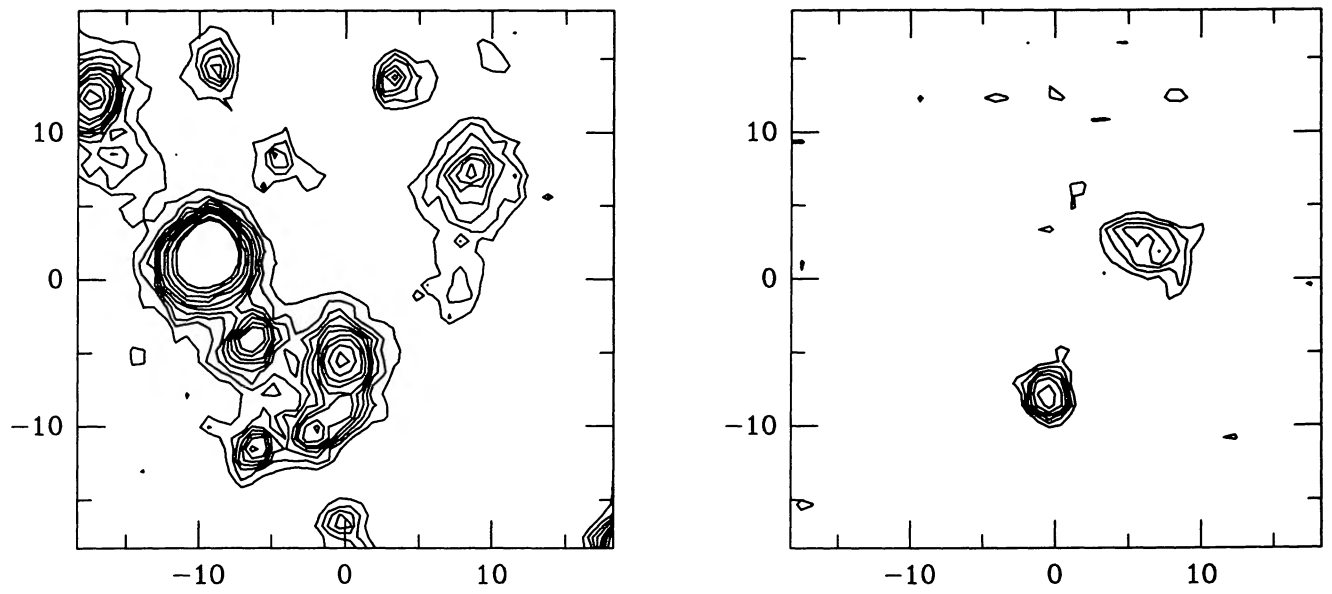

FIG. 32.—3C 441 in [O II] and r_S. The contour levels in the [O II] image in units of 10^{-17} ergs s^{-1} cm^{-2} arcsec^{-2} are 1.2, 1.7, 2.2, 2.7, 3.5, 4.5, and 6.0.

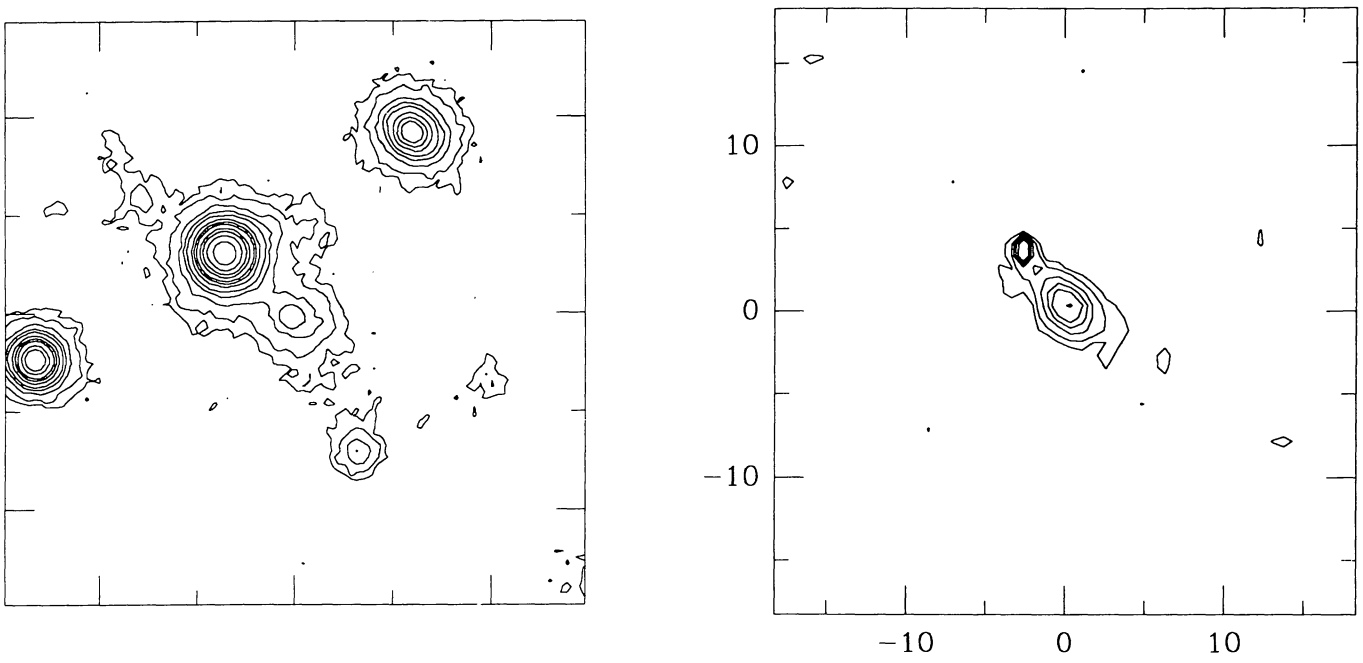

FIG. 33.—3C 247 in [O II] and R. The contour levels in the [O II] image in units of 10^{-17} ergs s^{-1} cm^{-2} arcsec^{-2} are 2.3, 4.6, 9.2, 13.8, 18.4, 27, and 32.

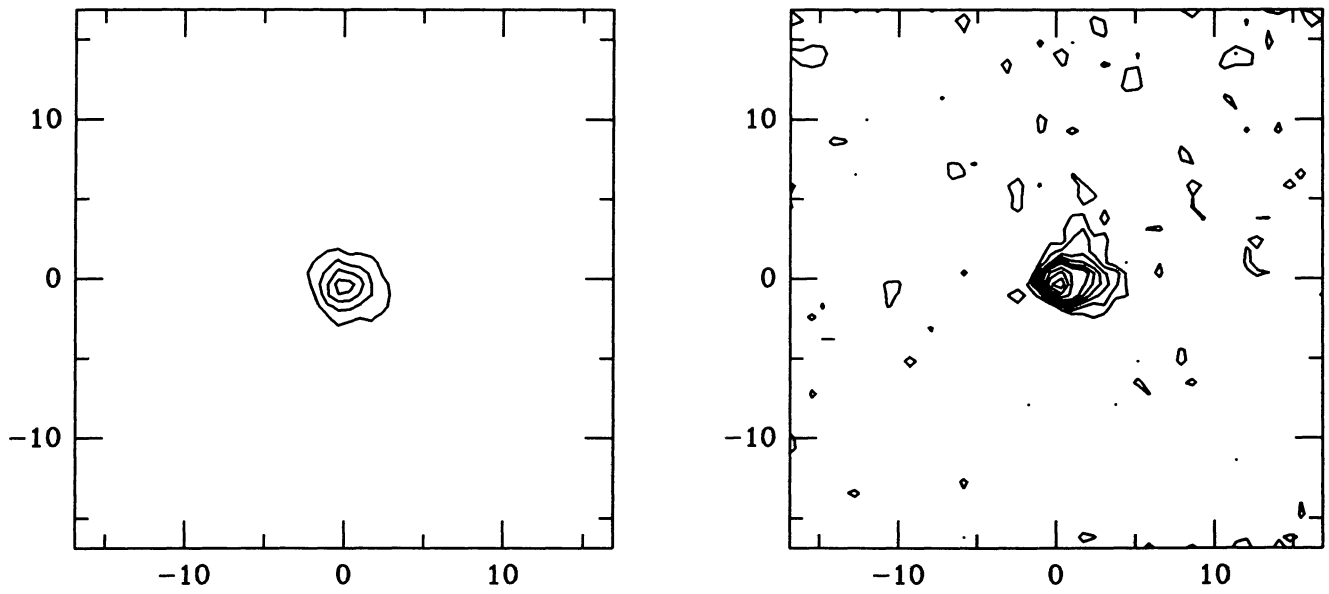

FIG. 34.—3C 343.1 in [O II] and r_S. The contour levels in the [O II] image in units of 10^{-17} ergs s^{-1} cm^{-2} arcsec^{-2} are 1, 2, 3, 4, 5, 6, 8, 10, 12, 14, 16, 18, and 20.

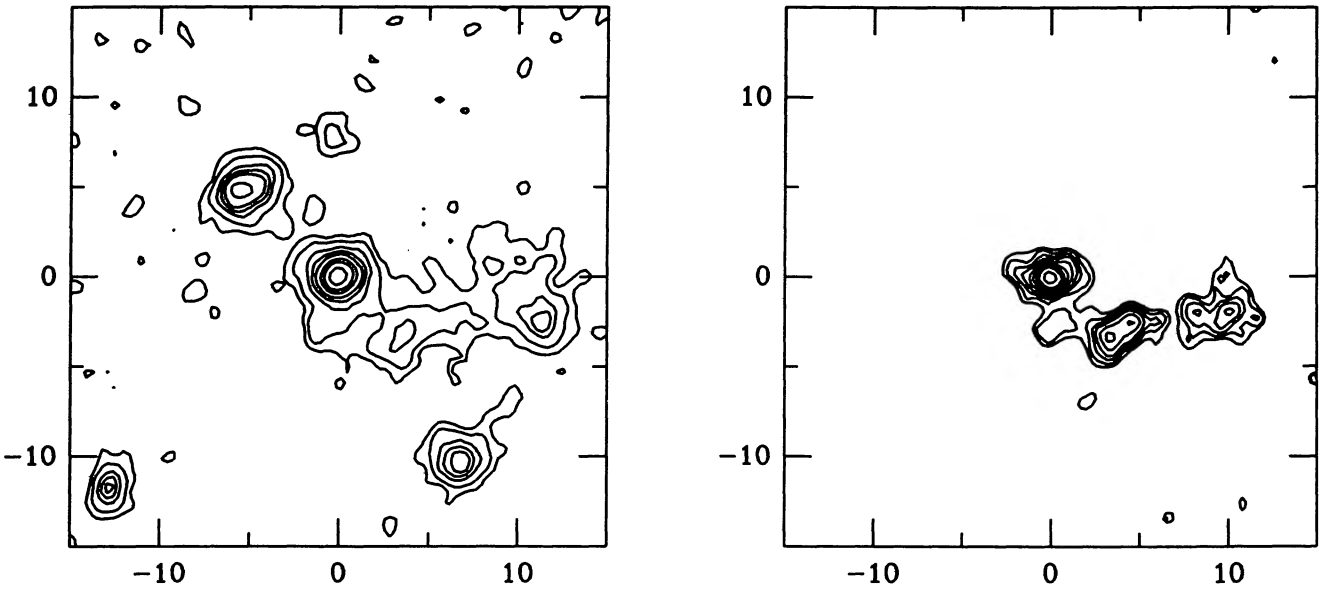

FIG. 35.—3C 277.2 in [O II] and R. The contour levels in the [OII] image in units of 10^{-17} ergs s^{-1} cm^{-2} arcsec^{-2} are 6, 8, 11, 14, 18, 21, 26, 30, and 37.

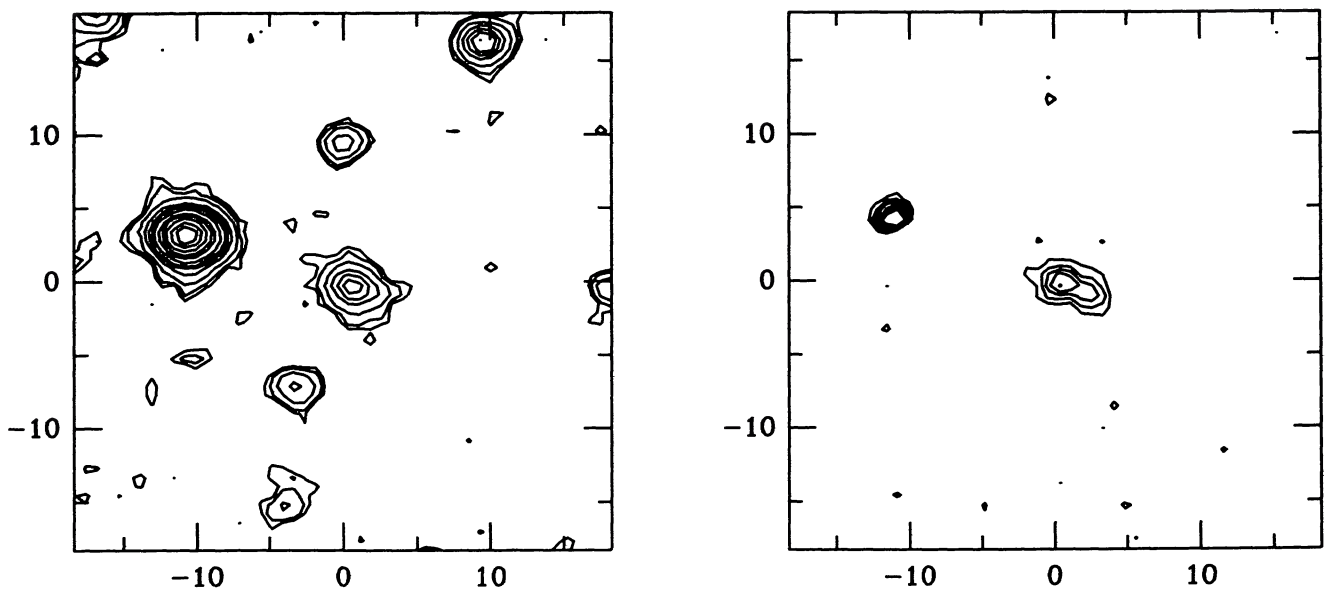

FIG. 36.—3C 340 in [O II] and r_S. The contour levels in the [O II] image in units of 10^{-17} ergs s^{-1} cm^{-2} $arcsec^{-2}$ are 1.6, 2.5, 3.3, 4.2, 5, 5.8, 6.7, 7.5, 8.3, 9.2, 10, and 10.8.

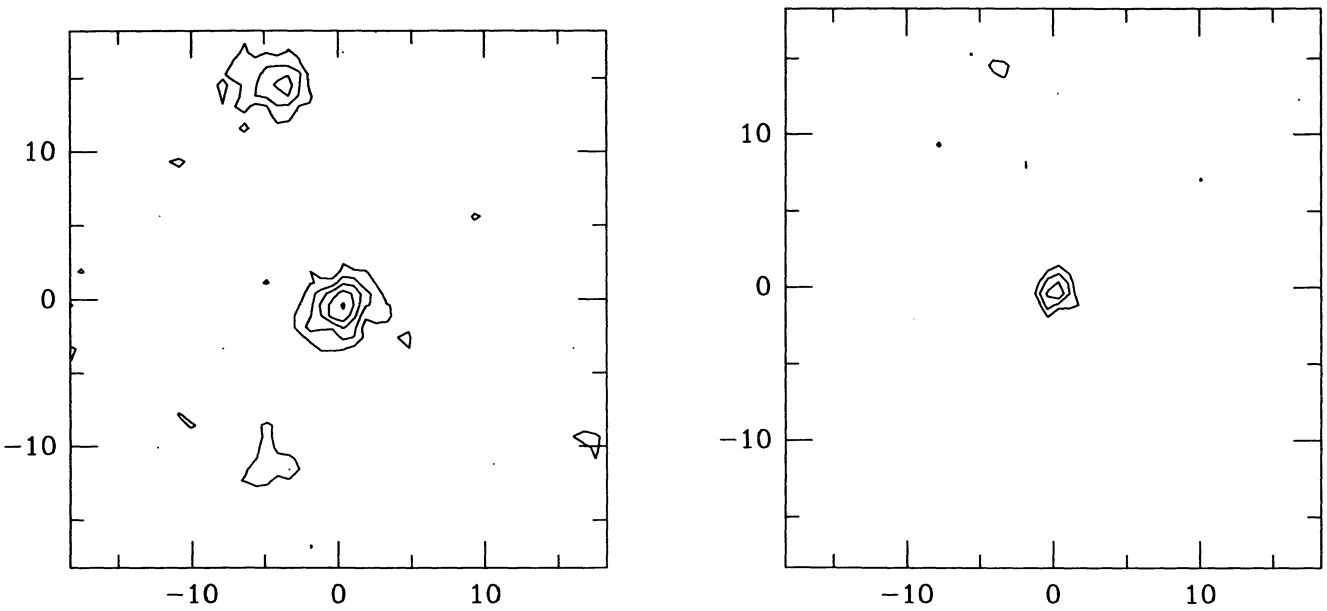

FIG. 37.—3C 41 in [O II] and r_S. The [O II] image shows no extended emission and is uncalibrated.

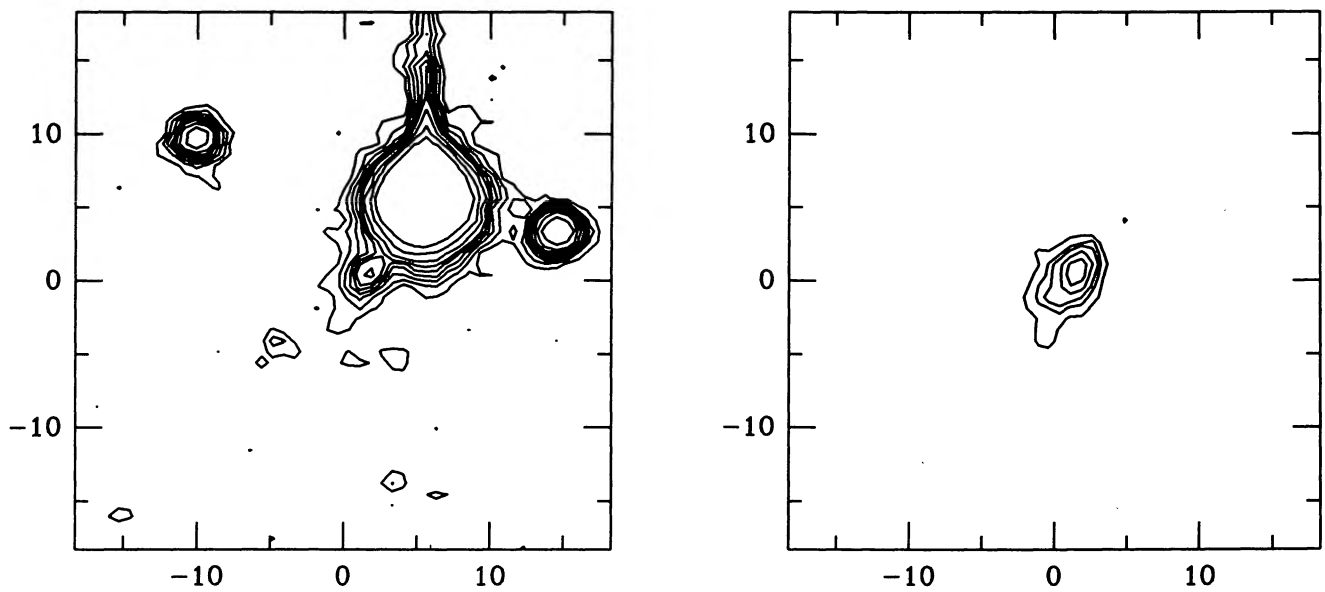

FIG. 38.—3C 352 in [O II] and r_S. The contour levels in the [O II] image in units of 10^{-17} ergs s^{-1} cm^{-2} $arcsec^{-2}$ are 2.6, 3, 4, 8, 12, 20, and 30.

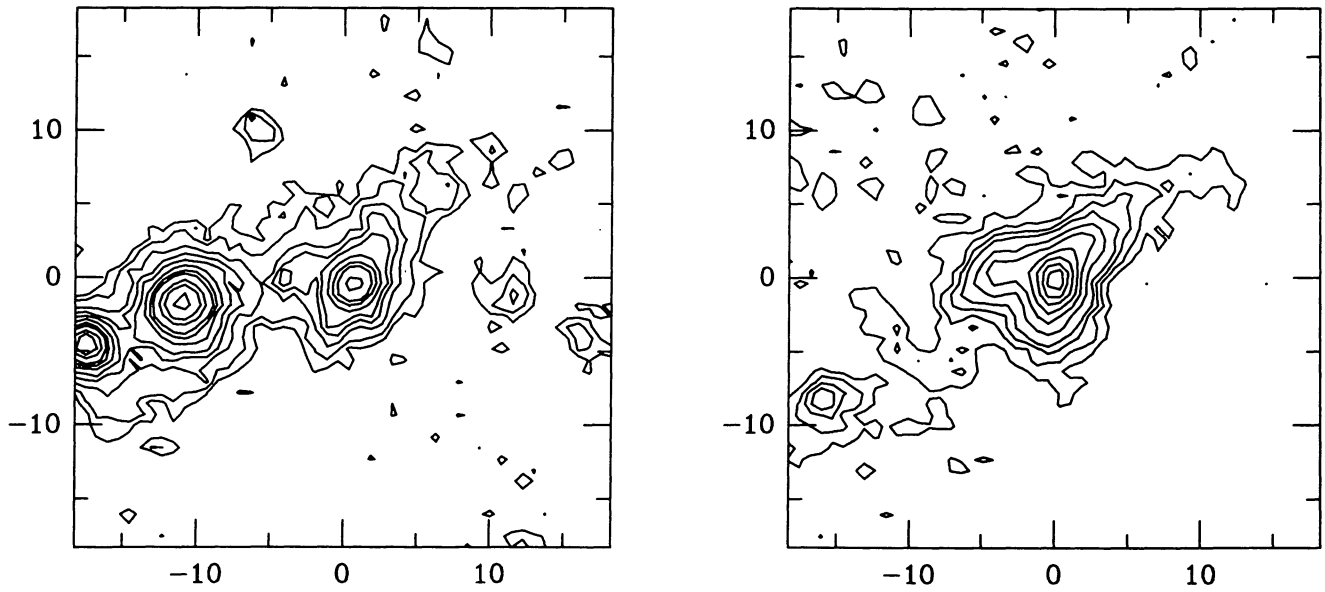

FIG. 39.—3C 265 in [O II] and r_S. The contour levels in the [O II] image in units of 10^{-17} ergs s^{-1} cm^{-2} $arcsec^{-2}$ are 4, 8, 12, 15, 20, 25, 30, 35, 40, 45, 50, 60, 70, 80, 90, and 100.

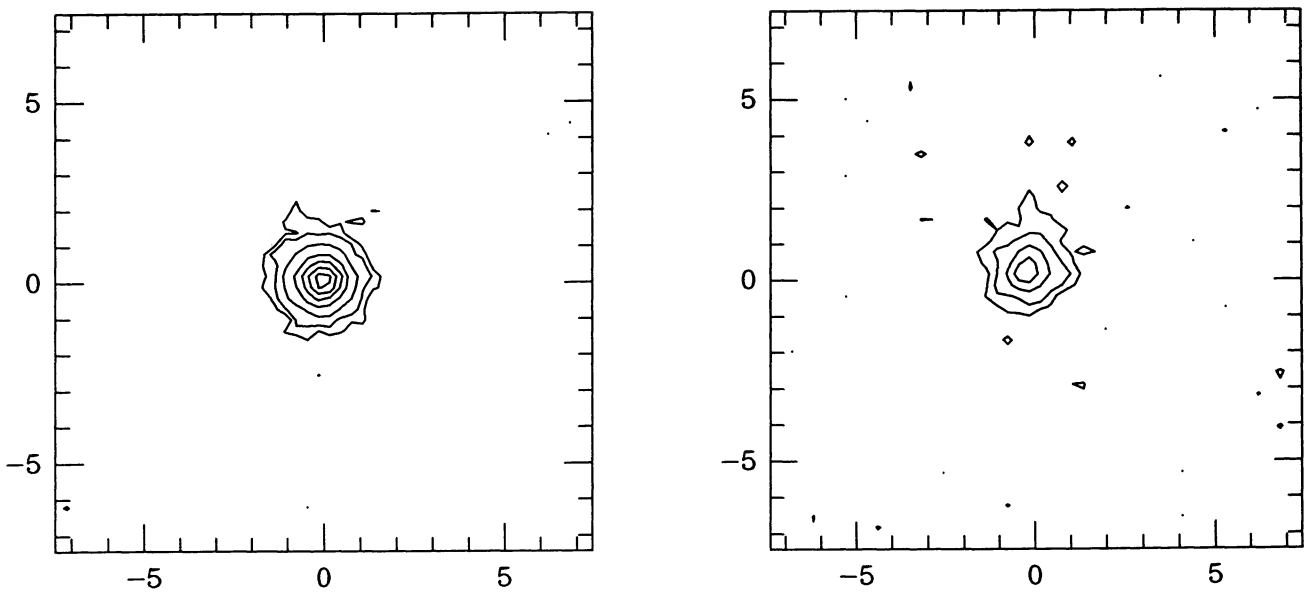

FIG. 40.—3C 226 in [O II] and r_S. We have no flux calibration for this object.

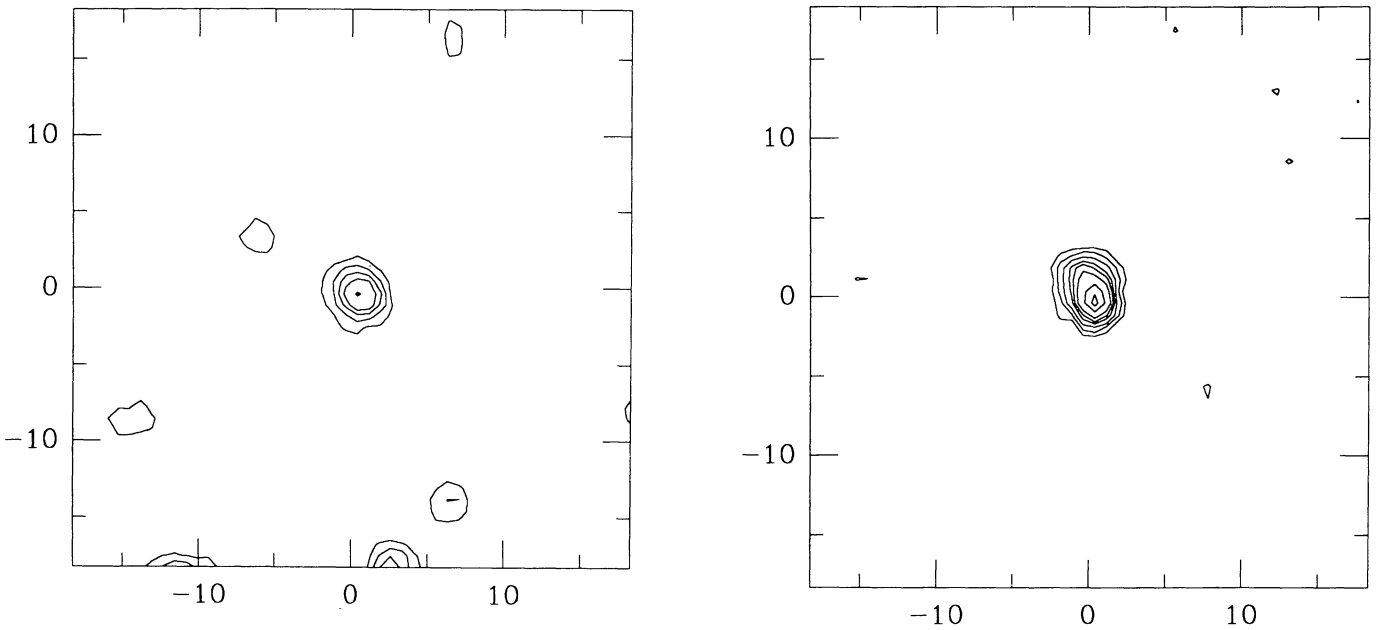

FIG. 41.—3C 263.1 in [O II] and r_S. The contour levels in the [O II] image in units of 10^{-17} ergs s^{-1} cm^{-2} $arcsec^{-2}$ are 3, 5, 8, 12, 15, 20, 30, and 40.

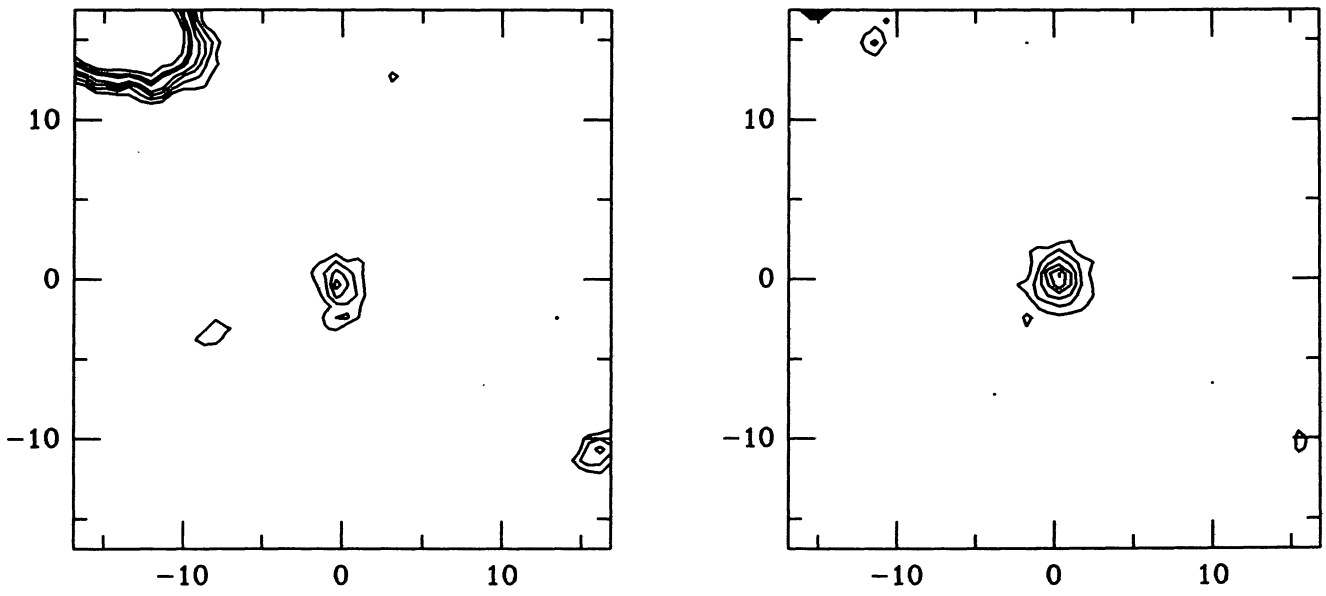

FIG. 42.—3C 54 in [O II] and r_S. The contour levels in the [O II] image in 10^{-17} ergs s^{-1} cm^{-2} arcsec^{-2} are 1.7, 2.6, 3.5, 4.4, 5.2, 6, 7, 7.8, and 8.7.

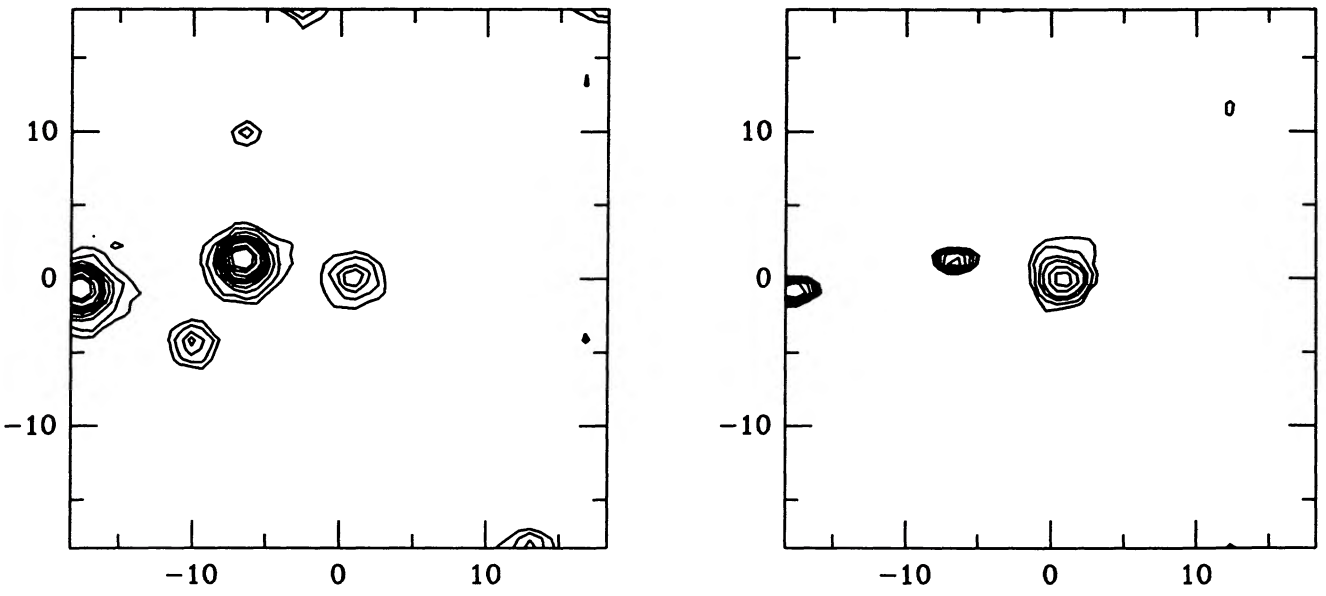

FIG. 43.—3C 22 in [O II] (*top*) and r_S (*bottom*). The contour levels in the [O II] image in units of 10^{-17} ergs s^{-1} cm^{-2} arcsec^{-2} are 4, 6, 10, 14, 21, and 30.

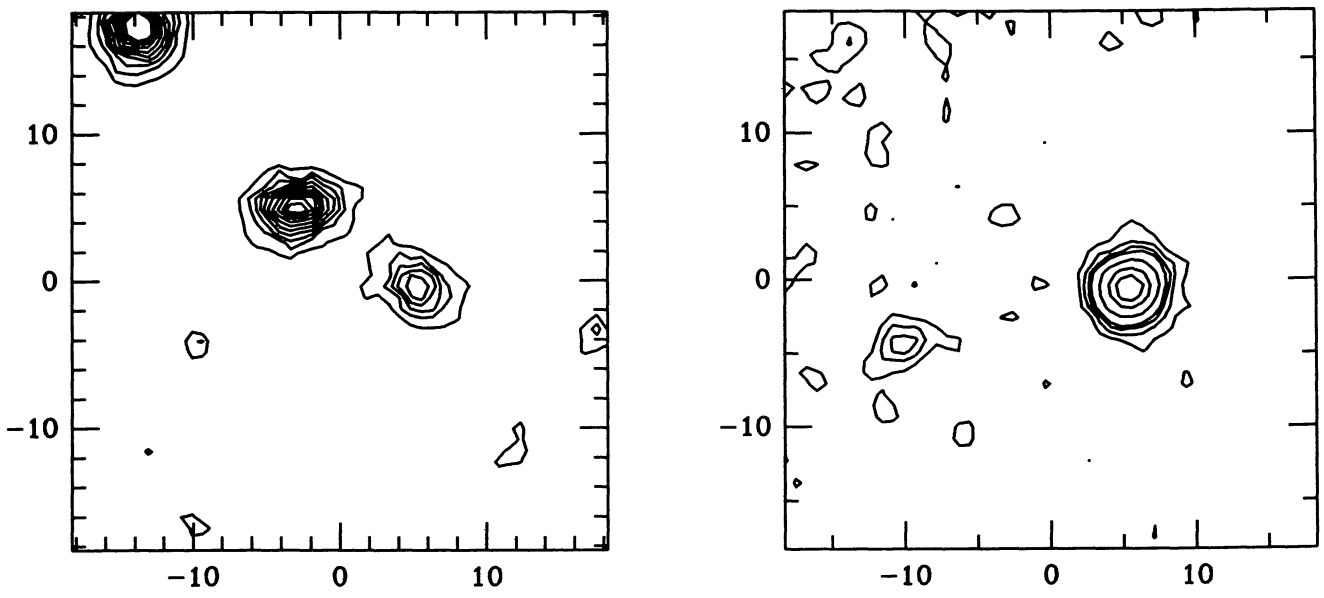

FIG. 44.—3C 184 in [O II] and r_S. The [O II] image shows no extended emission and is uncalibrated.

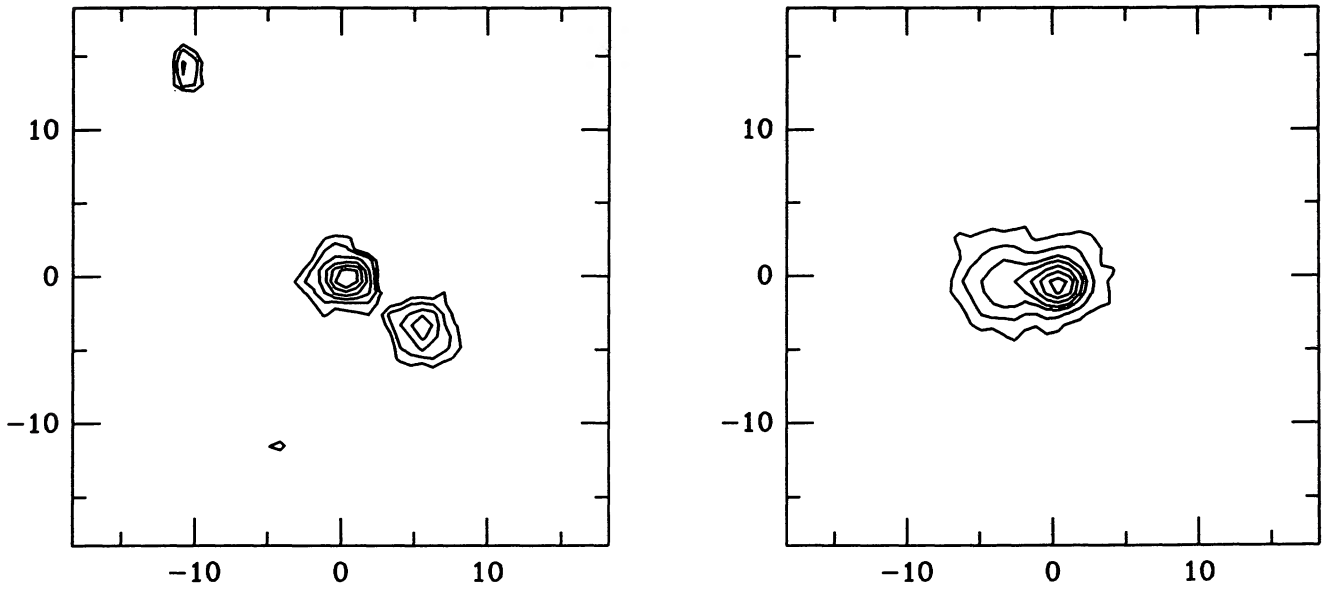

FIG. 45.—3C 280 in [O II] and r_S. The contour levels in the [O II] image in units of 10^{-17} ergs s^{-1} cm^{-2} $arcsec^{-2}$ are 5, 10, 16, 20, 25, 30, and 35.

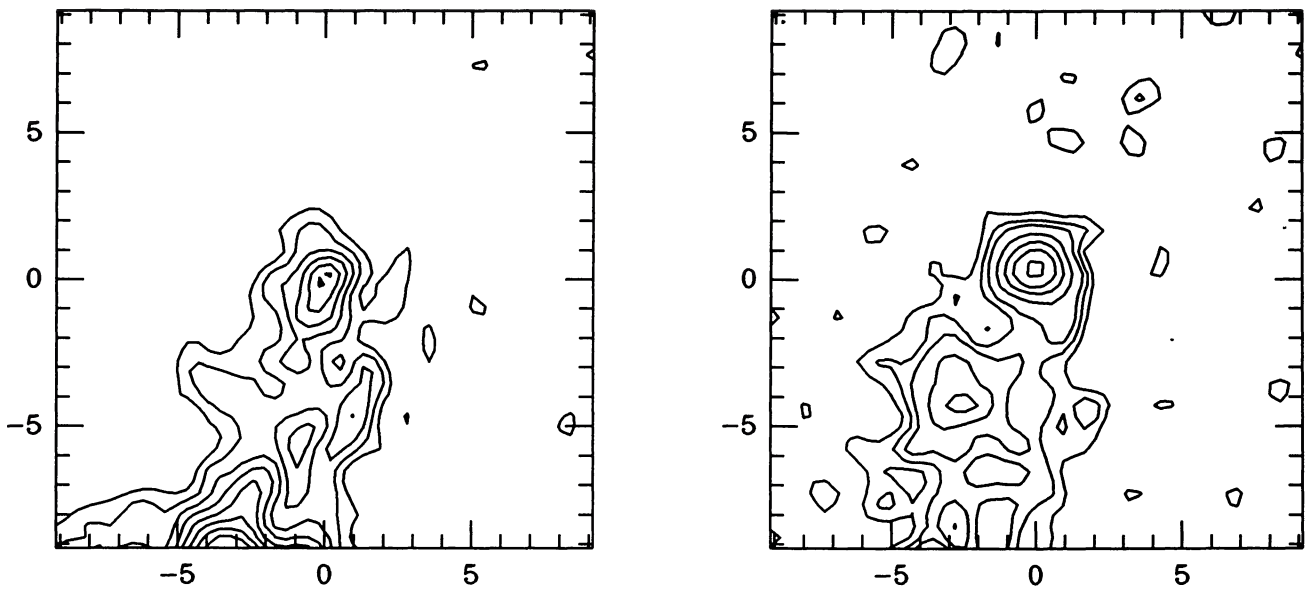

FIG. 46.—3C 356 in [O II] and r_S. The contour levels in the [O II] image in units of 10^{-17} ergs s^{-1} cm^{-2} arcsec^{-2} are 1, 2, 3, 5, 7, 9, and 11.

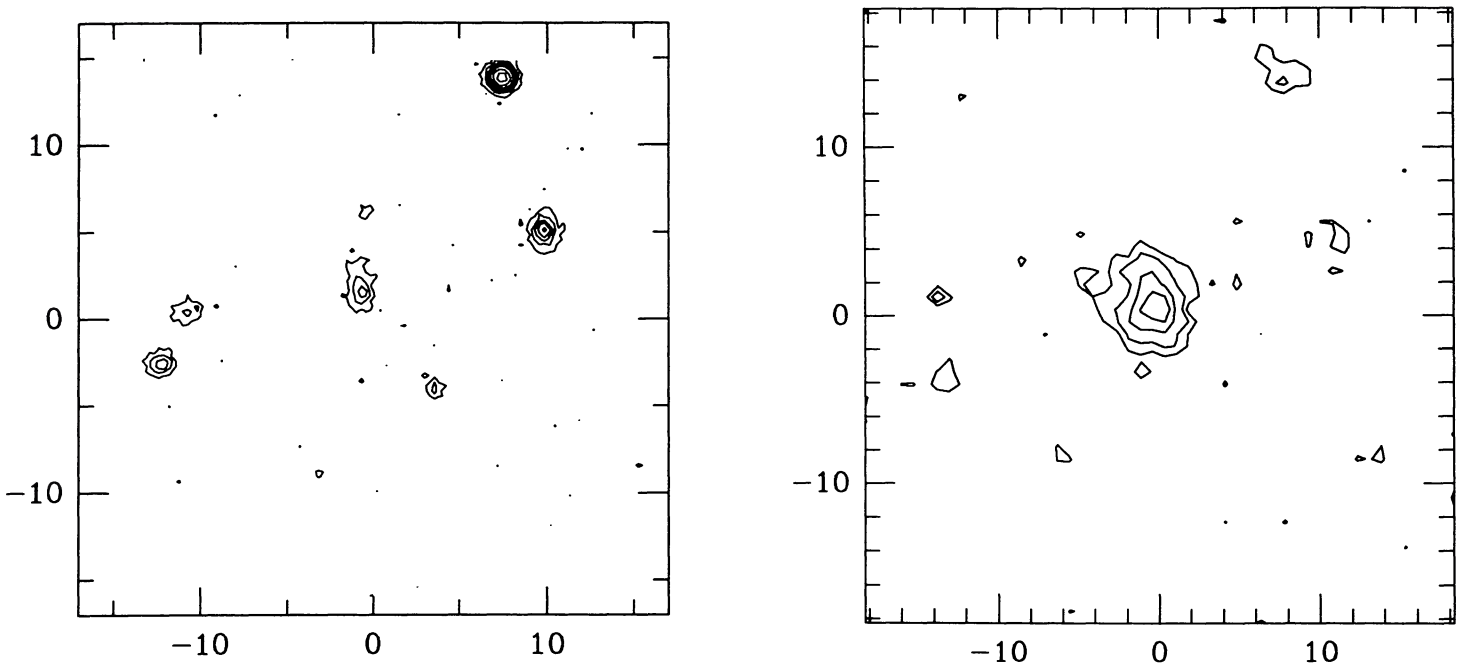

FIG. 47.—3C 124 in [O II] and R. The contour levels in the [O II] image in 10^{-17} ergs s^{-1} cm^{-2} arcsec^{-2} are 1, 1.75, 2.5, 3.75, 5.0, 6.25, 7.5, 8.75, 10, 11.25, 12.15, 13.75, 15.0, 17.5, 20.0, 22.5, 25.0, 27.5, 30.0, 32.5, and 35.0. The R image in the right-hand panel was taken by S. Djorgovski and P. McCarthy with the KPNO 4 m PF-CCD.

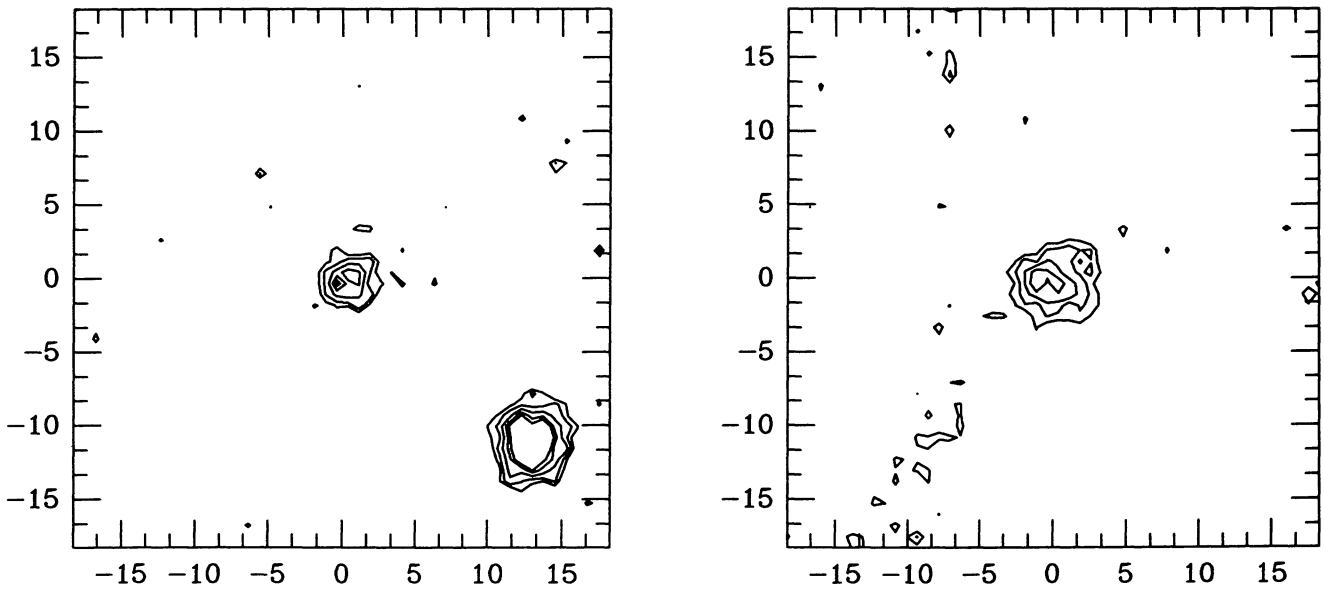

FIG. 48.—3C 252 in [O II] and r_S. The contour levels in the [O II] image in units of 10^{-17} ergs s^{-1} cm^{-2} arcsec^{-2} are 5, 7, 9, 10, and 14.

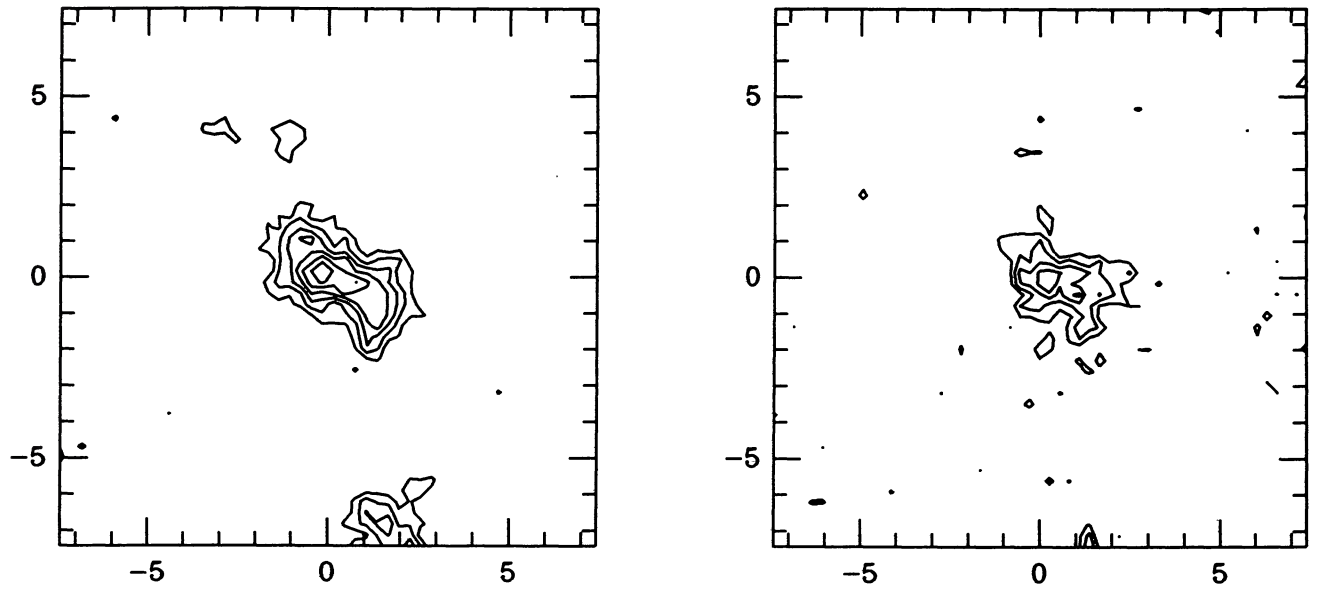

FIG. 49.—3C 267 in [O II] and R. The contour levels in the [O II] image in units of 10^{-17} ergs s^{-1} cm^{-2} arcsec^{-2} are 0.8, 1.2, 1.7, 2.1, 3.0, and 4.4.

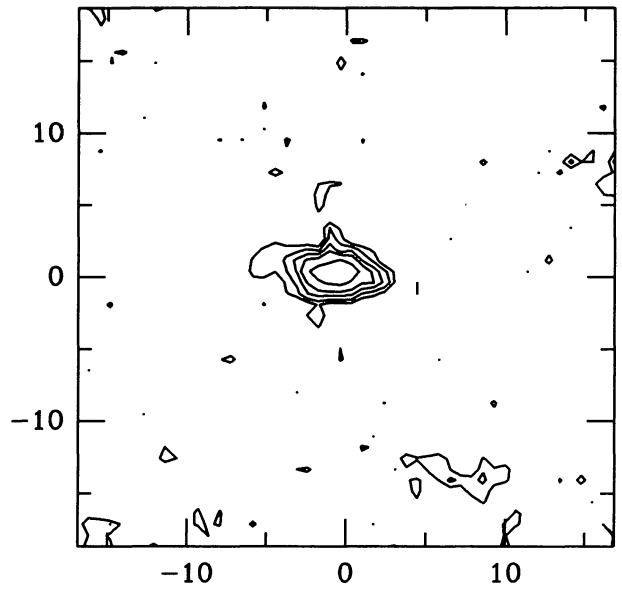

FIG. 50.—3C 324 in [O II]. The contour levels in the [O II] image in units of 10^{-17} ergs s^{-1} cm^{-2} $arcsec^{-2}$ are 6.2, 10, 15, 21, 42, 50, and 60.

in the light of [O III]. The continuum images reveal a cluster with a close projected companion galaxy to the east. The [O III] image shows extensive regions of emission lying in two directions. The inner and highest surface brightness emission is elongated in position angle 140°. This emission extends nearly 20″. A fainter filament of [O III] emission stretches ~25″ to the north and curves around the outer boundary of the northern radio lobe. This is one of the largest high-ionization emission-line regions among the low-redshift 3CR galaxies. The radio source is a 69″ double (Riley & Pooley 1975; J. Stocke 1990, private communication).

3C 357 (z = 0.1664; Fig. 6).—Our Hα image shows two small regions of extended emission lying 2″–3″ from the nucleus along the minor axis of the galaxy. The radio source is an 80″ double, oriented nearly east-west (Riley & Pooley 1975).

3C 33.1 (z = 0.18; Fig. 7).—This galaxy lies in a region of high foreground stellar density. A finding chart is given in Riley, Longair, & Gunn (1980). The continuum plate in Riley et al. shows what appears to be a close companion galaxy 4″ to the southwest, but in our CCD image it appears to be stellar. The Hα image shows emission extended over 10″ in the position angle of the radio source. The emission-line morphology is highly linear and has a "core-jet" type of morphology that is aligned with the radio source axis. An unpublished VLA map made available to us by L. Rudnick shows the source to be a 216″ double. A low-resolution Cambridge map is given by Jenkins, Pooley, & Riley (1977).

3C 28 (z = 0.19; Fig. 8).—This giant elliptical galaxy is the dominant member of the X-ray cluster Abell 115. An *Einstein* image of the cluster is given in Feretti et al. (1984). The Hα image shows a small curved filament extending to the southwest. This filament lies in a region of low surface brightness in the X-ray image. The radio source is a diffuse FR I source (Feretti et al. 1984) that is rather typical of the cooling-flow cluster sources described by Baum & Heckman (1987).

3C 180 (z = 0.22; Fig. 9).—This gE galaxy lies in a cluster. The [O II] image shows two regions of extended emission along the minor axis of the galaxy. The apparent lack of emission at the core of the galaxy is a result of imperfect continuum subtraction. Long-slit spectra show weak emission at the nucleus.

3C 284 (z = 0.24; Fig. 10).—This object lies in a moderately rich cluster. The continuum image is unremarkable. The [O III] image shows a small region of extended high surface brightness emission centered on the nucleus, similar to the circumnuclear emission regions described by Baum et al. (1988). The [O III] image, however, also shows three regions of de-

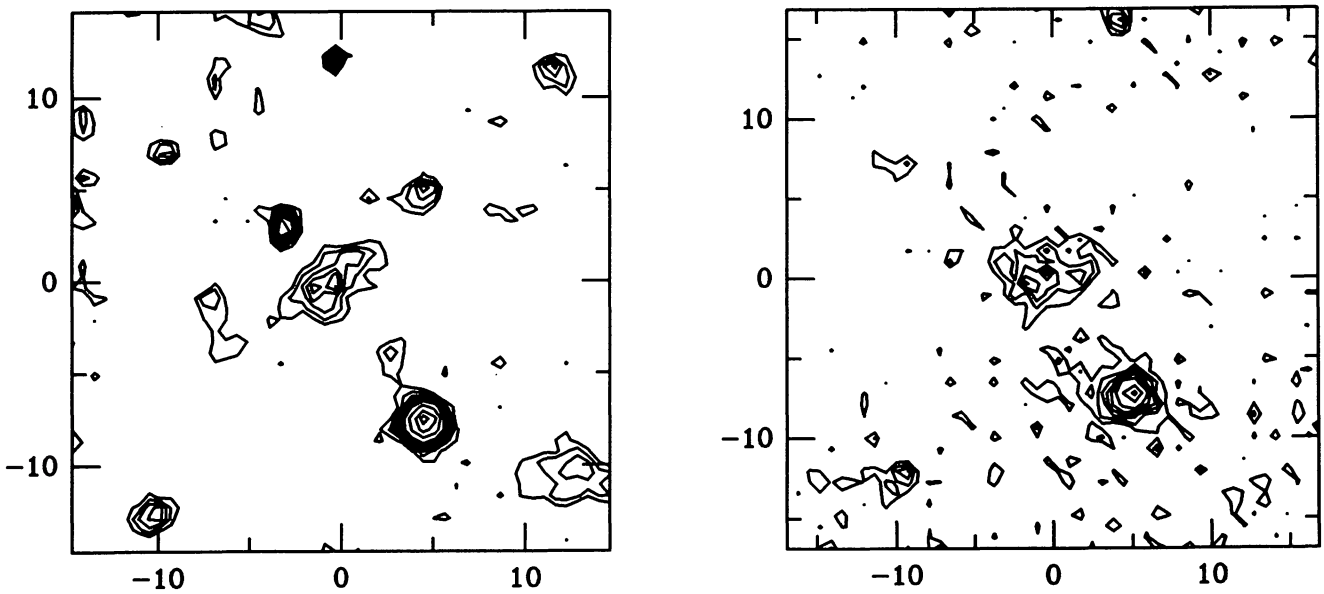

FIG. 51.—3C 437 in [O II] and $B + V$. We have no flux calibration for this object.

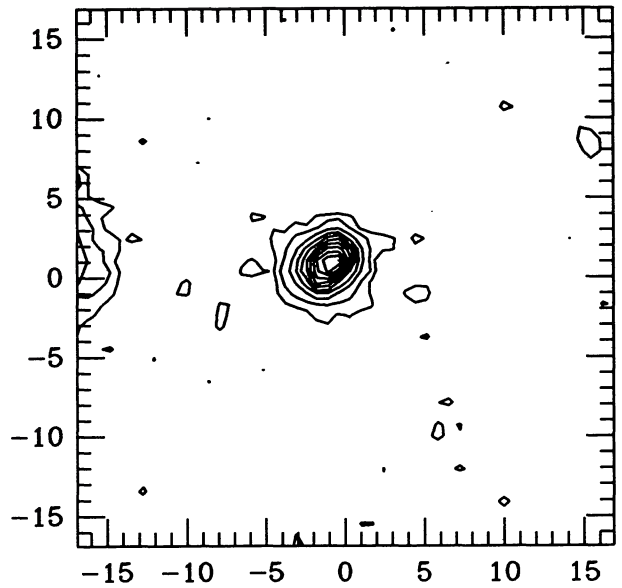

FIG. 52.—3C 256 in Lyα and B. The contours of the Lyα image in units of 10^{-17} ergs s^{-1} cm^{-2} arcsec^{-2} are 3, 6, 12, 18, 24, 30, 36, 42, 48, and 54.

tached emission that lie ~40″ from the nucleus. These detached emission regions lie within 15° of the radio source axis. The source is a large 176″ double in position angle 101° (Riley & Pooley 1975; Leahy & Williams 1984).

3C 79 (z = 0.26; Fig. 11).—This galaxy has been classified as an N type by Kristian, Sandage, & Katem (1974). Our images were taken in rather poor seeing, but reveal a large region of extended Hα emission in a curving filament that extended 12″ to the northwest. There is also diffuse emission surrounding the nucleus. The radio source is a 86″ double, oriented east-west (Riley & Pooley 1975; Leahy & Williams 1984).

3C 379.1 (z = 0.26; Fig. 12).—The continuum image is quite round and unremarkable. The [O III] image shows extended emission on either side of the nucleus in position angle 0°. The total extent of the [O III] emission is 9″. Changes in the image quality (seeing and focus) between the on- and off-band images resulted in poorer continuum subtraction than usual. The radio source is oriented in position angle 161°.

3C 303.1 (z = 0.27; Fig. 13).—The radio source is a 1.″8 double in position angle 90°. The broadband image shows the galaxy to be quite strongly nucleated. The [O III] image shows circumnuclear emission to a radial distance of ~3″.

3C 460 (z = 0.27; Fig. 14).—This object, like 3C 299, is one of the few low-redshift galaxies that show many of the properties of the $z > 1$ sources. The continuum image is elongated and is aligned with the radio source axis. A higher spatial resolution continuum image shows a distinct feature 3″ to the southwest of the nucleus. The [O III] image shows extended emission in the same direction as the continuum emission, but extended over a total of roughly 12″. The radio source is a highly asymmetric 5.″8 double that is oriented in position angle 36° (van Breugel & McCarthy 1995). The [O III] emission extends beyond the southern radio hot spot.

3C 300 (z = 0.27; Fig. 15).—This object lies in a cluster of galaxies. The [O III] image shows regions of very high surface brightness emission, peaking off the nucleus at a level of 3×10^{-15} ergs s^{-1} cm^{-2} arcsec^{-2}. The [O III] image has an S-shaped morphology with the southeast arm of the S pointing directly toward the southeast radio lobe, and the outermost isophotes of the northwest arm pointing toward the northwest lobe. The radio source is a 96″ double in position angle 130° (Riley & Pooley 1975; Leahy & Williams 1984; J. Stocke 1987, private communication).

3C 153 (z = 0.28; Fig. 16).—This galaxy is rather small and unremarkable in the continuum, but imaging is somewhat hampered by a bright star 9″ to the west. The [O II] image shows small extensions to the northeast and southwest. The quality of the continuum subtraction in the emission-line im-

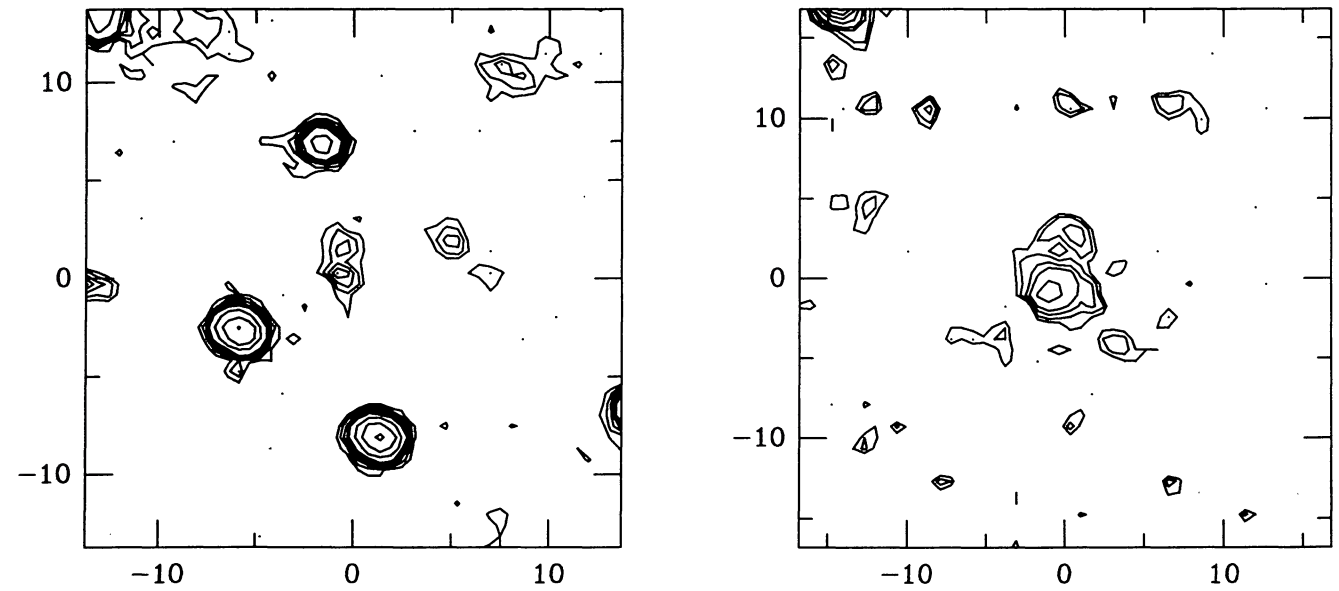

FIG. 53.—3C 454.1 in Lyα and B. The contour levels in the Lyα image in units of 10^{-17} ergs s^{-1} cm^{-2} arcsec^{-2} are 2, 2.4, 3, 3.4, 4.4, 5.5, 6.5, 7.5, and 10.

age is poor, since the KPNO 2 m telescope, with which this image was taken, changed focus between the on- and off-band images.

3C 458 ($z = 0.29$; Fig. 17). This object is one of the most visually striking objects in the sample. The continuum image shows the galaxy to be small and highly nucleated. A number of fainter cluster members can be seen close to the host galaxy. The identification of 3C 458 given in Kristian et al. (1974) appears to be a plate flaw, since it is not seen in our deep CCD images. The object marked by Wyndham (1966) appears to be the correct identification. For this object we obtained V as well as [O II] λ3727 and [O III] λ5007 images (Figs. 54*a,* 54*b,* and 54*c*). Both images show an extensive network of filaments extending over more than 35″ (300 kpc, $H_0 = 50$ km s^{-1} Mpc^{-1}), making this one of the largest nebulae in our sample. The inner region of the nebula has a core-jet type of morphology. There are significant differences between the morphologies revealed in the [O II] and [O III] images. The [O III] λ5007 image (Fig. 54*b*) shows high surface brightness emission in the central ~10″, while the [O II] λ3727 emission (Fig. 54*c*) is brighter at large distances. The diffuse patch of [O II] emission lying 15″ south and 15″ west of the nucleus has been detected spectroscopically and has a lower ionization state than the gas closer to the nucleus. The considerable excitation differences within this object should prove useful in quantitative tests of central ionization models.

The radio source is a very large (191″ = 1.2 Mpc) double, one of the largest radio galaxies in the 3CR catalog, with a weak core (J. Stocke 1990, private communication). The inner filaments are skewed from the radio source axis by 20°. The radio source has one of the largest flux density asymmetries in the sample, 9:1, and is only moderately asymmetric in its lobe arm ratio, 1.2:1. The closer of the two lobes lies to the southwest, the direction of the highest surface brightness [O II] and [O III] emission. The brighter of the two lobes lies to the northeast.

3C 299 ($z = 0.367$; Fig. 18).—This object has very high surface brightness both in the continuum and in [O III]. The continuum is highly elongated and is aligned with the radio source axis. The [O III] image shows strong emission extended over ~10″. The radio source is quite asymmetric (Pearson, Perley, & Readhead 1985; van Breugel & McCarthy 1995). The region of highest surface brightness [O III] emission is offset from the nucleus toward the northeast, the direction of the closer lobe. In many respects this object resembles the high-redshift ($z > 1$) radio galaxies, and yet it is at a rather low redshift.

3C 268.3 ($z = 0.37$; Fig. 19).—This object is small and unremarkable in the continuum. The [O III] image shows extended emission on a scale of ~4″ with fairly high surface brightness. The radio source is a small 1.″3 double, oriented in position angle 161°. This object is one of several sources that show extended emission along the radio source axis, but on scales larger than the radio source.

3C 244.1 ($z = 0.428$; Fig. 20).—This galaxy lies in a cluster. The continuum appears rather distorted, but this may be due in part to close projected cluster members. The [O III] image shows a high surface brightness fan of emission extending ~7″ to the northwest. The [O III] morphology is quite similar to that of the cluster galaxy 3C 330. The radio source is a 52″ double, oriented in position angle 168°, similar to the [O III] position angle. The radio source is quite symmetric in both its lobe flux densities and its arm-length ratios (Leahy & Williams 1984).

3C 306.1 ($z = 0.44$; Fig. 21).—This galaxy has a disturbed appearance in the continuum, with a nearby companion and low surface brightness emission that resembles tidal tails of the sort seen in a number of nearby powerful radio galaxies (e.g., Heckman et al. 1986). The [O II] image shows a small extension to the southwest with a morphology of the core-jet type. A recent VLA observation shows the source to be a symmetric double.

3C 341 ($z = 0.45$; Fig. 22).—This galaxy is unremarkable in the continuum, and our [O II] images are of rather poor quality. Nonetheless, we can say that the [O II] emission is slightly extended to the north. The radio source is a 71″ double, oriented north-south.

3C 313 ($z = 0.46$; Fig. 23).—This galaxy is unremarkable both in the continuum and in [O III]. The [O II] emission is slightly extended on a scale of 4″. The radio source is a large double, oriented in position angle 59° (Baum et al. 1988).

3C 435A ($z = 0.47$; Figs. 24 and 55). This is one of the most unusual objects in the sample. The Cambridge 1 mile (1.6 km) telescope map given by Mackay (1969) showed the source to be a large, highly asymmetric double. Modern VLA observations by McCarthy, van Breugel, & Spinrad (1989) show that 3C 435 is actually composed of two doubles with roughly equal flux densities. The identification proposed by Smith & Spinrad (1980) is the correct identification for the smaller of the two sources, which we have designated 3C 435A. This source is a 7″ double. The continuum image of this galaxy shows it to have a close companion galaxy 5″ to the northeast. This object lies roughly 2″ east, in projection, of the northern lobe. The [O II] image shows emission extended with a scale of ~25″ in the direction of the radio lobes. The [O II] emission, however, extends more than 5″ beyond the radio hot spots. An overlay of the [O II] image and the radio map is given by van Breugel & McCarthy (1989). The region of highest surface brightness [O II] emission is nearly coincident with the northern radio lobe, and is slightly offset from the continuum peak of the companion galaxy.

3C 172 ($z = 0.52$; Fig. 25).—The northernmost of the three objects near the center is coincident with a radio core (Laing, Owen, & Puschell 1984). The [O II] emission is moderately strong and extends 7″ to the southwest. The quality of the [O II] image is not particularly good, primarily because of poor continuum subtraction. The radio source is a 103″ double, oriented 37° east of north, nearly parallel to the continuum and the [O II] emission. The radio source is only slightly asymmetric with the close lobe lying to the southwest, the side of the extended [O II] emission.

3C 330 ($z = 0.55$; Fig. 26).—This object lies in a cluster and has a close companion to the north. The [O III] emission is quite strong and is extended over roughly 5″ to the northeast. The radio source is a large (62″) double that is oriented in position angle 62° (Jenkins et al. 1977; Schilizzi, Kapahi, & Neff 1982; McCarthy et al. 1991).

3C 228 ($z = 0.55$; Fig. 27).—Our images were obtained in rather poor conditions. Nonetheless, we are able to determine that the [O II] image shows no extended emission on a scale larger than 2.″5. The radio source is a large double (Jenkins et al. 1977).

3C 169.1 ($z = 0.63$; Fig. 28).—This galaxy has a close companion that appears to be interacting with it. The projected distance to the companion is 4″, or 40 kpc for $H_0 = 50$, $q_0 = 0.2$. The [O II] image shows a curved filament that connects to the companion. The highest surface brightness [O II] emission is offset from the continuum of the companion, as is often the case (see 3C 172, 3C 435A, 3C 321). The radio source is a 38° double that is oriented 137° east of north.

3C 337 ($z = 0.64$; Fig. 29).—This cluster galaxy has an unremarkable continuum morphology, but has quite extended [O II] emission. The [O II] emission has a rather low surface brightness, typically 10^{-17} ergs s^{-1} cm^{-2} arcsec^{-2}. The emission-line region lies in the backflow of the southwestern radio lobe. The source is a 43″ double with a large asymmetry in both structure and lobe flux densities. The closer of the two lobes is to the southwest. Detailed VLA observations of this source are given by Pedelty et al. (1989b).

3C 44 ($z = 0.66$; Fig. 30).—This galaxy lies in a large cluster that can be seen in the image taken by Spinrad (1986). The central galaxy is unremarkable in its structure; the extension to the northwest is a close (in projection) companion galaxy. The [O II] emission is extended in a curved filament to the south. The radio source is a large (65″) double, oriented north-south. The [O II] image revealed two cluster members with strong emission. These have both been confirmed spectroscopically.

3C 34 ($z = 0.69$; Fig. 31).—This galaxy lies in a rich, compact cluster. The continuum image of the galaxy itself is confused by close projected companions. The [O II] image shows an extensive region of high surface brightness emission. The emission is distributed east-west, as is the radio source, and is quite symmetric in its surface brightness distribution. The source is a 46″ double (Jenkins et al. 1977).

3C 441 ($z = 0.71$; Fig. 32).—This source is quite remarkable in its optical continuum properties. The host galaxy is compact, although the presence of a number of close objects makes it difficult to determine the continuum morphology in detail. The broadband image shows a large diffuse object located 12″ north and 8″ west of the core galaxy. This low surface brightness object is extended over more than 12″ (100 kpc for $H_0 = 50$, $q_0 = 0.2$) and has a luminosity roughly equal to that of the core galaxy. This object lies within the northern radio lobe of 3C 441. The [O II] image shows a diffuse patch of emission along the radio source axis just beyond the peak of the continuum object described above and near the boundary of the northern radio lobe. Long-slit spectroscopy resulted in the detection of [O II] emission beyond the region shown in the image and 3″ beyond the radio hot spot. The source is a fairly large (33″) asymmetric double. The closer of the two hot spots lies to the northwest, the direction of the extended [O II] and continuum emission.

3C 247 ($z = 0.749$; Fig. 33).—Imaging of this galaxy is made difficult by the presence of a bright star only 4″ to the northeast. Our [O II] image reveals an elongated structure oriented to the northeast, the direction of the radio source. The [O II] morphology of this object is quite similar to that of 3C 352. The continuum image was taken with the KPNO 4 m telescope by Djorgovski and Spinrad. While this image is contaminated by the star, the galaxy appears to be elongated in the same direction as the [O II] emission. The radio source is a moderately asymmetric 12.″5 double (Jenkins et al. 1977).

3C 343.1 ($z = 0.75$; Fig. 34).—This is an interesting object from the point of view that it is a very small (0.″2) VLBI radio source (van Breugel & McCarthy 1995). The continuum is moderately elongated in a position angle that is 45° from the radio source axis. The [O II] image shows extended emission over 5″ in the direction of the radio source. This the most extreme sample of an object whose emission-line extent is larger than the radio source, yet the extended emission is in the direction of the source axis.

3C 277.2 ($z = 0.77$; Figs. 35 and 56).—This object is one of the most extended galaxies, both in the continuum and in the emission lines. The continuum image shows a number of nearby galaxies that are likely cluster members (a concordant redshift has been obtained for one of them). The *R* image also shows continuum in a diffuse patch extending over more than 30″. The [O II] image shows emission that is also quite extended, with morphology that is similar to that of the continuum. The linear extent of the diffuse emission and continuum is 360 kpc for $H_0 = 50$, $q_0 = 0.2$. The *R* filter contains a contribution from [O II] λ3727 emission, but the diffuse continuum has been confirmed spectroscopically. The radio source is a highly asymmetric 54″ double with the closer of the two lobes located to the southwest (Pedelty et al. 1989a). The extended emission lies along the boundary of the close radio lobe, which is strongly depolarized. This object best shows the radio-optical correlations that are found for nearly all of the galaxies with $z > 0.6$.

3C 340 ($z = 0.77$; Fig. 36).—The continuum is fairly elongated and is aligned with the radio source axis. The identification given in Laing et al. (1983) is incorrect and is superseded by the identification given here. The [O II] emission extends over 3″ along the radio axis and has the core-jet type of morphology. The radio source is a 45″ double, oriented in position angle 88° (Riley & Pooley 1975; Jenkins et al. 1977).

3C 41 ($z = 0.79$; Fig. 37).—This object is unremarkable both in the continuum and in the emission lines. The continuum is marginally resolved in our mediocre seeing image, and the [O II] emission is completely unresolved. The radio source is a 23″ double.

3C 352 ($z = 0.81$; Fig. 38).—A foreground star only 5″ away makes continuum imaging of this object rather difficult. Our r_S image does show the continuum to be extended with a position angle of 135″. Higher quality continuum images are given by Lilly, Longair, & McLean (1983) and Rigler et al. (1992). Our [O II] images show extended emission on a scale of 8″ in nearly the same position angle as the continuum. The radio source is a 10.″2 double in position angle 162″ (Jenkins et al. 1977; Schilizzi et al. 1982).

3C 265 ($z = 0.81$; Figs. 39 and 57).—This object is one of the most spectacular objects in the sample. The continuum image shows extended structure over more than 10″ and a very bright nucleus. The bright continuum objects to the east are foreground (H. Spinrad 1986, private communication). The [O II] image shows emission over more than 30″, corresponding to more than 320 kpc for $H_0 = 50$, $q_0 = 0.2$. The [O II] emission lies along the axis of the radio source, which is a 78″ double with a double hot spot (Jenkins et al. 1977). This object is particularly unusual because it shows strong extended Ne V λλ3426, 3346 emission (McCarthy & Baum 1995). High spatial resolution images of 3C 265 are given by Rigler et al.

(1992). Jannuzi & Elston (1991) report high linear polarization in the nucleus.

3C 226 ($z = 0.82$; Fig. 40).—Our images were obtained in rather poor conditions. Nonetheless, we are able to determine that the [O II] image shows no extended emission on a scale larger than 2".5.

3C 263.1 ($z = 0.82$; Fig. 41).—This galaxy is small but is still noticeably elongated. The [O II] emission is quite strong and extends in the same direction as the continuum and has the core-jet type of morphology. The radio source is a small (5".8) double (Jenkins et al. 1977).

3C 54 ($z = 0.83$; Fig. 42).—This object is quite compact both in the continuum and in [O II]. The continuum image is moderately elongated north-south as is the [O II] image, although the latter appears to be rounder. The radio source is a large 54" double, oriented 25° east of north.

3C 22 ($z = 0.99$; Fig. 43).—This galaxy is unresolved in the continuum and in [O II]. The slight [O II] extension to the north at a surface brightness level of $\sim 4 \times 10^{-17}$ ergs s^{-1} cm^{-2} arcsec^{-2} is probably an artifact. The [O II] emission is strong, and the rest-frame equivalent width is 110 Å (Perryman et al. 1984). Incomplete continuum subtraction has left residuals associated with the brighter stars in the frame. The radio source is a 25" double in position angle 105° (Jenkins et al. 1977; Schilizzi et al. 1982).

3C 184 ($z = 0.99$; Fig. 44).—This object is slightly elongated in the continuum, although this is best seen in the unpublished KPNO 4 m *R* image by Djorgovski, Spinrad, & Dickinson (1991). The [O II] image shows no extended emission. The [O II] image does, however, show emission from a companion galaxy 10" east and 4" south of 3C 184. The redshift of this galaxy ($z = 0.99$) has been confirmed spectroscopically. The radio source is a 4".4 double, oriented nearly east-west (Jenkins et al. 1977).

3C 280 ($z = 0.99$; Fig. 45).—This galaxy is rather small and round in the continuum but shows a region of high surface brightness [O II] emission 5" to the east. The extended [O II] emission is spatially coincident with the closer of the two radio hot spots (Pooley & Henbest 1974; Schilizzi et al. 1982). A high spatial resolution [O II] image taken by Rigler et al. (1992) shows that the [O II] emission is edge-brightened and lies along the boundaries of the radio lobe.

3C 356 ($z = 1.08$; Figs. 46 and 58).—A bright foreground star makes continuum imaging of this object quite difficult. High-resolution images of this object are given by Le Fèvre, Hammer, & Jones (1988a). This image shows that the host galaxy is extremely nucleated. A large (4") region of diffuse continuum lies 5" to the southeast of the nucleus. This region has a rather flat surface brightness distribution and an integrated flux equivalent to that of the nucleus. Our [O II] image shows that this region has strong [O II] emission extended over similar scales. The spatially integrated [O II] flux is also approximately equal to the core [O II] flux. The radio source is a large (72") asymmetric double, oriented in position angle 162° (Pedelty et al. 1989a). There is some uncertainty regarding which of the two continuum objects contains the nucleus of the radio source. Two core positions have been reported (Laing et al. 1984; Pedelty et al. 1989a; Fernini et al. 1993) that correspond to the two continuum objects. We identify the northern object as the nucleus on the basis of its compact structure and high-ionization spectrum. The diffuse object to the southeast has spatially resolved emission lines with a low excitation level. Eales & Rawlings (1990) identify the other object as the nucleus. At this point it remains unclear which of the two objects is the true nucleus.

3C 124 ($z = 1.08$; Fig. 47).—This object is extremely elongated and clumpy in its continuum structure. The continuum image presented here was taken with the KPNO 4 m telescope by Djorgovski. The [O II] image, taken with the Lick 3 m telescope, shows extended emission with a morphology that is similar to that of the continuum. The surface brightness of the [O II] emission is quite high. The radio source is a small (1".3) double, oriented north-south (van Breugel & McCarthy 1995). This is one of the best cases of a source with [O II] emission along the radio source axis, but extended beyond the radio hot spots.

3C 252 ($z = 1.10$; Fig. 48).—Our images of this galaxy were taken in poor (2".5 FWHM) seeing. The [O II] emission appears to be extended, but we do not resolve any structure. The radio source is a 60" double.

3C 267 ($z = 1.14$; Fig. 49).—This galaxy has an unusual "butterfly-like" morphology both in the continuum and in [O II]. The radio source is a 38" double with a weak core (Pedelty et al. 1989a). The broadband image shows a number of faint galaxies, lying to the southwest of 3C 267. Three of these galaxies, including the one closest to 3C 267, show excess emission in the [O II] image, implying that they are members of a cluster containing 3C 267. If this is the case (spectroscopic confirmation is required), 3C 267 would rank among the most distant clusters of galaxies known.

3C 324 ($z = 1.2$; Fig. 50).—This object was one of the first extremely elongated high-redshift radio galaxies identified by Spinrad & Djorgovski (1984a). High spatial resolution images are given by Le Fèvre et al. (1987). The [O II] image presented here shows extended emission on a scale of ~ 8" with a morphology that is very similar to that of the continuum. This exposure is quite short (20 minutes), and as a result it does not go very deep. The radio source is a small double, oriented in nearly the same direction as the galaxy (Pedelty et al. 1989a).

3C 437 ($z = 1.48$; Figs. 51 and 59).—This is the most distant object that we have imaged in [O II]. At a redshift of 1.48, [O II] λ3727 is at 9242 Å. The continuum image was taken by Spinrad and Dickinson with the KPNO 4 m telescope. The continuum image is highly elongated and clumpy in appearance. A high-resolution image is given by Le Fèvre & Hammer (1988). The continuum is quite misaligned with the radio source axis (43°), making it the most misaligned 3CR galaxy with $z > 1$. The [O II] image shown here has not had the continuum subtracted; the object to the southwest is a foreground star. The [O II] emission is extended east-west, also at a large angle to the radio source axis. The source is a large (34") double (Strom et al. 1989; van Breugel & McCarthy 1995).

3C 256 ($z = 1.82$; Fig. 52).—This galaxy was one of the first of the high-redshift galaxies found to have strong Lyα emission (Spinrad et al. 1985b). A high spatial resolution continuum image is given in Le Fèvre et al. (1988b). The Lyα image presented here shows high surface brightness emission that appears to be rounder than the continuum image. Both the con-

tinuum and the Lyα emission are aligned with the radio source axis. The radio source is a small 4".2 double (van Breugel & McCarthy 1995).

3C 454.1 (z = 1.84; Fig. 53).—The continuum structure of this object is quite remarkable. The continuum image presented here has been published as a halftone by Djorgovski et al. (1988). The image shows the object to consist of two small condensations separated by 2". A high-resolution image is given by Le Fèvre & Hammer (1988). The continuum morphology corresponds very closely to the radio source structure. The VLA map by Pearson et al. (1985) shows the source to be a 2".5 double, oriented north-south. Astrometric measurements by Djorgovski et al. (1987) show that the two continuum knots correspond to the radio lobes. The high-resolution images of Le Fèvre & Hammer (1988) reveal a fainter knot between the two coincident with the radio lobes. The Lyα image shown here reveals emission on a scale much larger than that of the continuum. Lyα emission can be traced to a diameter of greater than 5". The low surface brightness features 4" to the southeast and southwest appear to be real.

5. STRUCTURE OF THE EMISSION-LINE REGIONS

We have measured the basic structural properties of the nebulae discovered in this program. The largest angular size of each nebula has been determined at a fixed rest-frame surface brightness level of 3×10^{-17} ergs s^{-1} cm^{-2} in Hα + [N II]. We chose this surface brightness level to allow direct comparison with the work of Baum & Heckman (1989a) on low-redshift radio galaxies. Since most of the images were taken in lines other than Hα + [N II], we were required to scale the surface brightness by an amount equal to the intensity ratio of each line imaged relative to Hα + [N II]. The line ratios that we used were [O II] λ3727/(Hα + [N II]) = 1, [O III] $\lambda\lambda$5007, 4959/(Hα + [N II]) =3, and Lyα/(Hα + [N II]) = 2. These were derived from individual one-dimensional spectra as well

TABLE 2

SIZES OF EMISSION-LINE REGIONS

3CR	z	θ(")	D[1](Kpc)	D[2](Kpc)	Reference	3CR	z	θ(")	D[1](Kpc)	D[2](Kpc)	Reference
454.1	1.847	7.0	89	58	1	341.0	0.448	6.5	49	44	1
326.1	1.825	8.3	106	69	4	306.1	0.441	6.8	51	46	1
256.0	1.819	6.4	81	53	1	244.1	0.428	7.8	58	52	1
294.0	1.779	12.0	152	100	5	268.3	0.371	4.5	31	28	1
437.0	1.480	6.8	83	58	1	299.0	0.367	13.0	88	80	1
266.0	1.275	4.0	47	34	1	109.0	0.306	8.6	52	48	2
324.0	1.206	8.0	92	69	1	458.0	0.290	40.0	232	216	1
267.0	1.140	2.7	31	23	1	300.0	0.270	13.0	72	67	1
305.1	1.132	3.7	42	32	1	460.0	0.268	7.0	38	36	1
368.0	1.132	8.0	91	69	1	303.1	0.267	3.2	18	16	1
356.0	1.079	7.6	85	65	1	379.1	0.256	7.0	37	35	1
280.0	0.998	9.0	98	77	1	79.0	0.256	22.0	117	110	1
184.0	0.994	1.5	16	13	1	284.0	0.239	92.0	467	439	1
22.0	0.937	3.0	32	25	1	171.0	0.238	13.0	66	62	2
435.1	0.865	2.5	26	21	6	180.0	0.220	12.0	57	54	1
54.0	0.827	4.0	41	33	1	196.1	0.198	5.6	25	23	2
263.1	0.824	5.6	57	46	1	28.0	0.195	6.0	26	25	1
226.0	0.818	2.0	20	17	1	33.1	0.181	14.0	58	55	1
265.0	0.811	28.0	283	231	1	63.0	0.175	15.6	63	60	2
352.0	0.806	6.0	60	49	1	357.0	0.166	7.1	27	26	1
41.0	0.794	4.0	40	33	1	381.0	0.160	34.0	127	122	1
340.0	0.775	3.8	38	31	1	223.0	0.137	7.2	24	23	2
277.2	0.766	32.0	316	261	1	135.0	0.108	4.0	12	12	2
343.1	0.750	5.6	55	45	1	327.0	0.104	7.6	20	19	1
247.0	0.749	8.7	85	71	1	433.0	0.102	12.0	31	30	1
441.0	0.707	17.0	162	136	1	321.0	0.096	23.5	57.2	55.8	2
34.0	0.689	18.0	170	143	1	285.0	0.079	10.0	20.6	20.2	2
44.0	0.660	8.7	81	68	1	192.0	0.060	24.3	38.7	38.2	2
337.0	0.635	11.5	105	89	1	403.0	0.059	10.2	16.1	15.8	2
169.1	0.633	8.0	73	62	1	382.0	0.058	25.0	38.6	38.1	1
228.0	0.552	2.4	20	18	1	218.0	0.055	5.8	8.6	8.4	2
330.0	0.550	10.0	85	74	1	317.0	0.035	26.0	25.1	24.9	2
172.0	0.519	6.9	57	50	1	98.0	0.031	38.0	32.3	32.1	2
275.0	0.480	6.6	52	46	2	88.0	0.030	9.3	7.8	7.8	2
435.0	0.471	36.0	281	250	1	78.0	0.029	8.6	6.9	6.9	2
295.0	0.461	6.8	53	47	2	264.0	0.021	7.0	4.1	4.1	2
313.0	0.461	2.0	15	14	1	278.0	0.014	8.7	3.6	3.6	2
						272.1	0.003	21.7	2.0	2.0	2

[1] $H_0 = 50$, $q_0 = 0.1$.
[2] $H_0 = 50$, $q_0 = 0.5$.
REFERENCES.—See list following Table 3.

TABLE 3

OPTICAL AND RADIO MORPHOLOGIES

3CR	z	PA r	PA [OII]	PA radio	References r	[OII]	radio
257.0	2.480	126	59	125	8	8	8
454.1	1.847	177	167	167	1,4,15,10	1	23
326.1	1.825	108	108	94	4,11	4	4
256.0	1.819	145	140	134	18	1	21
239.0	1.781	139	...	75	9	...	22
294.0	1.779	...	1	35	...	5	16
322.0	1.676	83	...	...	9,15	...	21
470.0	1.653	128	...	38	10	...	21
241.0	1.617	84	...	80	1,11	1	21
68.2	1.575	169	...	155	10	...	23,24
225.1	1.560	41	...	15	10	...	21
230.0	1.487	...	...	159	9	...	21
437.0	1.480	134	90	160	1,10,16	1,16	21,16
297.0	1.406	178	167	...	9	9	21
238.0	1.405	163	...	163	11	...	21
13.0	1.351	155	...	145	18	...	25
469.1	1.336	131	...	171	9	...	25
36.0	1.301	...	...	20	...	...	25
266.0	1.275	174	174	177	9,12,46	1,9,12	21
324.0	1.206	95	90	71	12,19	9,1,12	25
194.0	1.185	178	...	151	10,15	...	16
65.0	1.176	93	N	98	10,12	12	...
300.1	1.170	...	...	0	15	...	21
210.0	1.169	167	...	167	9,15	...	16
267.0	1.140	63	46	79	1,9,12	1,12	25
305.1	1.132	180	180	11	1	1	23,24
368.0	1.132	13	19	18	11,12,17,13	11,12,17	28,17
252.0	1.1035	114	115	107	1,9	1	29
124.0	1.083	6	8		1	1	21
356.0	1.079	150	161	162	1,12,11	1,12,11	25
173.0	1.035	...	...	0	15	...	30
208.1	1.020	R	...	103	14	...	21
280.0	0.9975	94	90	91	1,12,47	1,12,47	21,37
184.0	0.994	83	N	106	1,7	1	31
268.1	0.9737	...	...	83	...	...	25
289.0	0.9674	R	145	108	12	12	25
272.0	0.944	...	...	25	...	...	16
22.0	0.937	N	N	103	1,7	1	25
175.1	0.920	90	...	72	7	...	25
217.0	0.8975	53	52	104	12,7	12	25
237.0	0.877	R	...	88	7	...	24
435.1	0.865	N	N	56	6	6	6
325.0	0.860	30	N	121	...	...	32
6.1	0.840	52	N	26	1	1	22
54.0	0.827	20	11	25	1	1	33
263.1	0.824	41	25	49	1,20	1	31
226.0	0.8177	R	171:,34:	144	1,12	1,12	32
114.0	0.814	R	...	45	16	...	16
265.0	0.811	154	152,83	106	1,12	1,12	29
352.0	0.8057	143	141	164	1,12	1,12	25
41.0	0.794	R	N	146	1	1	33
107.0	0.785	N	...	...	15	...	21
340.0	0.775	43	65	88	1	1	32
277.2	0.766	50	44	61	1	1	25
318.0	0.752	90	N	41	1	1	23,24
343.1	0.750	59	95	97	1	1	24,30
247.0	0.7489	...	47	69	1,7	1	32
55.0	0.7348	167	...	94	1	...	31
292.0	0.713	...	...	162	...	...	...
293.1	0.709	...	...	45	...	...	21
441.0	0.707	144	144	149	1	1	21
34.0	0.689	59:	90,114	85	1	1	32

TABLE 3—*Continued*

3CR	z	PA r	PA [OII]	PA radio	References r	[OII]	radio
220.3	0.685	...	...	117	...	...	32
323.0	0.679	38	...	9	15	...	16
44.0	0.660	45	11	11	1	1	21
263.0	0.656	...	...	113	...	...	25,29
337.0	0.635	R	145	102	1,27	1,27	27
169.1	0.633	165	123	137	1	1	21
49.0	0.621	...	...	87	...	...	23,24
220.1	0.620	...	...	79	...	...	34
225.2	0.582	...	...	...	...	...	24
427.1	0.572	...	...	140	...	...	29,22
228.0	0.5524	R	N	9	1	1	34
330.0	0.550	20	46	62	1	1	37
172.0	0.519	37	24	37	1	1	...
19.0	0.482	...	...	...	...	...	32
275.0	0.480	127	28	51	2,20	2	2
435.0	0.471	28	46	31	1	1	6
411.0	0.467	N	N	108	1	1	35,22
327.1	0.4628	...	...	115	2	2	2
295.0	0.461	113:	135	143	2,20	2	2
313.0	0.461	R	70	59	1,2	1,2	2
200.0	0.458	...	...	159	...	...	34
341.0	0.448	R	180	50	1	1	39
306.1	0.441	177	61	180	1	1	21
46.0	0.437	...	...	68	...	...	39
244.1	0.428	122	133	168	1	1	36
99.0	0.426	...	...	52	...	...	38
274.1	0.422	...	...	76	...	...	36
277.0	0.414	...	...	75	16	...	16
119.0	0.408	...	...	...	...	...	...
142.1	0.406	...	...	...	...	...	21
16.0	0.405	...	...	35	...	...	23
42.0	0.395	...	...	...	...	...	32
268.3	0.371	R	149	161	1	1	23,24
299.0	0.367	56	70,35	64	1	1	3
268.2	0.362	172	...	21	20	...	16
187.0	0.350	...	...	...	20	...	...
320.0	0.342	132	...	77	1	...	39
103.0	0.3306	...	...	159	...	...	...
434.0	0.322	...	...	78	...	...	22
67.0	0.310	90:	...	174	1	...	24,23
109.0	0.3056	...	39	143	2	2	2
165.0	0.2957	...	...	159	...	...	36
173.1	0.292	R	...	...	...	...	23
458.0	0.290	R	39	75	1	1	21,47
438.0	0.290	...	...	46	...	...	31
52.0	0.285	...	...	20	...	...	40
133.0	0.2779	...	...	...	...	...	...
153.0	0.2769	R	45	50	1,20	1	47
300.0	0.270	115	126,90	130	1	1	47
460.0	0.268	31	18	36	1	1	21
303.1	0.267	...	146	90	1	1	...
379.1	0.256	R	180	161	1	1	53
79.0	0.2559	R	146	105	1	1	44
410.0	0.2485	...	...	129	...	...	40
288.0	0.246	...	...	146	...	...	45
166.0	0.245	114	...	180	20	...	...
93.1	0.244	133	N:	...	1	1	...
284.0	0.239	R	116	101	1	1	...
171.0	0.238	169	105	100	2,20	2	2
456.0	0.233	...	...	...	...	...	...
180.0	0.2200	42	26	...	1	1	...
459.0	0.2199	...	...	94	...	...	...

TABLE 3—*Continued*

3CR	z	PA r	PA [OII]	PA radio	References r	[OII]	radio
17.0	0.219	...	...	...	...	...	...
123.0	0.218	92	...	115	20	...	43
287.1	0.2159	...	...	91	...	...	...
436.0	0.2145	...	...	...	...	...	...
132.0	0.214	105	...	...	20	...	...
349.0	0.205	76	...	142	...	...	49
401.0	0.201	...	...	24	...	...	52
196.1	0.198	56	55	43	2,20	2	2
28.0	0.195	142	228	146	1	1	43
234.0	0.1848	R	...	64	20	...	36
33.1	0.181	18	53	45	1	1	47
63.0	0.175	100	74	34	2	2	2
219.0	0.174	127	N	40	2 ,20	2	2
357.0	0.166	90	90	111	1	1	42
258.0	0.165	33	...	...	20	...	16
346.0	0.161	141	125	71	2 ,20	2	2
381.0	0.1605	69	9,135	4	1	1	47
303.0	0.141	N	...	102	20	...	22,31
89.0	0.1386	38	...	115	2	2	2
223.0	0.1368	52	140	164	2 ,20	2	2
197.1	0.130	R	...	...	20	...	...
135.0	0.108	136	57	...	1	1	...
184.1	0.118	...	...	157	...	...	43
223.1	0.1075	49	...	15	...	...	43
327.0	0.1039	136	22	100	2	2	2
433.0	0.1016	153	132	166	1,2	1,2	2
236.0	0.0989	41	...	122	20	...	41
321.0	0.096	124	122	136	1,2	1,2	2
105.0	0.089	...	...	129	2	2	2
227.0	0.086	7	35,119	86	2	2	2
277.3	0.0857	...	147	166	148	148	148
285.0	0.079	126	81	81	2	2	2
15.0	0.073	R	...	...	...	...	...
-35.0	0.067	...	...	13	...	...	50
192.0	0.0598	59	161	124	2	2	2
33.0	0.0595	153	65	19	2	2	2
403.0	0.059	42	23	87	2	2	2
382.0	0.0578	85	88	50	1,20	1	13
445.0	0.056	...	37	176	21	21	21
390.3	0.056	R	...	144	2	2	2
218.0	0.055	135	109	6	2	2	2
29.0	0.0447	97	...	160	2	2	2
305.0	0.041	133:	57	45	2	2	2
317.0	0.035	38	157	185	2	2	2
98.0	0.0306	R	147,95	26	2	2	2
353.0	0.030	...	164	0.00	2	2	2
88.0	0.030	153	118	56	2	2	2

REFERENCES TO TABLES 2 AND 3.—(1) This paper; (2) Baum et al. 1988; (3) van Breugel et al. 1995; (4) McCarthy et al. 1987a; (5) McCarthy et al. 1990; (6) McCarthy et al. 1989; (7) S. Djorgovski et al. 1987, unpublished; (8) M. Dickinson et al. 1990, unpublished; (9) Hammer & Le Fèvre 1990; (10) Le Fèvre & Hammer 1988; (11) Le Fèvre et al. 1988a; (12) Rigler et al. 1992; (13) Hammer et al. 1991; (14) Le Fèvre & Hammer 1990; (15) Djorgovski et al. 1988; (16) Strom et al. 1990; (17) Djorgovski et al. 1987; (18) Le Fèvre et al. 1988b; (19) Le Fèvre et al. 1987; (20) Hutchings et al. 1988; (21) van Breugel & McCarthy 1995; (22) Pooley & Henbest 1974; (23) Pearson et al. 1985; (24) Fanti et al. 1990; (25) Schilizzi et al. 1982; (26) Pedelty et al. 1989a; (27) Pedelty et al. 1989b; (28) Chambers et al. 1988; (29) Leahy et al. 1989; (30) Spencer et al. 1989; (31) Laing 1981; (32) Jenkins et al. 1977; (33) Longair 1975; (34) Burns et al. 1984; (35) Spangler & Pogge 1984; (36) Leahy & Williams 1984; (37) McCarthy et al. 1987b; (38) Mantovani et al. 1990; (39) Gregorini et al. 1988; (40) Pooley et al. 1987; (41) Strom & Willis 1980; (42) Hogbom & Carlsson 1974; (43) Riley & Pooley 1975; (44) Spangler et al. 1984; (45) Bridle et al. 1989; (46) McCarthy et al. 1987b; (47) S. Stocke 1994, private communication; (48) van Breugel et al. 1985; (49) Macdonald et al. 1968; (50) Mackay 1969; (52) Branson et al. 1972; (53) Hargrave & McEllin 1975; (54) Riley and Branson 1973.

TABLE 4

EMISSION-LINE FLUXES

3CR	z	f(erg s^{-1} cm^{-2})	Line	Calibration
454.1	1.8470	9.25×10^{-16}	Lyα	D/S
326.1	1.8250	7.50×10^{-15}	Lyα	D
256.0	1.8190	1.00×10^{-14}	Lyα	D/S
294.0	1.7790	1.00×10^{-14}	Lyα	D/S
437.0	1.4800	7.60×10^{-16}	[OII]	D/S
305.1	1.1320	4.78×10^{-15}	[OII]	D
252.0	1.1035	3.08×10^{-15}	[OII]	D
124.0	1.0830	4.76×10^{-15}	[OII]	D
356.0	1.0790	6.19×10^{-15}	[OII]	D/S
280.0	0.9975	9.33×10^{-15}	[OII]	D/S
184.0	0.9940	1.50×10^{-15}	[OII]	D/S
22.0	0.9370	3.20×10^{-15}	[OII]	D
435.1	0.865	2.70×10^{-16}	[OII]	D/S
6.1	0.8400	4.20×10^{-16}	[OII]	D/S
54.0	0.8274	1.57×10^{-15}	[OII]	D
263.1	0.8240	2.87×10^{-15}	[OII]	D
265.0	0.8110	2.27×10^{-14}	[OII]	D/S
352.0	0.8057	3.67×10^{-15}	[OII]	D/S
340.0	0.7754	1.68×10^{-15}	[OII]	D
277.2	0.7660	6.05×10^{-15}	[OII]	D/S
343.1	0.7500	1.08×10^{-15}	[OII]	D
247.0	0.7489	4.00×10^{-15}	[OII]	D/S
441.0	0.7070	1.20×10^{-15}	[OII]	D/S
34.0	0.6890	1.93×10^{-14}	[OII]	D/S
44.0	0.6600	1.73×10^{-15}	[OII]	D/S
337.0	0.6350	2.54×10^{-16}	[OII]	D/S
169.1	0.6330	3.95×10^{-15}	[OII]	D
228.0	0.5524	1.17×10^{-15}	[OII]	D
330.0	0.5500	1.29×10^{-14}	[OII]	D/S
172.0	0.5191	5.50×10^{-15}	[OII]	D/S
435.1	0.4710	1.00×10^{-14}	[OII]	D/S
313.0	0.4610	3.76×10^{-15}	[OIII]	D
341.0	0.4480	8.00×10^{-16}	[OII]	D
306.1	0.4410	3.50×10^{-15}	[OII]	D/S
244.1	0.4280	1.60×10^{-14}	[OIII]	D
268.3	0.3710	6.60×10^{-15}	[OIII]	D
299.0	0.3670	1.01×10^{-14}	[OII]	D/S
458.0	0.2900	5.46×10^{-15}	[OII]	D
153.0	0.2769	1.27×10^{-14}	HA + NII	D
300.0	0.2700	1.32×10^{-14}	[OII]	D/S
460.0	0.2680	3.03×10^{-15}	[OIII]	D/S
303.1	0.2670	2.95×10^{-14}	[OIII]	D
79.0	0.2559	1.93×10^{-14}	[OIII]	D/S
284.0	0.2394	1.42×10^{-15}	HA + NII	D/S
180.0	0.2200	2.75×10^{-15}	[OII]	D/S
28.0	0.1952	5.97×10^{-15}	HA+NII	D
33.1	0.1810	1.37×10^{-14}	HA NII	D
381.0	0.1605	4.47×10^{-14}	[OIII]	D
433.0	0.1016	2.68×10^{-15}	[OIII]	D/S
382.0	0.0578	2.30×10^{-15}	HA	D

as from consideration of the emission-line luminosity versus redshift diagram. These ratios do not necessarily reflect the actual values of line ratios in individual objects. While the [O III] λ5007/[O II] λ3727 ratio of 3.0 does accurately reflect the observed ratio in the typical 3CR galaxy, the Lyα/Hα ratio had to be derived indirectly and does not necessarily reflect the ratio in any one galaxy. The recent near-IR spectroscopic measurements of Hα at redshifts of 1–2.5 by McCarthy, Elston, & Eisenhandt (1992) and Eales & Rawlings (1993) lend support to the validity of the adopted ratio. The line ratios will be discussed in detail in Paper II.

The largest angular size of each nebula is given in Table 2 along with the corresponding linear size for two cosmologies: $H_0 = 50$, $q_0 = 0$ and $H_0 = 50$, $q_0 = 0.5$. We also list the largest angular sizes of the radio sources, as given in McCarthy et al. (1991) in Table 2.

We have measured the position angle on the sky of the longest dimension of the extended emission-line regions. The objects have sufficiently complex morphologies that, in many cases, the position angle is not terribly well defined. The overall uncertainty in the position angle measurements is ~10°–15°. Images of other 3CR and 1 Jy class radio galaxies in the literature have also been measured and are included in Table 3. We have also determined the position angle of the continuum emission in the *R* images. These measurements are based in large part on data in the literature that supersede the continuum images shown here. The high spatial resolution and high signal-to-noise ratio images obtained by Le Fèvre and his collaborators (Le Fèvre et al. 1988a, b; Hammer & Le Fèvre 1990) and Rigler et al. (1992) were used wherever possible. The position angle on the sky of the radio source, as defined by the line between the two brightest hot spots, is listed in column (6) of Table 3. The sources of the images and radio maps used for these measurements are given in the notes to Table 3.

In Table 4 we give the observed flux for a single emission line for each object, along with the source of the data and the type of measurement, direct imaging or long-slit spectroscopy. We have spatially integrated the direct images to determine the total flux. The long-slit measurements are summed along a 3″–6″ length of a 2″–2.″5 wide slit. The spectroscopic observations will underestimate the total flux. In the last column of Table 4 we list the method used to calibrate the imaging data.

6. SUMMARY

We have presented emission-line and continuum images for a sample of 53 radio galaxies from the 3CR catalog. These objects span roughly four orders of magnitude in radio luminosity and roughly 70% of the age of the universe in look-back time. Extended line emission is found in nearly 90% of the objects. At large redshifts the continuum morphology becomes highly elongated and aligned with the radio source axis. These data will be analyzed and compared with the radio source properties in detail in Paper II.

We gratefully acknowledge the support and assistance of the staffs of Lick Observatory and Kitt Peak National Observatory. The interference filters used in this program were obtained with funds provided by the California Space Institute. The research of H. S. and P. M. was supported by the National Science Foundation under grant AST 87-06227. The research of W. v B. was performed at IGPP/LLNL under the auspices of the US Department of Energy under contract W-7405-ENG-48. We thank G. Djorgovski for the use of unpublished images of 3C 124 and 3C 256, as well as for helpful discussions.

REFERENCES

Antonucci, R. R. J., & Miller, J. S. 1985, ApJ, 297, 621
Balick, B., & Heckman, T. 1982, ARA&A, 20, 431
Baum, S. A. 1987, Ph.D. thesis, Univ. Maryland
Baum, S. A., & Heckman, T. 1987, in Radio Continuum Processes in Clusters of Galaxies, ed. C. O'Dea & J. Uson (NRAO), 119
———. 1989a, ApJ, 336, 681
———. 1989b, ApJ, 336, 702
Baum, S. A., Heckman, T., Bridle, A., van Breugel, W., & Miley, G. 1988, ApJ, 68, 643
Baum, S. A., Heckman, T., & van Breugel, W. 1992, ApJ, 389, 208
Bennet, A. S. 1962, MmRAS, 68, 163
Branson, N. J. B. A., Elsmore, B., & Pooley, G. G. 1972, MNRAS, 156, 377
Bridle, A. H., Fomalont, E. B., Byrd, G. G., & Valtonen, M. 1989, AJ, 97, 674
Burns, J. O., Basart, J. P., De Young, D. S., Ghiglia, D. C. 1984, ApJ, 238, 515
Chambers, K., Miley, G., & Joyce, R. 1988, ApJ, 329, L75
Dickinson, M., Djorgovski, S., & Spinrad, H. 1995 in preparation
Djorgovski, S. 1985, PASP, 97, 1119
Djorgovski, S., Spinrad, H., Pedelty, J., Rudnick, L., & Stockton, A. 1987, AJ, 93, 1307
Djorgovski, S., Spinrad, H., & Dickinson, M. 1991, unpublished
Djorgovski, S., Spinrad, H., McCarthy, P. J., van Breugel, W., Dickinson, M., & Strom, R. 1988, AJ, 96, 836
Eales, S. A., & Rawlings, S. 1990, MNRAS, 243, 1P
———. 1993, ApJ, 411, 67
Fanti, R., Fanti, C., Schilizzi, R. T., Spencer, R. E., Rendong, N., Parma, P., van Breugel, W., & Venturi, T. 1990, A&A, 231, 333
Feretti, L., Gioia, I. M., Giovannini, G., Gregorini, L., & Padrielli, L. 1984, A&A, 139, 50
Fernini, I., Burns, J. O., Bridle, A. H., & Perley, R. A. 1993, AJ 105, 1690
Fosbury, R. A. E. 1986, in Structure and Evolution of Active Galactic Nuclei, ed. G. Givrincin, F. Mardirossian, M. Mezzetti, & M. Ramonella (Dordrecht: Reidel), 297
———. 1990, in Proc. ESO Conf. and Workshop 32, Extranuclear Activity in Galaxies, ed. E. J. A. Meurs & R. A. E. Fosbury (Garching: ESO), 169
Gregorini, L., Padrielli, L., Parma, P., & Gilmore, G. 1988, A&A, 202, 329
Hammer, F., & Le Fèvre, O. 1990, ApJ, 357, 38
Hammer, F., Le Fèvre, O., & Proust, D. 1991, ApJ, 374, 91
Hargrave, P. J., & McEllin, M. 1975, MNRAS, 173, 37
Heckman, T., Smith, E., Baum, S., van Breugel, W., Miley, G., Illingworth, G., Bothun, G., & Balick, B. 1986, ApJ, 311, 526
Högbom, J. A., & Carlsson, I. 1974, A&A, 34, 341
Hutchings, J. B., Johnson, I., & Pike, R. 1988, ApJS, 66, 361
Jannuzi, B., & Elston, R. 1991, ApJ, 366, L69
Jenkins, C. J., Pooley, G. G., & Riley, J. M. 1977, MmRAS, 84, 61
Kristian, J. A., Sandage, A. R., & Katem, B. 1974, ApJ, 191, 43
Laing, R. A. 1981, MNRAS, 195, 261
Laing, R. A., Owen, F., & Puschell, J. 1984, unpublished
Laing, R. A., Riley, J., & Longair, M. 1983, MNRAS, 204, 151
Leahy, J. P., Muxlow, T., & Stephens, P. 1989, MNRAS, 239, 40
Leahy, J. P., & Williams, A. G. 1984, MNRAS, 210, 929
Le Fèvre, O., & Hammer, F. 1988, ApJ, 333, L37
———. 1990, ApJ, 350, L1
Le Fèvre, O., Hammer, F., & Jones, J. 1988a, ApJ, 331, L73
Le Fèvre, O., Hammer, F., Nottale, L., & Mathez, G. 1987, Nature, 326, 268
Le Fèvre, O., Hammer, F., Nottale, L., Mazure, A., & Christian, C. 1988b, ApJ, 324, L1
Lilly, S. J., Longair, M., & McLean, I. 1983, Nature, 301, 488
Longair, M. 1975, MNRAS, 173, 309
Macdonald, G. H., Kenderdine, S., & Neville, A. C. 1968, MNRAS, 138, 259
Mackay, C. D. 1969, MNRAS, 145, 31
Mantovani, F., Saikia, D. J., Browne, I. A. W., Fanti, R., Muxlow, T., & Padrielli, L. 1990, MNRAS, 245, 427
McCarthy, P. 1993, ARA&A, 31, 639
McCarthy, P., & Baum, S. 1995, ApJ, submitted
McCarthy, P., Elston, R., & Eisenhardt, P. 1992, ApJ, 387, L29
McCarthy, P. J., Spinrad, H., Djorgovski, S., Strauss, M. A., van Breugel, W. J. M., & Liebert, J. 1987a, ApJ, 319, L39
McCarthy, P., Spinrad, H., van Breugel, W., Liebert, J., Dickinson, M., Djorgovski, S., & Eisenhardt, P. 1990, ApJ, 365, 487
McCarthy, P., van Breugel, W., & Kapahi, V. 1991, ApJ, 371, 478
McCarthy, P., van Breugel, W., & Spinrad, H. 1989, AJ, 97, 36
McCarthy, P. J., van Breugel, W. J. M., Spinrad, H., & Djorgovski, S. 1987b, ApJ, 321, L29
Miller, J. S., & Stone, R. P. S. 1987, Lick Obs. Tech. Bull., 48, 1
Oke, J. B. 1974, ApJS, 27, 21
Osterbrock, D. E., Koski, A. T., & Phillips, M. M. 1986, ApJ, 206, 898
Pearson, T. J., Perley, R. A., & Readhead, A. C. S. 1985, AJ, 90, 738
Pedelty, J. A., Rudnick, L., McCarthy, P. J., & Spinrad, H. 1989a, AJ, 97, 647
——— 1989b, AJ, 200, 1067
Perryman, M. A. C., Lilly, S. J., Longair, M. S., Downes, A. J. B. 1984, MNRAS, 209, 159
Pooley, G. G., & Henbest, S. N. 1974, MNRAS, 169, 477
Pooley, G. G., Leahy, J. P., Shakeshaft, J. R., & Riley, J. M. 1987, MNRAS, 224, 847
Rigler, M., Lilly, S., Stockton, A., Hammer, F., & Le Fèvre, O. 1992, ApJ, 385, 61
Riley, J. M., & Branson, N. J. B. A. 1973, 164, 271
Riley, J. M., Longair, M. S., & Gunn, J. E. 1980, MNRAS, 192, 233
Riley, J. M., & Pooley, G. G. 1975, MNRAS, 80, 105
Robinson, A., Binnett, L., Fosbury, R. A. E., & Tadhunter, C. N. 1987, MNRAS, 227, 97
Schilizzi, R., Kapahi, V. K., & Neff, S. 1982, J. Astron. Astrophys., 3, 173
Smith, E. P., & Heckman, T. 1989a, ApJS, 69, 365
———. 1989b, ApJ, 341, 658
Smith, H. E., & Spinrad, H. 1980, PASP, 92, 553
Spangler, S. R., & Pogge, J. J. 1984, AJ, 89, 342
Spangler, S., Myers, S. T., & Pogge, J. J. 1984, AJ, 89, 1478
Spencer, R. E., McDowell, J. C., Charleworth, M., Fanti, C., Parma, P., & Peacock, J. A. 1989, MNRAS, 240, 657
Spinrad, H. 1986, PASP, 98, 269
Spinrad, H., & Djorgovski, S. 1984a, ApJ, 280, L9
———. 1984b, ApJ, 285, L49
Spinrad, H., Djorgovski, S., Marr, J., & Aguilar L. A. 1985a, PASP, 97, 932
Spinrad, H., Filippenko, A., Wyckoff, A., Stocke, J., Wagner, M., & Lawrie, D. 1985b, ApJ, 299, L7
Spinrad, H., et al. 1995, in preparation
Stone, R. P. S. 1977, ApJ, 218, 767
Strom, R., Riley, J. M., Spinrad, H., van Breugel, W. J. M., Djorgovski, S., & McCarthy, P. J. 1990, A&A, 227, 19
Strom, R. G., & Willis, A. G. 1980, A&A, 85, 36
Tadhunter, C. N., Perez, E., & Fosbury, R. A. E. 1986, MNRAS, 219, 555
van Breugel, W. J. M. 1986, in Proc. Toronto Conf., Jets from Stars and Galaxies, ed. R. N. Henriksen & T. W. Jones (Canadian J. Phys., Vol. 64), 392
———. 1990, in Lecture Notes in Physics 327, Hot Spots in Extragalactic Radio Sources, ed. K. Meisenheimer & H.-J. Roser (Heidelberg: Springer), 25
van Breugel, W., & McCarthy, P. 1989, in ESO Conf. and Workshop Proc. 32, Extranuclear Activity in Galaxies, ed. E. J. A. Meurs & R. A. E. Fosbury (Garching: ESO), 227
———. 1995, in preparation
van Breugel, W., McCarthy, P., & Spinrad, H. 1995, in preparation
van Breugel, W., Miley, G. K., Heckman, T. M., Butcher, H. R., & Bridle, A. H. 1985, ApJ, 290, 496
Wyndham, J. D. 1966, ApJ, 144, 459